

Extremely Low Frequency (ELF) Radio Wave Propagation: A review

A.P. Nikolayenko¹, A. Shvets¹, and M. Hayakawa²

¹*Usikov Institute for Radio-Physics and Electronics, National Academy of Sciences of the Ukraine, Kharkov, Proskura st. 12, 61085, Ukraine*

²*The University of Electro-Communications, Advanced Wireless & Communications research Center, 1-5-1 Chofugaoka, Chofu Tokyo 182-8585, Japan*

Abstract.

The Extremely Low Frequencies (ELF) extend from 3 Hz to 3 kHz. This formal limit corresponds to real physical phenomena in subionospheric radio propagation: the Schumann Resonance (SR) observed in the band between 4 Hz and 40 Hz and the transverse resonance having the basic frequency about 1.7 kHz. When speaking about ELF radio waves, we usually have in mind the subionospheric propagation when electromagnetic wave travels in the spherical dielectric stratum formed by the Earth's surface and the lower edge of the ionospheric plasma. The dielectric shell has a small thickness of about 60–100 km in comparison with the Earth's radius of ~6366 km. This non-conducting layer forms a spherical cavity resonator, with two sets of eigen-values. One of them corresponds to the global electromagnetic resonance predicted by Schumann [1952], which is often regarded as SR. Its peak frequencies (frequencies of maxima in the power spectra of natural ELF radio noise) are approximately 8, 14, 20, Hz, etc. At such low frequencies, only transverse electromagnetic (TEM) wave propagates in the cavity having the non-zero vertical electric E_r and horizontal magnetic H_ϕ field components. If we account for the finite ground conductivity, a small longitudinal electric field E_θ appears. It is clear that we use the spherical polar coordinate system (r, θ, ϕ) with the origin at the Earth's center and the polar $\theta = 0$ axis directed to the vertical electric dipole source.

Owing to small losses and a great wavelength, the resonance signals can multiply & circle the globe, so that direct and antipodal waves interfere forming a set of maxima in the power spectrum of vertical electric or horizontal magnetic fields positioned at the above-mentioned frequencies. Lightning strokes of the global thunderstorms occurring at the rate of 50–100 discharges per second serve as the source of natural ELF radio noise. SR might be regarded as “longitudinal” one: it occurs in the waves propagating along the Earth's surface.

The second type of resonance corresponds to vertically propagating radio waves, therefore, it is called the transverse resonance. Relevant waves are captured between the ground and ionosphere, so that their basic frequency depends on the ionosphere height and is equal to 1.7

kHz when the thickness of the ground–ionosphere gap is 88 km. Transverse resonance is a local phenomenon, because it is not linked with the round-the-world propagation. In radio engineering, the eigen-values of transverse resonance are regarded as cutoff frequencies of the modes propagating in the Earth–ionosphere duct. The basic frequency is the cut-off frequency of the first-order mode, the second-order mode has the cutoff equal to the doubled basic frequency of transverse resonance, etc. Obviously, only the basic transverse resonance frequency definitely belongs to the ELF band, while the higher-order modes are found within the very low frequency (VLF) band.

Key words: 1 ; ELF(extremely low frequency),2; ELF propagation theory, 3; atmospheric conductivity, 4;VLF(very low frequency), 5;Schumann resonance (SR), 6;ELF transients, 7; Q-bursts, 8;global thunderstorm activity, 9;global warming, 10; terminator effect, 11;space weather, 12; inverse problem, 13;transverse resonance,14; tweeks.

1. Introduction

We describe the Extremely Low Frequency (ELF) radio propagation in the Earth-ionosphere cavity. The formal description of electromagnetic field is presented in the frequency and in the time domains. The expected spectra are demonstrated of the global electromagnetic (Schumann) resonance. The waveforms are given of the ELF transients or Q-bursts. Models of ELF propagation constant are listed together with the efficient approximate models of the lower ionospheric conductivity. The vertical profiles of conductivity are given that provide realistic Schumann Resonance (SR) data in the direct field computations, such as FDTD (Finite Difference Time Domain) method. Observational aspects are addressed including a brief description of the field sources, instrumentation, and typical signal processing with illustrations of actual data. Information is presented deduced from the ELF observations, e.g., diurnal/seasonal variations of global thunderstorm activity. Impact of ionospheric non-uniformities is mentioned in the context of its separation from alterations in the global thunderstorm activity. A comparison is made of the model time domain pulse with the unique observations of distant Q-bursts. Transverse resonance in the Earth–Ionosphere cavity is introduced as observed as tweek atmospherics. A solution of relevant inverse problem is briefly described allowing simultaneous inference of the source distance and parameters of the lower ionosphere (“Kharkov technique”). The other topics are listed that could not be included in the article of limited size.

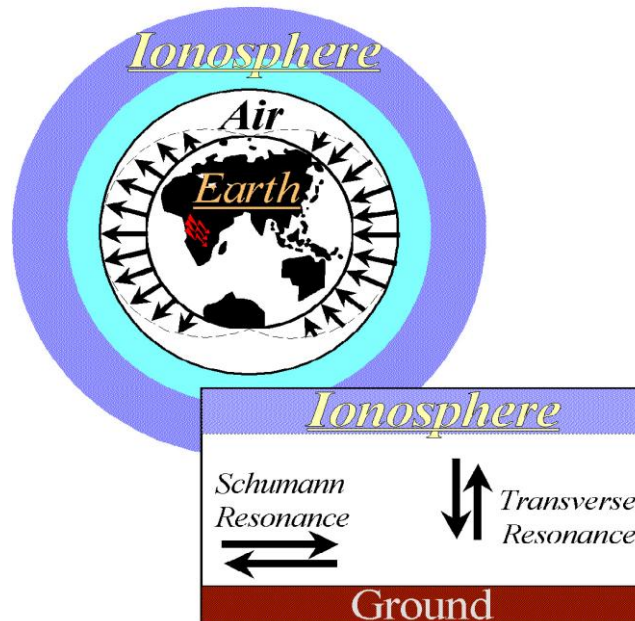


Figure 1: Two types of electromagnetic resonance (longitudinal (Schumann) and transverse) in the Earth – ionosphere cavity

The ELF extends from 3 Hz to 3 kHz. This formal limit corresponds to real physical phenomena in subionospheric radio propagation: the SR observed in the band between 4 and 40 Hz and the transverse resonance with the basic frequency about 1.7 kHz (see Figure. 1). When speaking about ELF radio waves, we usually have in mind the subionospheric propagation when electromagnetic wave travels in the spherical dielectric strata formed by the Earth’s surface and the lower edge of the ionospheric plasma. The dielectric shell has a small thickness of about 60–100 km in comparison with the Earth’s radius of ~6366 km. This non-conducting layer forms a spherical cavity resonator, having two sets of eigen-values. One of them is the global electromagnetic resonance predicted by Schumann [1952] which is often regarded as SR. Its peak frequencies are approximately 8, 14, 20, Hz, etc. At such low frequencies, only transverse electromagnetic (TEM) wave can propagate in the cavity having the non-zero vertical electric E_r and horizontal magnetic H_φ field components. If we account for the finite ground conductivity, there appears a small longitudinal electric field E_θ . It is clear that we use the spherical polar coordinate system (r, θ, φ) with the origin at the Earth’s center and the polar $\theta = 0$ axis directed to the vertical electric dipole source.

Because of small losses and great wavelength, resonance signals can multiply & circle the globe, so that direct and antipodal waves interfere forming a set of maxima in the power spectrum of vertical electric or horizontal magnetic fields positioned at the above-mentioned frequencies. Lightning strokes of the global thunderstorm activity occurring at the rate of 50–100 discharges in a second serve as the source of natural ELF radio noise. SR might be regarded as “longitudinal”: it occurs due to waves propagating along the ground.

The second type of resonance corresponds to radio waves propagating vertically, so it is called the transverse resonance. Relevant waves propagating vertically are trapped between the ground and ionosphere, so that their basic frequency depends on the ionospheric height and is equal to 1.7 kHz when the thickness of the ground – ionosphere gap is 88 km. Transverse resonance is a local phenomenon, because it is not linked with the round-the-world propagation. On the other hand, frequencies of transverse resonance are regarded as the cut-off frequencies of modes propagating in the Earth–ionosphere duct. The basic frequency is the cutoff frequency of the first mode, and the second mode has the cutoff equal to the doubled basic frequency of transverse resonance, etc. Obviously, only the basic transverse resonance definitely belongs to the ELF band and higher-order modes are found within the very low frequency (VLF) band.

2. Radio Propagation at ELF

2.1. Radio propagation theory

In the simplest approach one considers the Earth–Ionosphere cavity formed by two perfectly conducting concentric spheres with the cavity height h much smaller than the Earth radius a . The Schumann’s formula is derived for the eigen-frequencies $f_n = \frac{c}{2\pi a} \sqrt{n(n+1)}$ where $n = 1, 2, \dots$ is the SR mode number [Schumann, 1952]. After substituting the light velocity c and the Earth’s circumference $2\pi a$, one obtains the equation $f_n = 7.5[n(n+1)]^{1/2}$ and the following succession of the eigen-values: 10.6, 18.4, 26.0, 33.5 Hz, etc. Peak frequencies f_{PEAK} of SR are observed in the power spectra of natural ELF radio noise being about 8, 14, 20, 26 Hz, etc. These also vary with the mode number as $[n(n+1)]^{1/2}$, and only the factor 7.5 Hz should be replaced with 5.7 Hz (see Figure 2).

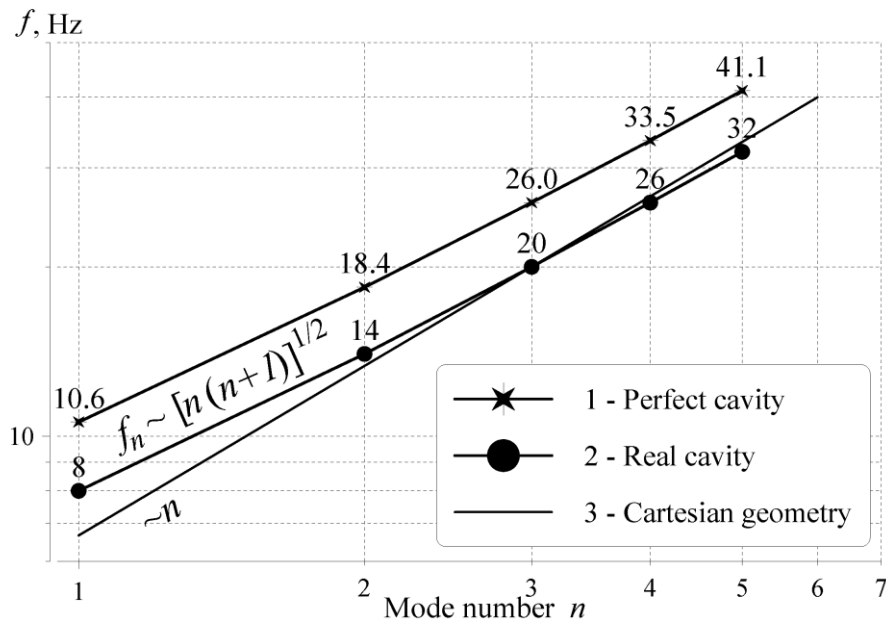


Figure 2: Eigen-values of perfect and observed peak frequencies of the Earth-ionosphere cavity

Deviations of observed peak frequencies from the $[n(n+1)]^{1/2}$ dependence do not exceed 3%, and this proves that the Earth is a sphere. Plots in Figure. 2 show the congruent curves of the perfect and real cavities, and the both deviate from the linear asymptotic dependence relevant to Cartesian geometry (see Chapter 2 in [Nickolaenko and Hayakawa 2002] for details).

Formulas for the electric and magnetic fields of the cavity are obtained from the solution of the boundary problem, and the detailed description might be found in [Nickolaenko and Hayakawa 2002; Wait, 1970; Galejs, 1972; Bliokh, 1980 ; Nickolaenko and Hayakawa 2014]. A single zero-order mode propagates in the cavity at frequencies below 1.6–1.7 kHz, and it is often regarded as TEM mode. Only two field components might be detected on the perfectly conducting ground:

$$E_r(\omega) = \frac{M_C(\omega) i \nu(\nu+1) P_\nu^1[\cos(\pi-\theta)]}{4ha^2 \varepsilon \omega \sin \pi \nu} \quad (1)$$

$$H_\phi(\omega) = -\frac{M_C(\omega) P_\nu^1[\cos(\pi-\theta)]}{4ha \sin \pi \nu} \quad (2)$$

Here E_r and H_ϕ are the vertical electric and horizontal magnetic fields in V/m and A/m correspondingly, ω is the angular frequency, M_C is the current moment of the source (Am), h is the effective height of the cavity in m, a is the Earth's radius in m, ε is the permittivity of free space in F/m, ν is the dimensionless propagation constant, θ is the source-observer angular distance in

radians, and $P_\nu(x)$ and $P_\nu^1(x)$ are the Legendre and associated Legendre functions of order ν and argument x . The vertical electric dipole source of the current moment M_C is positioned at the pole $\theta = 0$ of the spherical polar coordinate system (r, θ, ϕ) with the origin at the Earth's center.

The physical meaning of the parameter $\nu(\omega) = \nu_1(\omega) - i\nu_2(\omega)$ becomes clear at high frequencies where $|\nu| \cong ka \gg 1$ and the asymptotic expansions are valid for the Legendre functions [Gradstein and Ryzhik, 1963]:

$$P_\nu[\cos(\pi - \theta)] = \sqrt{\frac{2}{\pi(\nu + 1/2)\sin\theta}} \cos[(\nu + 1/2)(\pi - \theta) - \pi/4] \quad (3)$$

$$P_\nu^1[\cos(\pi - \theta)] = \sqrt{\frac{2\pi(\nu + 1/2)}{\pi\sin\theta}} \sin[(\nu + 1/2)(\pi - \theta) - \pi/4] \quad (4)$$

Here θ should not be equal to 0 or π . At high frequencies the imaginary part $\nu_2(\omega)$ responsible for the wave attenuation is large, so that the trigonometric functions are replaced by exponential functions:

$$\frac{P_\nu[\cos(\pi - \theta)]}{\sin\pi\nu} = i \sqrt{\frac{2}{\pi(\nu + 1/2)\sin\theta}} \exp\{-i[(\nu_1 + 1/2)\theta - \pi/4] - \nu_2\theta\} \quad (5)$$

$$\frac{P_\nu^1[\cos(\pi - \theta)]}{\sin\pi\nu} = i \sqrt{\frac{2(\nu + 1/2)}{\pi\sin\theta}} \exp\{-i[(\nu_1 + 1/2)\theta - \pi/4] - \nu_2\theta\} \quad (6)$$

The above formulas suggest that the time dependence is of the form $\exp(+i\omega t)$, and so the field components in Eqs. (5) and (6) are proportional to $\exp[(i\omega t - \nu_1\theta)]$. Hence Eqs. (5) and (6) contain the direct wave traveling from the source to the observer along the great circle path, and $\nu(\omega)$ is the propagation constant when the path is measured in radians. Formulas (3) and (4) include both the direct and antipodal waves. The antipodal wave travels along the same great circle, but reaches the observer via the source antipode and has smaller amplitude. At SR frequencies we have $|\nu| \cong 1$, so we cannot use the asymptotic expansions (3–6) corresponding to $|\nu| \gg 1$. The zonal harmonic expansion is used here for the Legendre functions.

SR occurs physically when the wavelength is comparable with the Earth's circumference, direct and antipodal waves arrive at the observer having almost the same amplitudes, and the observed field strongly depends on the wave interference. The amplitude increases at the frequencies where the waves meet in phase, and we speak about the SR maxima. At frequencies below 100 Hz, the zonal harmonic series representation (ZHSR) is used [Jones, 1969; Jones, 1970]:

$$E_r(\omega) = -\frac{M_C(\omega)}{4\pi\epsilon_0 a^2} \frac{i\nu(\nu+1)}{\omega} \sum_{n=0}^{\infty} \frac{(2n+1)P_n(\cos\theta)}{n(n+1) - \nu(\nu+1)} \quad (7)$$

$$H_{\varphi}(\omega) = \frac{M_C(\omega)}{4\pi ha} \sum_{n=1}^{\infty} \frac{(2n+1)}{n(n+1) - \nu(\nu+1)} P_n^1(\cos \theta) \quad (8)$$

We conclude that the following parameters are necessary in the computations of expected ELF fields: the source current moment (M_C), the effective height of the Earth–Ionosphere waveguide (h), the source–observer distance (SOD) (θ), and the propagation constant (ν). The source current moment $M_C(f)$ is supposed to be a constant equal to 10^8 A m Hz^{1/2}, which corresponds to a realistic lightning stroke with the channel length of 4 km and the current spectral density of 25 kA Hz^{1/2}. Such a current moment corresponds to a delta-function in the time domain, and the relevant charge moment is a step function. The effective height of the cavity and the propagation constant will be discussed below.

Each term in the ZHSR (7) and (8) is called the mode, and it contains the resonance denominator that might be written in the form: $n(n+1) - \nu(\nu+1) = (n - \nu)(n + \nu + 1)$. The ELF propagation constant $\nu(f)$ is a complex function of frequency, and the following condition is satisfied at SR: $\text{Re} [\nu(f_{PEAK})] \approx n$, so that the resonance denominator becomes small and the n -th term in Eqs. (7) and (8) is large. Thus the resonance peaks appear in ELF spectra. Each resonance term of ZHSR is multiplied by the relevant Legendre or associated Legendre polynomials, and the products sum provides the unique outline of SR amplitude spectra for a given SOD θ as seen in Figure 3.

The series in Eqs. (7) and (8) converge poorly, because this is conditioned by the field singularity at the source point. The method of acceleration convergence of the series is adopted, and we show the final result (see [Nickolaenko and Hayakawa 2002; Nickolaenko and Hayakawa 2014] for details and references).

$$-\pi \frac{P_{\nu}(-x)}{\sin \pi \nu} = R_{\Sigma} + \sum_{n=0}^{\infty} \frac{a^u}{a^b} P_n(x) \quad (9)$$

where $R_{\Sigma} = 2R_1 + R_2 + 2[\nu(\nu+1)+1]R_3 + 3[3\nu(\nu+1)+2]R_4$, $R_1 = \ln \frac{\sqrt{1-x} + \sqrt{2}}{\sqrt{1-x}}$, $R_2 = 1 + (1-x)R_1 - \sqrt{2(1-x)}$,

$$R_4 = -R_1(5x+1)(x-1)^2/12 + (15x^2 - 27x + 14)/36 + 5(1-x^2)\sqrt{2(1-x)}/12 - 11\sqrt{2(1-x)^3}/18,$$

$$R_3 = 1 + 3R_1(1-x)(3x-1)/4 - \left(x + \sqrt{2(1-x)^3}\right)3/4, \quad a^u = 2n[\nu^2(\nu+1)^2 + 22\nu(\nu+1) + 12] + 17\nu^2(\nu+1)^2 + 74\nu(\nu+1) + 24,$$

$$a^b = (n-\nu)(n+\nu+1)(n+1)(n+2)(n+3)(n+4).$$

Similar expressions are valid for accelerated computations of associated Legendre function:

$$-\pi \frac{P_v^1(-x)}{\sin \pi v} = \frac{2v(v+1)}{\sqrt{1-x^2}} \left(2R_3 + 9R_4 + \sum_{n=0}^{\infty} \frac{b^n}{b^b} P_n(x) \right) \quad (10)$$

where $b^b = [v(v+1) - (n-1)n][v(v+1) - (n+1)(n+2)](n+1)(n+2)(n+3)(n+4)$ and

$$b^n = 4n^3[v(v+1)+12] + 2n^2[19v(v+1)+78] - n[2v^2(v+1)^2 + 19v(v+1)+66] - [17v^2(v+1)^2 - 34v(v+1) - 24].$$

2.11 SR over the frequency – distance plane

Field expansions with accelerated convergence allow us to compute the SR spectra for any SOD. We plot the 2D (2 dimensional) amplitude distributions in Figure 3 of electric and magnetic fields over the frequency–distance plane. Frequency is shown along the abscissa on logarithmic scale, and SOD is shown on the ordinate in mega meters (1 Mm= 1,000 km). Field amplitude is shown with color. The left graph corresponds to the vertical electric field and the right one depicts the amplitude of the horizontal magnetic field component.

We had used the heuristic linear dependence of propagation constant (see below). The source current moment was equal to 10^8 A m s, and the fields were measured in $\text{mV m Hz}^{1/2}$ and $\mu\text{A m Hz}^{1/2}$ correspondingly. The maps illustrate the interaction of direct and antipodal waves that forms the resonance patterns in the space and frequency. A broad spectral maximum occupies the frequencies of some hundred Hertz when the SOD is small. This is the area where the slow-tail ELF atmospherics might be observed. With an increase in SOD, the wave attenuation also increases and the spectral peaks rapidly decrease [Nickolaenko and Hayakawa 2002; Nickolaenko and Hayakawa 2014].

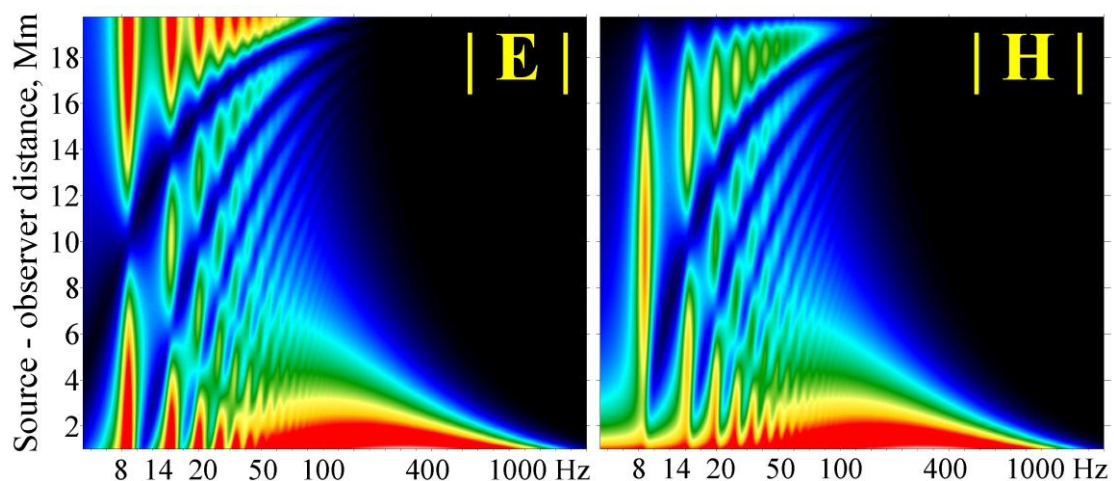


Figure 3: Amplitudes of E and H fields over the frequency–distance plane, where 1 Mm=1,000km

Figure 3 includes a system of summits (shown by red color) corresponding to individual SR modes. Amplitude of the vertical electric field grows toward the source and to its antipode where the well-resolved SR peaks are visible. These two ‘highlands’ are divided by a wide ‘valley’ centered around the distance of 10 Mm. One observes a series of peaks extended vertically in the maps, i.e., along the SR modal frequencies. A few summits and saddles are positioned here corresponding to maxima and to the nodes of a given resonant mode, which are described by the corresponding Legendre polynomial. The central valley gradually descends toward the higher frequencies owing to an increase in the wave attenuation.

The side canyons are also present in Figure 3 extended from lower left to upper right. These appear due to the interaction of direct and antipodal waves and tend to connect the nodes of adjacent modes. These areas correspond to the condition: $\nu(f) (\pi - \theta) \approx const$ describing the families of hyperbolic curves. There exists a secondary hardly visible symmetric system of canyons approaching the source.

The right map in Figure 3 refers to the horizontal magnetic field. Interaction of direct and antipodal waves is also present here. Both the fields contain a broad slow-tail peak when the SOD is small. A succession of equidistant saddles and peaks is seen at a fixed distance in both maps. The ‘antipodal effect’ becomes visible at high frequencies: a series of depressions here tend to become extended horizontally.

There are distinctions between the ‘electric’ and ‘magnetic’ field distributions. The absence of magnetic field at the source antipode is the most evident feature. Besides, a peak in the electric map always corresponds to a relevant node in the magnetic map. This feature follows from the conservation law of the total electromagnetic power which is equally distributed in the cavity, so that a maximum of one field occurs at the minimum of the other field component.

2.12 ELF fields in the time domain

The time domain solution is constructed as the formal Fourier transform of the frequency domain series (7) and (8). Spectral components of the fields have the poles in the complex frequency plane, and so one can use the residual theorem for obtaining the ZHSR in the time domain for both the fields (e.g., [Nickolaenko and Hayakawa 2002; Wait, 1970; Nickolaenko and Hayakawa 2014]). Convergence of the ZHSR in the time domain is better than that in the frequency domain, and still it might be accelerated by extracting the singularity. The results are of the following form:

$$E(t) = E_A \cdot \text{Re} \left\{ A_\nu \cdot \tau^{-B_\nu} \left[Q_{-1} + (Q_0 - 1)B_\nu + \left(\frac{Q_1}{\tau} - 1 \right) B_\nu (B_\nu + 1) + B_\nu (B_\nu + 1)^2 \sum_{n=1}^{\infty} \frac{P_n(x)}{(n - B_\nu)(n + 1)} \exp \left(\frac{itn}{A_\nu} \right) \right] \right\} \quad (11)$$

$$H(t) = H_A \cdot \text{Im} \left\{ \left(1 - x^2 \right)^{1/2} \left(1 - 2x\tau + \tau^2 \right)^{3/2} \exp \left[\frac{it(1 - B_\nu)}{A_\nu} \right] \right\} \quad (12)$$

Here $E_A = M_C / (2\pi\epsilon h a^2)$ and $H_A = M_C / (2\pi h a)$ are the electric and magnetic field amplitudes; $x = \cos\theta$; $\tau = \exp(it/A_\nu)$ is the time factor; functions $Q_{-1} = (1 - x\tau)(1 - 2x\tau + \tau^2)^{-3/2} - 1$ and $Q_1 = \ln\{[\tau - x + (1 - 2x\tau + \tau^2)^{-1/2}]/(1 - x)\}$ were derived from the generating function of Legendre polynomials $Q_0 = (1 - 2x\tau + \tau^2)^{-1/2}$. Analytical time domain solutions (16) and (17) imply the linear frequency dependence $\nu(\omega) = A_\nu \omega + B_\nu$, so that the poles are positioned along the straight lines in the complex frequency plane.

Each term in the series (11) contains a parameter τ , which decreases exponentially with time or mode number n . This factor becomes equal to unity when $t = 0$, so that the series (16) diverges at the point $\theta = 0$ where $P_n(\cos\theta) \equiv 1$. Formulas (11) and (12) provide the finite function in the whole Earth–ionosphere cavity for an arbitrary time $t > 0$, including the point where the lightning discharge had been situated. This suggests a possibility of computing the waveform of an ELF pulsed signal (Q–burst) returned to the point of parent stroke.

We depict the ELF pulsed signals in Figure. 4 computed with the use of Eqs. (11) and (12), in which time from the stroke initiation is shown along the abscissa in milliseconds. Two left frames demonstrate the E- (lower frame) and H-field (upper frame) as functions of time. Pulses originate from the positive lightning stroke, i.e., when the electric current flows from the cloud to the ground, so that the vertical electric pulsed field has a negative onset. The current moment of the source was equal to 10^8 A·m, and its spectral density was constant (the “white” source). Computations are based on the heuristic linear frequency dependence of the propagation constant: $\nu(f) = (f - 2) / 6 - if / 100$ (see below).

The left plots of Figure 4 show a set of pulsed waveforms corresponding to different SODs varying with a step of 1 Mm. The curves were gradually elevated of the abscissa to facilitate a comparison of pulses arriving from the distances of 5, 10, 15, and 20 Mm marked by color. One may observe the direct pulse delay growing with the source distance and the antipodal pulse coming closer and closer to the direct wave. At the antipodal 20 Mm distance, the magnetic field turns to zero, while the electric pulse noticeably increases. Besides, the onset of electric field in the direct and antipodal waves has the same sign while the horizontal magnetic field is a succession of ‘pulses with alternating sign’ (see [Nickolaenko and Hayakawa, 2002] for details). The upper right plot of

Figure 4 shows temporal variations of the round-the-world wave, which is the wave that returned to the source point after the “round-the-world” trip. One may see that the propagation time is 159 ms, so that the signal velocity of the pulse is 251.6 Mm/s. The ordinate shows that the pulse onset has an amplitude of -2.81 m V/m, while the second half-wave is $+4.3$ m V/m. For comparison, the major ticks on the ordinate of the lower left plots correspond to 100 mV/m, and this is the amplitude of direct pulse at the distance of ~ 2.5 Mm.

The lower right plot of Figure 4 depicts the distance dependence of the initial negative excursion of the $E(t)$ field together with a set of “standard” functions. In fact, this dependence might be recognized in the sets of pulses collected in the left frames. Computations show how the electric pulse amplitude reduces when the circular wave front extends from a point vertical source. The wave front starts converging to the source antipode after passing the 10 Mm distance. This geometric convergence of the wave is combined with its attenuation in the cavity. This is why the pulse amplitude starts increasing from distances somewhat greater than 10 Mm. Figure 4 shows that the electric pulse acquires the minimum amplitude at the source distance about 15.5 Mm. Since the energy losses increase with signal frequency, the electromagnetic energy at higher frequencies decreases faster, and the signal initially “white” acquires the “reddish” spectrum. This results in a gradual widening of the pulse in the time domain. One may note that the Earth–Ionosphere cavity acts like a low-pass filter with the lower cut-off approximately equal to 100 Hz. Geometric focusing at the source antipode is seen as the electric field increases by approximately 10 dB from its minimum level. Magnetic field is absent at the source antipode. The antipodal focusing of radio waves may partially facilitate the detection of natural ELF transients arriving from great distances.

The wave front extension explains why the pulsed amplitude decreases faster than might be expected from the sole exponential attenuation: $|E| = \exp(-\theta v_2) [\theta/\sin \theta]^{1/2}$ [Nickolaenko and Hayakawa, 2002 ; Nickolaenko and Hayakawa, 2014]. This dependence is shown in the right lower frame by the green stars. It deviates from the amplitude of ELF transient because the monochromatic signal does not experience the spectral modifications during the propagation.

We show only the first pair of pulses in the left lower frame of Figure 4: the direct and antipodal waves. Here we also plotted a few characteristic functions. The red line shows the attenuation of a plane wave with the rate of 3 dB/Mm. The blue, black and magenta lines illustrate the distance dependence of $1/D$, $1/D^{3/2}$ and $1/D^2$ correspondingly. One may observe that the distance variation of ELF transient has its own distinctive outline.

A pair of direct and antipodal pulses returns to the observer after each “round-the-world travel” along the same great circle. This feature might seem odd, because the propagation takes place in the spherical cavity where “all propagation paths are possible”. The following elementary consideration demonstrates that this is not so. Let the vertical point source occupy the pole and emit a single short pulse. The expanding circular wave front initially moves from the source being coincident with a parallel. Then, it crosses the equator and starts converging to the source antipode. After focusing there, the pulsed circular wave re-appears again and propagates from the source antipode to the source point. It crosses the equator once again and merges at the source point. The process continues until the pulse amplitude becomes negligible due to wave attenuation. Imagine that there is an observer positioned at a meridian at some distance from the source. The observer will detect first the circular wave front expanding from the source. In a time, the wave front arrives from the source antipode or from the opposite direction. Thus, the observer detects pulses coming either from the source or from the source antipode, and radio waves arrive in succession from two opposite directions along the same great circle path.

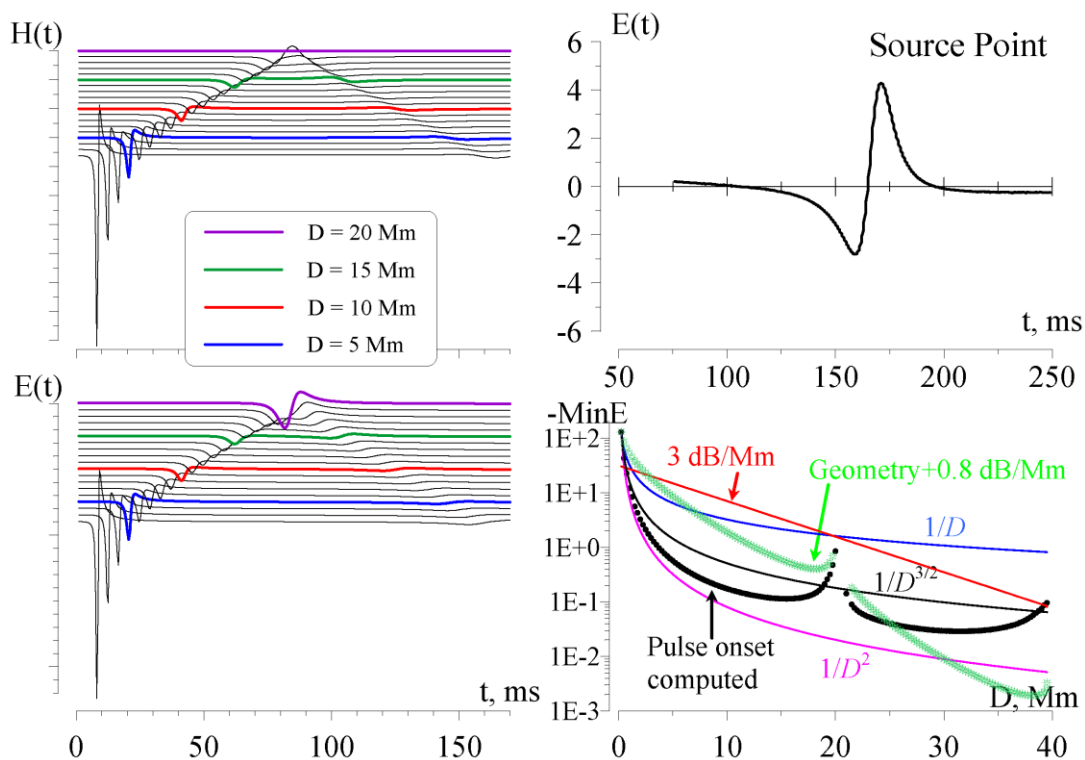


Figure 4: Waveforms of the electric and magnetic pulses computed in the time domain

2.2. ELF propagation

Aspects of ELF propagation have been reviewed in many books [Nickolaenko and Hayakawa, 2002; Wait, 1970 ; Galejs, 1972 ; Bliokh, et al., 1980; Nickolaenko and Hayakawa, 2014; Jones, 1969; Jones, 1970; Porrat and Fraser-Smith 2001; Polk, 1969; Ogawa et al., 1969; Volland,1995; Sentman, 1995; Harth 1982]. The ground surface might be considered a perfect conductor at ELF and the ionospheric plasma is responsible for the particular phase velocity and wave attenuation in the subionospheric radio propagation. The ELF radio waves are partially reflected over a relatively large interval of altitudes. Owing to the low frequency, the ‘C-region’ in the lower ionosphere formed by heavy ions and ion complexes produced by galactic cosmic rays plays a major role in determining the losses in the cavity. The geomagnetic field turns the ionospheric plasma into an anisotropic medium slightly modifying the phase velocity and attenuation and, particularly, the wave polarization. ELF radio signals propagate with the velocity smaller than that of light, and the attenuation rate varies from less than 0.1 dB/Mm at a few Hertz to about 60 dB/Mm at 2 kHz.

The propagation constant is the most important ingredient in the field computations. It was deduced from the experimental data on SR or observations of ELF atmospherics by using the wave impedance data. The simplest model describing the propagation constant as a function of frequency is the linear model [Nickolaenko and Hayakawa 2002 ; Nickolaenko and Hayakawa 2014]. The following linear model was found from SR cross-spectra measure at the Kharkov–Baikal-lake base [Bliokh et.al .,1980]: $\nu(f) = (f - 2)/6 - if/100$. This is a simple, but rather efficient model, and it was used in the time domain solution of SR problem. We demonstrate below a high reciprocity between observations and the time domain computations based on the linear model $\nu(f)$.

The $\nu(f)$ model suggested in [Ishaq and Jones, 1977] is considered to be the most accurate one. It is described by the following relations:

$$\nu(\nu + 1) = (kaS_\nu)^2, \quad (13)$$

where a is the Earth’s radius, k is the wave number in free space, and S is the following complex parameter:

$$S_\nu = c/V - i(5.59) \alpha / f. \quad (14)$$

The real and imaginary parts of the S parameter are specified as follows:

$$\text{Re}[S_\nu] = c/V = 1.64 - 0.1759 \ln(f) + 0.01791 \ln^2(f) \quad (15)$$

$$\alpha = 0.063 f^{0.64}. \quad (16)$$

The propagation constant is found from Eq. (1), which is used in the computations of electromagnetic fields in the Earth-ionosphere cavity.

This model is widely used in the SR computations, although a slightly different approximation was derived for the wave phase velocity by [Huang et al., 1999] from fitting other data of SR observations:

$$\text{Re}[S_v] = c/V = 1.725 - 0.275 \ln f + 0.052 (\ln f)^2 - 0.0036 (\ln f)^3 \quad (17)$$

In spite of visual deviations, Eq. (17) provides the $v(f)$ frequency dependence that departs from that given by Eqs. (13)–(16) by less than 1% in the whole SR frequency band 4 – 40 Hz. Therefore, we use in what follows the model [Ishaq and Jones, 1977] as the standard one.

2.3. Approximate models of atmospheric conductivity

Exponential profile

Conductivity of the lower ionosphere is often modeled by an effective exponential profile. Similar models were used in the VLF band long ago [Wait, 1970; Galejs, 1972], but these appeared to be inappropriate for ELF where a special model was developed [Greifinger and Greifinger, 1978] for monochromatic radio signals propagating in the flat Earth–ionosphere duct. It exploited the fact that E and H fields penetrate into different heights of the ionosphere. The electric field starts to severely attenuate after reaching the lower characteristic height h_0 where the conduction and displacement currents become equal to each other at the given frequency: $\sigma_E(h_0) = 2 \pi f \varepsilon$ (here ε is the permittivity of the vacuum). Magnetic field reaches greater altitudes, and it starts to rapidly decrease from the "magnetic" characteristic altitude h_1 . Here the wavelength in the ionosphere becomes equal to the local scale height of conductivity profile, i.e., the condition is held $\sigma_M(h_1) = [4 \mu_0 \omega \zeta_1^2]^{-1}$, where μ_0 is the permeability of vacuum and ζ_1 is the height scale in the vicinity of h_1 . The technique implies the four parameters of the $\sigma(h)$ conductivity profile; namely, two characteristic heights h_0 and h_1 and two scale heights ζ_0 and ζ_1 in the vicinity of characteristic altitudes for obtaining the complex propagation parameter.

$$S_v = [h_1/h_0]^{1/2} [1 + i(\zeta_0/h_0 + \zeta_1/h_1)\pi/4] \quad (18)$$

The complex parameter S_v and ELF propagation constant at a given frequency depend on the four parameters of the profile. Thus, one must find two functions of height relevant to a particular vertical profile of atmospheric conductivity: the $\sigma(h)$ conductivity itself and the scale height $\zeta(h)$. The

characteristic heights and scale heights are found from these profiles for the given frequency of radio signal f . For example, when the frequency of monochromatic signal is $f = 8$ Hz, the "electric" conductivity is $\sigma_E = 2 \pi 8 \varepsilon = 4.444 \cdot 10^{-10}$ S/m, and we can find the electric height h_0 by using the profile $\sigma(h)$ and relevant scale height ζ_0 from the $\zeta(h)$ profile. Afterwards, we evaluate $\sigma_M = 4.398 \cdot 10^{-4}$ S/m supposing that the scale height of the conductivity is 3 km. Thus we can find the magnetic height h_1 and the scale height ζ_1 . The search for the necessary parameters ends if $\zeta_1 = 3$ km. When $\zeta_1 \neq 3$ km, definite adjustments are necessary, so that any kind of iteration procedure might be organized.

It is clear that such a procedure is inconvenient, and a simplified relation was suggested in [Greifinger and Greifinger, 1978] for finding the magnetic height:

$$h_1 = h_0 - 2\zeta_0 \ln(2k\zeta_0). \quad (19)$$

This formula corresponds to the conductivity profile with a constant scale height, but it is also used in the so-called two-scale models when the magnetic height is found by using Eq. (11), but the actual magnetic scale height is used afterwards (see e.g. [Sentman, 1995]). Additional efforts were necessary for extending this technique to the SR studies. The first, formal obstacle was connected with the spherical geometry of SR problem, and it was not obvious beforehand that the results obtained for the flat waveguide will remain valid in the spherical cavity. Fortunately it appeared that formulas are correct in the spherical cavity, provided that the frequencies exceed a few Hertz [Sentman, 1995; Nickolaenko and Rabinowicz, 1982; Nickolaenko and Rabinowicz, 1987; Sentman, 1990; Füllekrug, 2000]. The following relations were obtained for the SR frequencies and the Q-factors:

$$f_n = [c/2\pi a] \sqrt{n(n+1)h_0/h_1} \quad (20)$$

$$Q_n = [\pi(\zeta_0/h_0 + \zeta_1/h_1)]^{-1}. \quad (21)$$

The second obstacle was the broadband nature of SR signal occupying the band up to 100 Hz and even higher as seen in Figure. 3. Indeed, the above procedure becomes inconvenient when it is necessary to find the variable characteristic heights and scale heights on a profile when the frequency varies in a wide band.

This problem was resolved by introducing the reference frequencies and relevant reference heights. The lower and the upper characteristic heights are found from the following formulas at an arbitrary frequency f :

$$h_0 = G_h + \zeta \ln(f / F_g) \quad (22)$$

$$h_1 = h_0 - 2\zeta \ln(2k\zeta). \quad (23)$$

Here G_h is the reference height and F_g is the reference frequency. The only distinction between the works using the exponential profiles lies in choosing the reference quantities. Various exponential conductivity profiles were described in the literatures providing realistic models of ELF propagation constant. Typical parameters of these profiles are: $G_h \approx 50$ km and $\zeta_0 \approx 3$ km at the reference frequency $F_g = 8$ Hz being equal to the first SR mode frequency. The magnetic characteristic height is found from the equation $h_1 = h_0 - 2\zeta_0 \ln(2k\zeta_0) \approx 95$ km. The scale height ζ_1 might be taken equal to ζ_0 (the single scale model) or to some other value (two-scale model).

We must emphasize that the exponential profile model is just a convenient approximate tool for computing the ELF propagation constant. No difficulties are met when the approach is applied to a given function $\sigma(h)$ for obtaining the $\nu(f)$ function. This result might be compared with the rigorous full wave solution constructed for the same conductivity profile. This was done in [Jones and Knott, 1999] and it turned out that approximate formulas predict the real part of propagation constant $\text{Re}[\nu(f)]$ with the accuracy of 1–2%. But concerning the imaginary part $\text{Im}[\nu(f)]$ or the wave attenuation, the approximate value may deviate from the accurate one by 10–15%.

Knee model

A further development of approximate heuristic models was the “knee model” [Jones and Knott, 1999 24]. It improved the relevance of obtained propagation constant to the standard dependence. In distinction from the two-scale exponential model, the knee model operates with four frequency-dependent parameters. Two of them are the complex functions of frequency interpreted as the characteristic electric and magnetic heights, and the other two are the real functions of frequency and we model the electric and magnetic height scales. The propagation constant $\nu(f)$, which might be used in the calculation of the fields, is computed using standard relations. The complex electric and magnetic height h_E and h_M are found from the following equations at a given frequency f :

$$h_E(f) = h_{KN} + \zeta_a \ln(f/f_{KN}) + \ln \left[1 + (f/f_{KN})^2 \right] \left[(\zeta_a - \zeta_b)/2 + i \left[\zeta_a \pi/2 - (\zeta_a - \zeta_b) \tan^{-1}(f_{KN}/f) \right] \right] \quad (24)$$

$$h_M(f) = h_m^* - \zeta_m \ln(f/f_m^*) - i \zeta_m(f) \pi/2 \quad (25)$$

$$\zeta_m = \zeta_m^* + b_m \left(1/f - 1/f_m^* \right) \quad (26)$$

Here $h_{KN} = 55$ km and $f_{KN} = 10$ Hz are the reference height and the frequency of the knee. The condition is satisfied at the knee height $\sigma(h_{KN}) = \sigma_{KN} = 2\pi f_{KN} \varepsilon$ where $\varepsilon = 8.859 \cdot 10^{-12}$ F/m is the permittivity of free space. Parameters $\zeta_a = 2.9$ km and $\zeta_b = 8.3$ km are the scale heights above and below the knee height. The magnetic reference height and magnetic reference frequency are $h_m^* = 96.5$ km and $f_m^* = 8$ Hz correspondingly. The scale height at magnetic reference frequency is $\zeta_m^* = 4$ km, and the frequency parameter of magnetic scale height is $b_m = 20$ km [Mushtak and Williams, 2002]. Other parameters were also used [Pechony and Price, 2004].

The propagation constant $\nu(f)$ is obtained from the standard expression (13), which is equivalent to the following equation:

$$\nu(f) = [0.25 + (kaS_\nu)^2]^{1/2} - 0.5 \quad (27)$$

The idea of the knee model is that at the frequency of the first SR mode, the characteristic electric height h_E lies below the knee altitude h_{KN} where the scale height ζ_E is large. With the growth in frequency, the electric height exceeds the knee altitude, and the scale height decreases. As a result the quality factor Q_n of SR is reduced at the fundamental mode and remains appropriate at higher modes [Mushtak and Williams, 2002].

The propagation constant found in the knee model corresponds to the standard one, and it became popular in SR computations, especially when the fields are obtained by using traditional formulas (7–10).

However, parameters of the knee model were verbally referred to a certain conductivity profile that never existed. At the same time the works appeared applying the direct modeling of radio propagation by using FDTD or 3DTE (3 dimensional telegraph equation) techniques [Yang and Pasko, 2005; Toledo-Redondo et al., 2013; Zhou et al., 2016]. The self-made conductivity profiles $\sigma(h)$ with a knee were used in direct computations and provided resonance spectra generally similar to the observations. A closer inspection revealed unavoidable departures of these direct solutions from “traditional” ones despite the both of them exploited the “same” knee model [Zhou et al., 2016]. It was demonstrated that the FDTD and the ZHSR give almost coincident results when applying such

a self-made conductivity profiles $\sigma(h)$ that follows from the knee model. In this case the propagation constant was obtained for the profile with the help of rigorous full wave solution. Unfortunately, this $\nu(f)$ dependence noticeably deviated from that found from the knee model by using Eqs. (24–27). This result indicates that the heuristic knee model is rather good for approximating the standard $\nu(f)$ dependence in the SR band. Simultaneously, it is unclear to what a conductivity profile $\sigma(h)$ does this model correspond, provided that such a profile exists at all. In other words, some other, realistic conductivity profiles must be applied when using direct numerical modeling of SR. Any attempts to derive a profile using the knee model result in unrealistic SR parameters. In what follows, we outline a profile $\sigma(h)$ corresponding simultaneously to observational SR and the global electric circuit data.

The propagation constant of ELF radio waves computed using formulas (25–28) of the heuristic knee model is close to the standard model [Volland 1995; Sentman, 1995; Harth, 1982; Ishaq and Jones, 1977]. Completely different data are obtained when computations imply the atmospheric conductivity profile built with the help of characteristic heights and the scale heights of the same knee model. Here, the effect is observed of the approximate physical interpretation of particular elements of the heuristic model. So, this model should be used with caution when interpreting observational data, because the deduced parameters of the profile will provide quite different results when applied in rigorous computations. It would be desirable to use initially the realistic conductivity profile, and such a profile is described in what follows.

Realistic profile

In the field computations and in the interpretation of experimental data, the knowledge is redundant of the vertical profile of atmospheric conductivity. It is sufficient to use the regular expressions for the electromagnetic fields incorporating the propagation constant, the current moment of the field source, and the ionospheric effective height. Information on the atmospheric conductivity $\sigma(h)$ becomes obligatory when using the direct modeling such as FDTD or the 2DTE (two dimensional telegraph equation) technique. The range of heights 30–100 km is crucial in the ELF radio propagation, but it is inaccessible by modern remote sensing. Existing experimental data on the air conductivity here are rare and have been usually obtained by the rocket probes. So, one can find only a limited amount of altitude profiles of the air conductivity in the literature.

In interpretations and modeling the ELF data the classical $\sigma(h)$ profile is often used [Cole and Pierce, 1965]. This profile is shown in Figure 5 by the curve with dots, and the data are listed in Table 1. The major drawback preventing its application in the direct modeling of SR spectra is the

inaccurate propagation constant deviating from the standard model. The new profile [Nickolaenko et al., 2016 ; Kudintseva et al., 2016] is shown in Figure 5 by a smooth line. This $\sigma(h)$ dependence provides a more realistic ELF propagation constant. Simultaneously, it does not seriously deviate from the classical plot, and hence it does not seriously deviate from the traditional data.

The atmospheric conductivity versus height is shown in Figure. 5. The curve with points 1 is the profile [Cole and Pierce, 1965] and the smooth curve 2 depicts the more realistic profile $\sigma(h)$ [Nickolaenko et al., 2016 ; Kudintseva et al., 2016]. Profile 2 has more pronounced alterations in the 50–60 km interval around the knee region. Deviations of two curves start at 30 km altitude, where profile 2 is elevated over the classical plot.

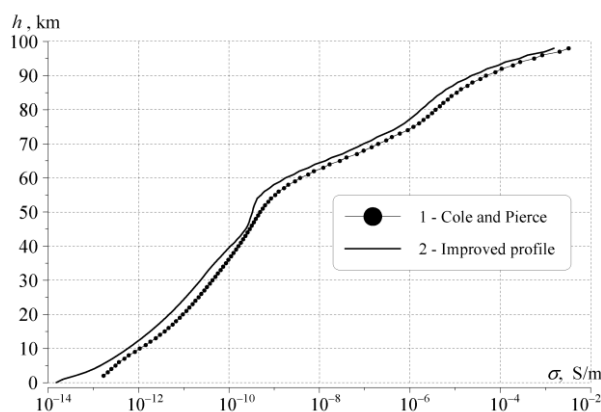


Figure 5: Altitude profiles of air conductivity. Line 1 is the profile [Cole and Pierce, 1965 29] and line 2 is the new profile corresponding to observations of SR and data on the global electric circuit.

The simplified conductivity profiles are widely used in direct methods of field computation. These are typically the $\lg [\sigma(h)]$ plot incorporating the two straight lines forming a kink at the knee altitude. The existence of the upper, “magnetic” characteristic height is often ignored, so that the profiles applied in direct computations are mere two-scale exponential models. On the other hand, an advantage of the direct FDTD, 2DTE, and 3D-TLM (3-dimensional transmission line model) computational techniques is that these are able to incorporate arbitrary vertical profiles and even combine them with some horizontal non-uniformities. Conductivity profile 2 shown in Figure 5 might be used in such computations. It was tested by using the full wave solution followed by the traditional formal description of SR, and we show some of these data.

The ELF propagation constant $\nu(f)$ is usually constructed on the assumption that the ionospheric plasma is isotropic and horizontally homogeneous. The approach is justified by a great wavelength of SR oscillations, because such long waves must be insensitive to “small details” of the cavity such

as the localized or even global non-uniformities. A given conductivity profile corresponds to the complex dielectric constant of the air separating the ground and ionosphere. This medium is supposed to be horizontally stratified, and the electromagnetic problem is formulated for such a configuration. The full wave solution of such a problem exploits waves propagating upward and downward in each slab and the boundary conditions at each interface where the tangential field components remain continuous [Bliokh et al., 1980; Jones and Knott, 1999 ; Madden and Thompson, 1965]. The full wave solution is the rigorous one, and it provides the system of $2N$ linear algebraic equations for the amplitudes of transmitted and reflected waves in each of N layers. The thickness of the layers is much smaller than the wavelength in the medium, and the problem might be reformulated to nonlinear differential equation of the first order (Riccati equation) for the surface impedance [Nickolaenko and Hayakawa, 2002; Hynninen and Galuk, 1972 ; Galuk et al. , 2015]. The latter is the ratio of the tangential components of E and H fields at the boundaries. When reformulated in the Riccati equation, the surface impedance must satisfy the boundary conditions on the ground and at an upper layer in the ionosphere.

Table 1 Logarithm of air conductivity (S/m) as a function of altitude above the ground surface

h km	$\lg(\sigma)$										
0	-13.82	17	-11.25	34	-10.19	51	-9.52	68	-7.35	85	-5.29
1	-16.66	18	-11.17	35	-10.14	52	-9.48	69	-7.17	86	-5.19
2	-12.77	19	-11.09	36	-10.09	53	-9.44	70	-7.02	87	-5.05
3	-12.68	20	-11.02	37	-10.03	54	-9.40	71	-6.85	88	-4.94
4	-12.60	21	-10.94	38	-10.0	55	-9.30	72	-6.72	89	-4.77
5	-12.51	22	-10.88	39	-9.95	56	-9.23	73	-6.55	90	-4.64
6	-12.43	23	-10.80	40	-9.92	57	-9.11	74	-6.37	91	-4.43
7	-12.31	24	-10.74	41	-9.86	58	-9.02	75	-6.25	92	-4.29
8	-12.22	25	-10.67	42	-9.83	59	-8.87	76	-6.12	93	-4.04
9	-12.08	26	-10.61	43	-9.78	60	-8.75	77	-6.02	94	-3.89
10	-11.97	27	-10.55	44	-9.75	61	-8.57	78	-5.93	95	-3.58
11	-11.84	28	-10.49	45	-9.70	62	-8.45	79	-5.83	96	-3.40
12	-11.74	29	-10.42	46	-9.67	63	-8.24	80	-5.76	97	-3.01
13	-11.62	30	-10.37	47	-9.64	64	-8.10	81	-5.66	98	-2.81
14	-11.53	31	-10.32	48	-9.62	65	-7.87	82	-5.58	99	-2.61
15	-11.42	32	-10.28	49	-9.59	66	-7.73	83	-5.49	100	-2.41
16	-11.34	33	-10.24	50	-9.56	67	-7.50	84	-5.40	101	-2.21

This method is regarded as the full wave solution, since it strictly accounts for all the fields propagating in the stratified medium. The full wave solution provides the complex $\nu(f)$ dependence corresponding to a given profile $\sigma(h)$. It is constructed numerically by using the iteration procedure (see [Galuk et al., 2015] for details). Iterations in the full wave solution were performed until the novel value of the surface impedance deviated from the previous one by less than 10^{-7} .

The classical full wave solution has a shortcoming that is revealed when applied in the SR problem. The lower strata of atmosphere have very small conductivity, so that permittivity of air stops varying with the altitude. The solution based on the application of waves in the slabs becomes irresolvable in a sense that the algebraic linear system contains a set of the same equations corresponding to lower layers, and its matrix becomes singular. This is why the full wave solutions in the works [Jones and Knott, 1999; Madden and Thompson, 1965] started from approximately 30 km altitude while the lower slabs were somewhat thicker than the upper strata. This means physically that ELF solutions thus obtained cannot be compared with the data based on measurements of the fair weather electricity in the global electric circuit: these are relevant to different altitude intervals.

This is not so when the full wave problem is formulated in terms of the surface impedance and its solution is obtained by using the Riccati equation. One may include the atmospheric strata of equal thickness ranging from the ground surface to the lower ionosphere edge. Physically this means that a profile might be treated combining the information acquired from measurements both of global electric circuit and the global electromagnetic resonance. This was done in [Nickolaenko et al., 2016; Kudintseva et al., 2016]. Profile 2 in Fig. 5 presents this particular $\sigma(h)$ dependence averaged over the whole globe. It is clear that owing to the global nature of SR, its parameters predominantly depend on the globally averaged properties of ionosphere. Data concerning the mean $\sigma(h)$ profile and its modifications to the ambient day and ambient night conditions might be found in [Nickolaenko et al., 2016]

Frequency variations of the real and imaginary parts of the propagation constant are compared in Figure 6 computed from the formulas of standard model (13–16) and from the full wave solution for profiles 1 and 2 of Figure 5. One may observe that all models give very close values in the real part of the propagation constant (i.e., the phase velocity of radio waves), and deviations do not exceed one percent. However, the peak frequencies in the power spectra of SR are noticeably different (see Figure 7). The reason is simple: a 1% deviation in the phase velocity is relevant to 0.2 Hz deviation at the third SR mode of the 20 Hz peak frequency.

Departures from the standard dependence in the imaginary part or in the attenuation rate are more distinct and they range from –1.5% to 25% for profile 1 and within the $\pm 6\%$ interval for profile 2. Plots in Figure 6 indicate that profile 2 provides the propagation constant close to the reference model in the entire SR band. Therefore, this profile might be recommended for modeling the global

electromagnetic resonance in the Earth–ionosphere cavity, especially when the direct methods of field computations are used.

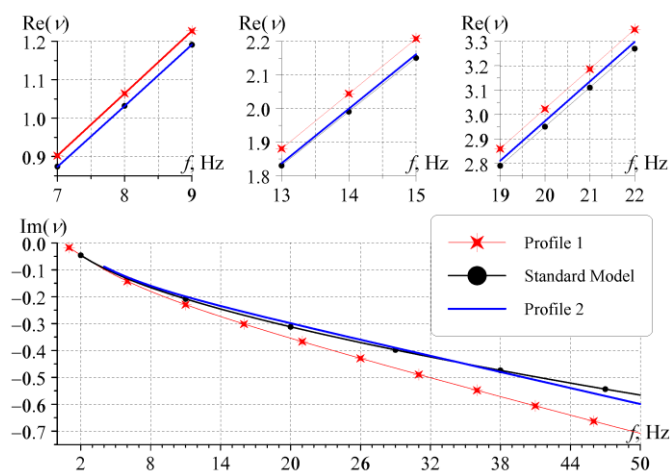


Figure 6: Dispersion curves $\nu(f)$. Upper panels: frequency variations of the real part of propagation constant in the vicinity of the first, second, and third SR modes, and lower panel: the imaginary part of propagation constant.

Validity of the conductivity profile 2 might be also verified by comparing model wave attenuation with the data of direct measurements of the man-made ELF radio signals. These monochromatic radio signals were radiated by the US [Bannister, 1999] and the Soviet [Nickolaenko, 2008] ELF transmitters. Data [Bannister, 1999] were based on the amplitude monitoring of the signal arriving from the US Navy transmitter regarded as the Wisconsin Test Facility. The global network was used in reception of the 76 Hz signal, and the deduced average attenuation rate was $\alpha = 0.82$ dB/Mm for the ambient night and 1.33 dB/Mm km in the ambient day conditions. The average attenuation at this frequency was equal to 1.08 dB/Mm, while the standard deviation due to seasonal variations was $\pm 25\%$. The imaginary part of the propagation constant at this frequency for the profile 2 is equal to $\text{Im}[\nu(f)]|_{f=76} = 0.86$ Napier/rad. By using the relation $\alpha = \pi \lg(e) \cdot \text{Im}(\nu) \approx 1.346 \cdot \text{Im}(\nu)$, we obtain that the relevant attenuation rate $\alpha(76 \text{ Hz}) = 1.17$ dB/Mm. This attenuation is very close to observational data, which is certainly in favor of the model.

The imaginary part of the propagation constant was also published [Nickolaenko, 2008] for the frequency of 82 Hz. The $\text{Im}[\nu(f)]$ was equal to 0.92 Napier/rad, which corresponds to the attenuation factor $\alpha(82 \text{ Hz}) = 1.25$ dB/Mm. This attenuation rate was inferred from the distance dependence of the signal amplitude in the vertical electric field for radio waves emitted by the Kola peninsula transmitter of the Soviet Navy. The model imaginary part of the propagation constant is

$\text{Im}[\nu(f)]|_{f=82} = 0.92$, which is equal to the value measured experimentally. Thus, a comparison with observations of the man-made ELF radio transmissions justifies the conductivity profile 2.

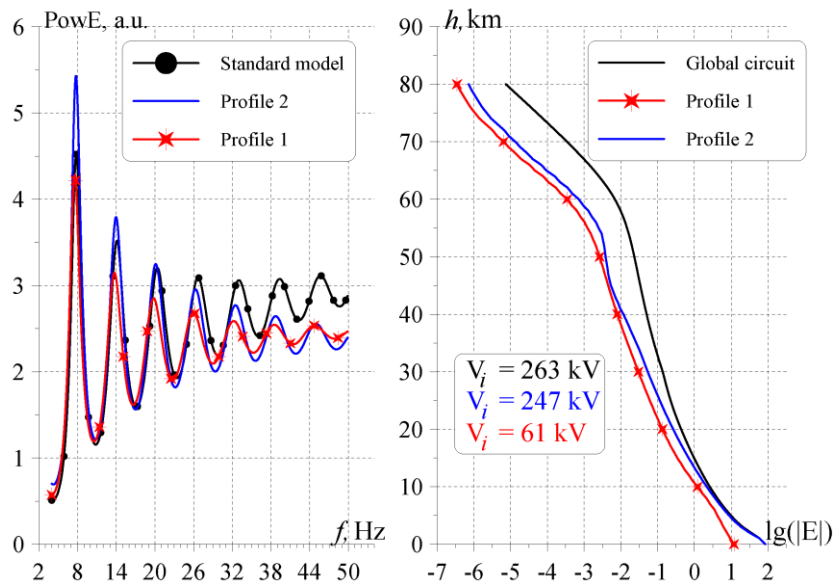


Figure 7: Spectra of SR (left) and altitude variations of vertical gradient of atmosphere potential (right)

The propagation constant is further applied in the field computations. To compare results obtained with the profiles 1 and 2 and the reference model, we turn to the power spectra of the vertical electric field component. To compensate the distance dependence of SR spectra, we used the globally uniform spatial distribution of field sources. The power spectrum is described for such a distribution by the following equation [Nickolaenko and Hayakawa, 2002; Bliokh, et al., 1980; Nickolaenko and Hayakawa, 2014]:

$$|E(f)|^2 \approx \left| \frac{\nu(\nu+1)}{\omega} \right|^2 \sum_{n=0}^{\infty} \frac{2n+1}{|n(n+1) - \nu(\nu+1)|^2} \quad (28)$$

Here the “white” source is used, and the power spectrum $\text{Power } E = |E(f)|^2$ is measured in arbitrary units.

Three SR spectra are shown in the left frame of Figure 7. The black line with dots shows the power spectrum obtained in the standard ELF radio propagation model, red curve with stars corresponds to profile 1, and blue line presents data for the profile 2. These plots suggest that profile 1 generally overestimates the losses in the Earth–ionosphere cavity, so that the resonance pattern becomes less pronounced and the peak frequencies and intensities are smaller than the observed values. Profile 2 provides data closer to the standard spectrum, especially in the vicinity of the first three SR modes that are usually used for inferring geophysical information from resonance data.

The right panel of Figure 7 compares the height variations of the fair weather field. The black curve corresponds to the conductivity profile derived from the global circuit data [Rycroft et al., 2000a; Rycroft et al., 2000b], the red curve with stars shows the profile 1 data, and the blue curve depicts results pertinent to profile 2. The altitude above the ground is shown on the ordinate in km, and the abscissa depicts the decimal logarithm of vertical electric field in V/m. The strength of the fair weather field was obtained from the Ohm's law: by multiplying the air resistance $\rho(h) = 1/\sigma(h)$ by the density of leakage current of the global circuit $j = 1.5 \text{ pA/m}^2$ [Rycroft et al., 2000b]. Relevant fair weather field on the ground level becomes equal to 99 V/m for profiles 1 and 2, but it is only 14 V/m for the profile [Cole and Pierce, 1965]. After integrating the field strength over altitude, we find that the ionosphere-to-ground potential difference V_i is equal to 263 kV in the model of global circuit, and 247 kV for profile 2, and only 61 kV for the profile in [Nickolaenko et al., 2016 ; Kudintseva et al., 2016]. The latter value is exceptionally low. Thus one may conclude that profile 2 provides realistic results when used for the field computations in the frequency band ranging from 0 to 100 Hz at least.

3. Natural ELF waves

3.1. Stationary ELF waves (SR)

Sources

Signals of global electromagnetic resonance are detected in the power spectra of vertical electric or the horizontal magnetic field components. Sources of natural ELF radiation are the lightning strokes occurring worldwide. All necessary details on the terrestrial lightning might be found in [Nickolaenko and Hayakawa, 2002 ; Nickolaenko and Hayakawa, 2014; Porrat and Fraser-Smith, 2001; Polk, 1969; Ogawa et al., 1969; Volland, 1995; Sentman, 1995; Harth, 1982 ; Rycroft et al., 2008]. Because of the low attenuation, the ELF pulse emitted by a lightning discharge is able to multiply return to the observer after "circling the globe". Natural ELF radio noise is a superposition of pulses arriving from lightning strokes at a rate about 100 events per second.

SR is observed as a succession of peaks between 4 and 40 Hz in the power spectra of E and H fields. The upper limit of SR observations is conditioned by the radiation of power supply lines (50 or 60 Hz), and we observe the geomagnetic pulsations and ionospheric Alfvén resonance below this band [Surkov and Hayakawa, 2014]. The major source of SR electromagnetic energy is radiation from lightning strokes, and owing to low frequencies substantial contribution is made by continuing currents of lightning. Only the strokes with large continuing currents are detected at ELF, which

might pass unnoticed in the other frequency band. So, data on the global lightning distribution might deviate when inferred from the SR and from the VLF band (a few tens of kHz frequency)

Individual discharges are random, and their parameters may vary substantially. Even nowadays, finding the global distribution of lightning strokes is not a simple task (e.g. [Hutchins et al., 2012]). Thunderstorms occur in many locations, and there are approximately 2,000 of them over the whole Earth. The strokes tend to occur over the land rather than over the sea. Therefore, there exist three global thunderstorm centers: the maritime continent in the South-East Asia, equatorial Africa, and America. Maximum of the local lightning activity is observed in the afternoon hours, so that the global thunderstorms move around the globe. Daily activity starts in Indonesia during morning hours of universal time (UT), it “steps” over the Indian Ocean to Africa in the afternoon and moves to America in the evening. Global thunderstorms cease late in the UT night when the Pacific Ocean occupies the sunny side of the globe. Seasonal and annual variations are caused by motion of the Sun in the sky being simultaneously connected with the local climate and weather.

The ELF waves are sensitive only to the ‘large scale’ elements in the thunderstorm distribution. At the first 8 Hz SR mode, the ‘insignificant details’ like continents are not resolved. So the simplest model of a single lightning center is successfully used at the first resonance mode. The single equatorial global thunderstorm center is usually placed at the 17-18 hr local time, and it has the size from 1/4 to 1/3 of the Earth’s circumference. Such a source follows the Sun during a day and slightly drifts to the north or to the south in summer and winter.

About 2,000 thunderstorms are permanently active over the planet, each of them covering the characteristic area of 1,000 km² and maintaining the rate of global lightning of 50–100 strokes per second. A thunderstorm cell provides the median current of 1 A to preserve the equilibrium in the global electric circuit. A median lightning stroke transports a negative charge of about 20 C to the ground, and a thunderstorm generates a median return stroke every 20 seconds. More detailed information on the global lightning activity might be found in the special literature (see [Polk, 1969; Ogawa et al., 1969; Volland, 1995; Sentman, 1995; Rycroft et al., 2008; Rycroft et al., 2000b; Hutchins et al., 2012; Rakov and Uman, 2013] and references therein).

Instrumentation

Owing to the huge man-made interference, a SR observatory should be placed far away from the industrial regions, transportation facilities, power supply lines, and populated area. A typical SR observatory exploits a vertical electric antenna and a couple of orthogonal horizontal magnetic

antennas. The detailed description of ELF antennas might be found in the monograph [Burrows, 1978]. The vertical electric antenna is an electrode (usually spherical) mounted on an insulator. Specific geometric shape of the electrode is not important, and it is desirable that it has a large self-capacity (20-30 pF at least) which might be easily calculated. The electrode is connected to the pre-amplifier with a typical input impedance of 10^9 Ohms, and the input capacitance of less than 100 pF. Afterwards, the SR signal is fed to the receiver with a gain of 60 dB and a dynamic range of at least 120 dB.

The electric antenna must have the frequencies of mechanical vibrations beyond the working frequency band. Usually this means that carrying construction is not very rigid, and the antenna active electrode is rather massive. The effective height of a vertical electric antenna increases with elevation of its active electrode regardless the conductivity of the carrying construction: the mast might be made of an insulator or a metal. One may imply that the effective height of vertical electric antenna is approximately equal to one-half of its elevation above the ground. The exact value should be established by using the procedure of antenna calibration (see [Nickolaenko and Hayakawa, 2002 ; Nickolaenko and Hayakawa, 2014] for details).

The ELF magnetic antennas are usually the induction coils with many turns winded on the ferromagnetic core of high magnetic permeability. Antennas have the sensitivity angular pattern of lemniscata (the 8-form), and one has to use a couple of orthogonal antennas to detect signals arriving from any arbitrary direction.

The voltage induced in the magnetic antenna coil is the product of the time derivative of the outer magnetic induction B and the effective area of antenna winding S_{eff} . The design of magnetic antenna must provide the greatest possible effective area, which depends on the geometry of the core (the length and diameter), the material of the core, number of turns, and the type of winding. The latter controls the average cross-section of a turn and the mutual capacitance of turns. This capacitance combined with the antenna inductance causes undesired resonances in the magnetic antenna sensitivity. The number of turns N usually reaches 100,000. The winding is split into ~10 sections set at the cover of the ferromagnetic core. The core is usually ~1 m long and has a few centimeters in diameter. It is made of a ferrite or the isolated permalloy leafs firmly placed in the plastic wrapping.

It is known that a ferromagnetic body “draws in” the outer magnetic field lines. The volume from which the field is collected increases when the core becomes longer (its orientation is parallel to the outer field). The following approximate formulas are valid for a majority of magnetic antennas. The effective permeability of the core is:

$$\mu_{\text{eff}} = (m_l/m_p)^2 [\ln(2m_l/m_p) - 1]^{-1} \quad (29)$$

where m_l is the half-length of the core, and m_p denotes the core diameter. The effective area might be evaluated from the following.

$$S_{\text{eff}} = \pi (m_l)^2 N/3 \quad (30)$$

The physical meaning of the last equation is that the effective area of a magnetic antenna with a ferromagnetic core is approximately equal to that of the air loop antenna having the diameter equal to the semi-axis of the core m_l . These formulas are approximate and correspond to the material permeability of the core $\mu \gg 1$. In practice this means that $\mu > 1,000\text{--}2,000$. These equations are useful for preliminary estimates of a future antenna size, while the exact computations must be made by using rigorous and more complicated equations [Burrows, 1978]. Eqs. (30) and (31) explain the relative invariance of the magnetic antenna design: all antennas described in the literature have the core 1–2 m long, the diameter of a few centimeters and $N \approx 100,000$ turns.

Another type of antennas is also used, and the most common is the horizontal wire antenna grounded at its ends. Physically such an antenna is equivalent of a one-turn vertical loop antenna (magnetic antenna) with the area of about its squared length.

The signal from the output of antenna pre-amplifier is usually fed through a twisted pair cable to the SR receiver positioned in the laboratory room at ~ 100 m distance from the antennas. A typical receiver is the low frequency amplifier with the gain about 60 dB and dynamic range not less than 120 dB. Its role is the signal conditioning for the Data Acquisition System (DAS), habitually placed in a PC. This usually means that the receiver band-pass is formed by the standard high-pass and the low-pass filters of 4 – 6 order, and the total amplification provides the RMS output signal amplitude of about 1 V. The DAS exploits the analog digital converters (24-bit sampling is preferred) working at the sampling rate a few times higher than the higher cut-off frequency of receiver. As a rule, the SR receiver has the bandwidth 4 – 40 Hz, and the sampling frequency is about 200 Hz. The DAS is often synchronized by 1 s time stamps from GPS, and this allows us to compare the records autonomously performed at remote observatories. The digital record is stored in the PC memory for further analysis and processing.

The current processing and averaging of observational data are performed to reflect the major results of SR monitoring, and these are displayed on the PC monitor. The first step in such a processing is obtaining the power or amplitude spectra of the time domain records. This is done using Fourier transform of the $U(t)$ realization. To stabilize results of measurements, one usually performs the data accumulation in the time domain, an 'automatic' averaging takes place in this case and the results become stable. An increase in the duration of the time domain record does not make the spectral estimates stable. According to the localization principle of Fourier transform, an increase in duration T of the time domain record simply raises the spectral resolution $\Delta F = 1/T$. Physically this means that spectral densities become independent, provided that their frequencies are separated by ΔF or a greater amount.

This feature is seen in the plot of Figure 8 where the amplitude spectrum is shown of the SR signal recorded by the receiver of 100 Hz band-pass with the sampling rate of 200 Hz at Tiksi settlement (71.584°N and 128.768°E) [Ayurov and Bashkuev, 2016]. The amplitude spectrum in Figure. 8a is based on the records of 470 minutes duration. We easily recognize the resonance modes in the radio noise spectrum that looks like a noisy strip and an enormous peak relevant to the power supply of 50 Hz.

The averaging procedure must be applied for the stabilization of spectra. This goal can be achieved by applying the spectral windows convolving the "raw" spectrum and a special window function. The windowing procedure averages the adjacent spectral densities and thus exploits the principle of localization. Since the spectral densities are independent, averaging over the frequencies becomes an equivalent to averaging over an ensemble of realizations with a concurrent reduction in the frequency resolution. Averaging over the frequency in Figure 8a was performed with the narrow spectral window of 16 frequencies. If one applies the wider spectral window, deviations at adjoining frequencies will be reduced, and there will appear the SR pattern.

After applying such a procedure to the SR record, one obtains the hourly spectra shown in Figure 8b and 8c where SR modes are clearly seen. Here, the same receiver and the same sampling rate are used. Duration of the record is 60 minutes now and the wide spectral window is used averaging spectral data over 1024 points.

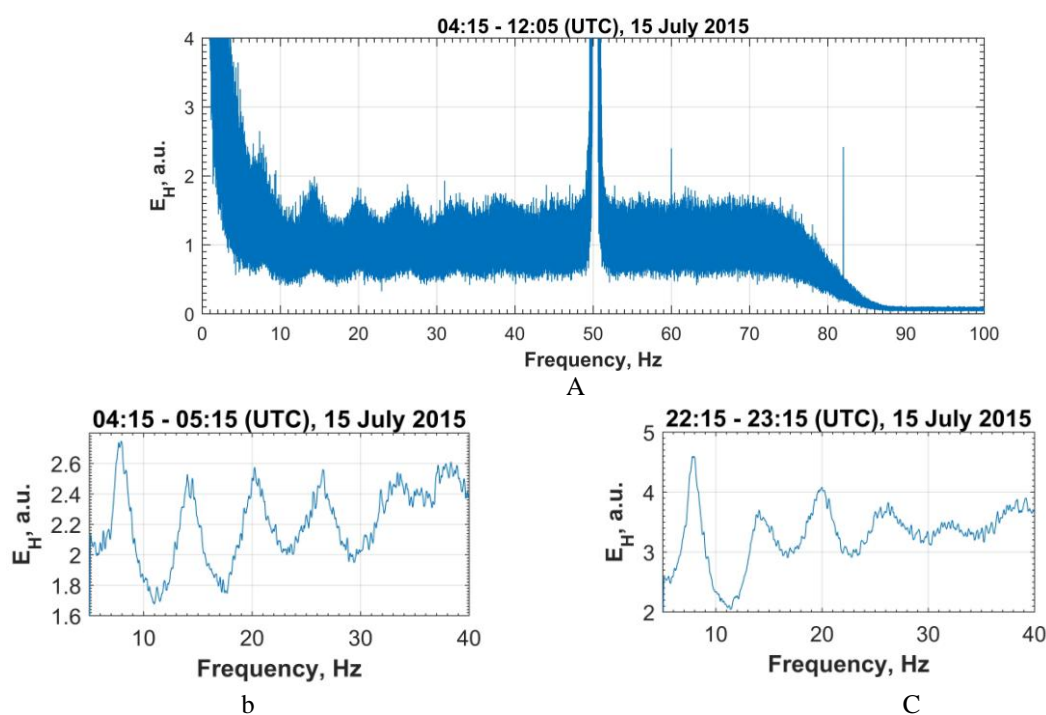


Figure . 8 Fourier transforms of continuous ELF record at Tiksi (71.584°N and 128.768°E) [courtesy of Ayurov and. Bashkuev]

There are many procedures of data processing that are based on similar, but other algorithms. Most often, a record is divided into fragments of standard duration about 10 s, which provides the 0.1 Hz spectral resolution. Elementary spectra are computed by applying FFT to these fragments. The power spectra thus found are averaged over 5 or 10 min intervals (30 or 60 spectra are averaged in an hour). Such a processing reduces random fluctuations present in elementary spectra as these do not repeat from sample to sample, while the SR pattern is continuously replicated in all the segments, and so the resonance lines become rather smooth [Nickolaenko and Hayakawa, 2002 ; Bliokh, et al., 1980 ;Nickolaenko, and Hayakawa, 2014].

Spectra of SR are observed in the power spectra of different field components. Sometimes, the cross spectra are used. For example, the spectra $\langle E(f)H_X(f)^* \rangle$ and $\langle E(f)H_Y(f)^* \rangle$ are the components of the Umov–Poynting vector, where $E(f)$ is the complex spectrum (Fourier transform) of vertical electric field, $H_X(f)^*$ and $H_Y(f)$ are complex conjugate of complex spectra of orthogonal horizontal magnetic field components ($H_X = H_{WE}$ and $H_Y = H_{SN}$), and the angular brackets denote averaging over the ensemble of spectra of elementary realizations. The cross-spectra of magnetic fields $\langle H_X(f)H_Y(f)^* \rangle$ and $\langle H_X(f)^*H_Y(f) \rangle$ detected at the same observatory are used in measurements of the field polarization. The cross-spectra of records obtained at different sites are also used [Nickolaenko and Hayakawa, 2002 ; Nickolaenko and Hayakawa, 2014].

As a rule, the primary information in the spectral form is stored in the computer memory. The secondary processing of records is performed with the spectra, and parameters of resonance modes are deduced. Each mode is characterized by its amplitude, peak frequency and Q-factor or relative width at the half-power level. The fine structure is always present in observed spectral data, and the spectral parameters are deduced by using some kind of data smoothing. The fitting by a Lorentzian curve is most popular, which is known in a mathematical analysis as a Cauchy curve or Cauchy–Lorentz distribution function. It has a pole in the complex frequency plane so that $y(f) = y_0 + A/[(f - f_n)^2 + (1/2 f_n/Q)^2]^{-1}$ where y_0 is a constant, A is the resonance amplitude, f_n is the resonance frequency, and Q is the quality factor of resonance oscillations connected with the width of resonance line.

An alternative processing of spectra is the Rice approach [4] when the resonance line $S(f)$ is considered as the probability density function of the continuous frequency, so the relation is valid $f_n^2 = W_2/W_0$ where $W_2 = \int_{f_1}^{f_2} S(f) f^2 df$, $W_0 = \int_{f_1}^{f_2} S(f) df$, and integration is performed in the vicinity of spectral maximum. Usually, the intervals are used of 8 ± 1.5 , 14 ± 1.5 ; 20 ± 1.5 Hz, etc. Such a processing is similar to the SR mode trackers [Nelson, 1967; Satori et al., 1996].

4. Some observational results

The above listed parameters of resonance are used in geophysical applications: median values and the diurnal, seasonal, and inter-annual variations. The major cause of regular variations of SR parameters is motion of the field sources relative to the observatory combined with a relatively low quality factor of cavity. There is no problem to explain an origin of diurnal variations in the resonance intensity by the motion of global thunderstorms around the Earth.

The motion is clearly seen in the daily variations of the median arrival angle of ELF radio waves established using the orthogonal components of Umov–Poynting vector. Such records show both the displacement of the lightning activity in respect to the observatory and the relevant increases in intensity when the waves arrive from the global thunderstorm centers (see Figure 4.4 in [Nickolaenko and Hayakawa, 2014]).

Figure 3 indicates that alterations in the SOD modify the observed intensity of resonance modes due to spatial modal structure and the wave attenuation. These modulations impede monitoring of the thunderstorm intensity itself. The easiest way to reduce the impact of modal structure is application of resonance intensity integrated (summed) over three modes. Individual spatial distributions

compensate each other, and an impact of SOD becomes substantially reduced in the integrated SR intensity [Nickolaenko and Hayakawa, 2002 ; Nickolaenko and Hayakawa, 2014]. Application of simultaneous records at widely separated observatories allows us to separate diurnal variations occurring the universal and local time as seen in Figure. 9.

The signal processing technique applied was suggested in [Sentman and Fraser, 1991] and improved in [Pechony and Price, 2006]. It exploits the simultaneous SR records at observatories widely separated along longitude. Data presented in Figure 9 were obtained from the records of Moshiri (44.4°N, 142.2°E), Lehta (64.4°N, 34°E), and West Greenwich (41.6°N, 71.6°W) [Nickolaenko et al., 2011]. The output data are the coherent diurnal variations occurring in the Universal time (UT), which reflect the pattern of global thunderstorm activity pertinent to different months and years estimated from the SR records. The daily changes reach the factor of 2, and the seasonal trend is of similar value with the maximum during boreal summer. The patterns for a month tend to repeat year after year, which indicates the general reproduction of thunderstorm activity from year to year.

Figure 9 demonstrates results of reconstruction of the source intensity from the global resonance data for every month of the year except July. These data are missing due to strong interference for local thunderstorms at the observatories: we did not have simultaneous records at all the three sites, and so processing was impossible. Resonance intensity recorded at an observatory is a convenient characteristic, which is often used in different applications, but it depends on two factors: the intensity of the source itself and the SOD. The source intensity variations are present in all records and occur coherently in the UT. Alterations caused by diurnal motion of thunderstorms around the globe take place in the local time. Separating these two factors is a crucial task when working with the SR intensity. It is clear that the Q-factor or relative width of resonance peak alters when the height of a given peak changes against that of adjacent peaks. Thus, variations of SOD cause diurnal modulations in the Q-factors. Simultaneously, the source motion in a cavity of relatively low quality-factor modifies the position of resonance peaks over the frequency axis due to interaction of adjacent modes. Diurnal frequency pattern is the simplest one at the first SR mode because the spatial distribution of relevant fields is plain: it is proportional to the cosine or to the sine functions of angular SOD. Correspondingly, the 1st mode frequency in the vertical electric field component has a discontinuity at the nodal distance of 90° or 10 Mm. The discontinuity turns into a fast variation of finite range $df_1 = f_{MAX} - f_{MIN}$ when the field sources occupy some area of width W [Wait, 1970 3]. One can estimate diurnal variations of the effective zone occupied by thunderstorms W by using the

calibration curve $W(df_1)$ (see [Nickolaenko and Hayakawa, 2002; Nickolaenko and Hayakawa, 2014]). The first mode frequency in the horizontal magnetic field is proportional to the SOD, and this dependence might be used to monitor diurnal, seasonal and inter-annual motion of global thunderstorms [Nickolaenko et al., 2015].

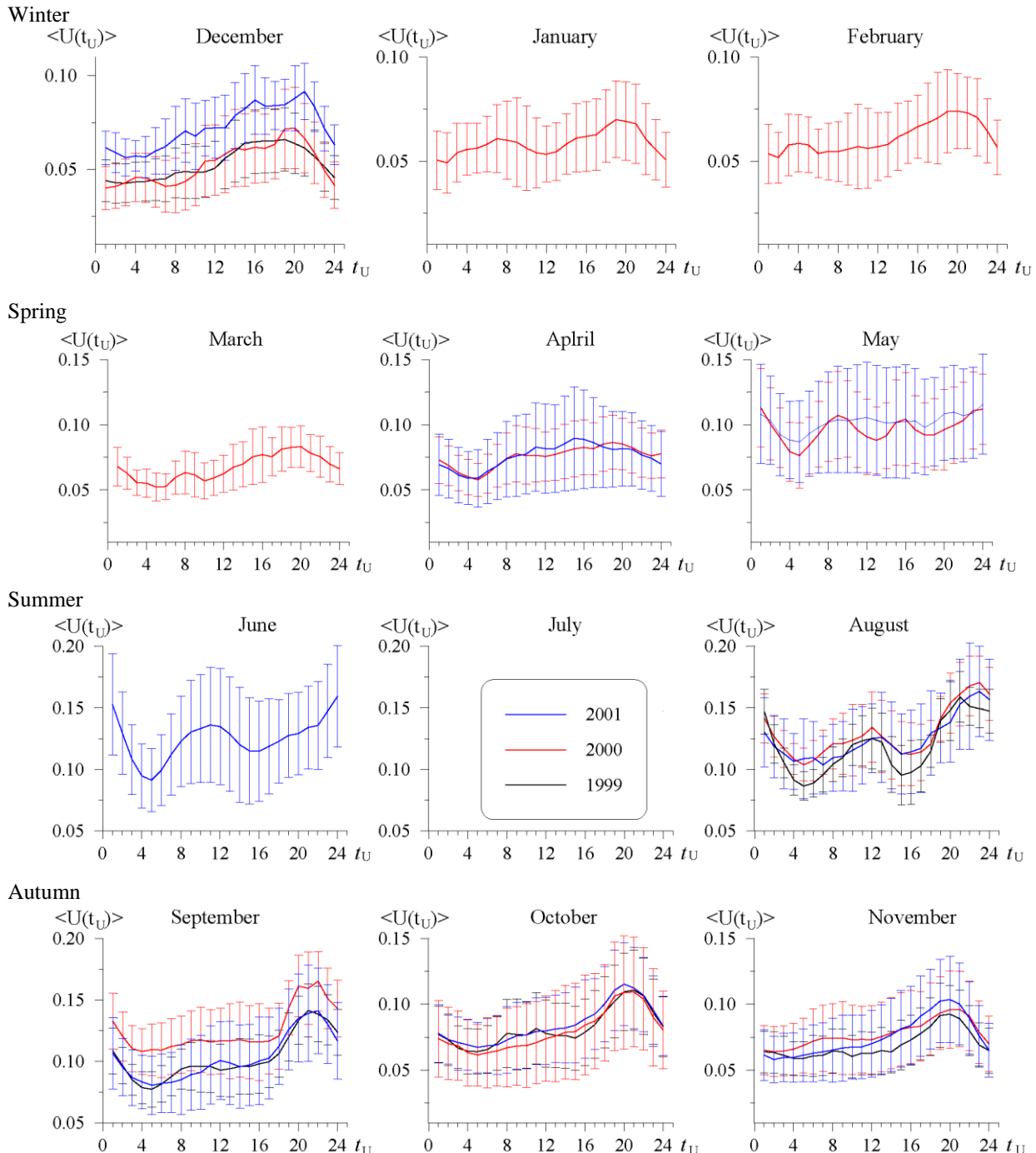


Figure 9: Diurnal/seasonal variations of global thunderstorm activity deduced from simultaneous SR records at Moshiri, Lehta and West Greenwich. The data of July are missing due to the strong interference by local thunderstorms at these stations.

By applying the above properties of SR, the following estimates were obtained that agree with other observations. The intensity of global thunderstorm activity varies by a factor of 2–3 during a day and approximately by the same amount during a year, this latter variation being observed like a trend. The two-three-fold inter-annual variations are also revealed by SR monitoring. The characteristic size of a compact area occupied by lightning strokes varies from ¼ to 1/3 of Earth circumference. In addition to the compact area, a half of global thunderstorms are uniformly distributed in equatorial belt around the equator. Seasonal drift of thunderstorms is estimated by SR data as 2–2.5 Mm.

4.1 SR as a global thermometer

The idea that SR intensity might be used as an indicator of current global thunderstorm activity was spelled in [Williams, 1992], which demonstrated the similarity of the long-term alterations in temperature anomaly and intensity of the first SR mode. Additional experimental evidence was presented in [Sekiguchi, et al., 2006] showing a high correlation between SR intensity recorded at the Moshiri observatory in Japan and the global soil temperature in different latitude intervals. The following relation was obtained for the SR intensity I measured in dB relative to 1 pT^2 and the ground surface temperature in centigrade T measured in the latitude interval from 60°S to $+60^\circ\text{N}$:

$$I [\text{dB}] = - 13.64 + 0.648 T \quad (31)$$

The following relation is valid for the temperature deviations (anomaly) ΔT from the median value $\langle T \rangle = 16.96^\circ\text{C}$ in this interval:

$$I [\text{dB}] = - 0.077 + 0.679 \Delta T \quad (32)$$

Relevant data are shown in the upper frame of Figure 10. The abscissa shows the months from November 1998 to May 2002. The black curve with stars depicts the observed SR intensity in dB relative to 1 pT^2 . The red smooth curve demonstrates the estimate for the resonance intensity retrieved from the temperature observations in the $[60^\circ\text{S} - 60^\circ\text{N}]$ latitude interval by using Eq. (32). As one might observe, the correspondence of these two curves is rather good.

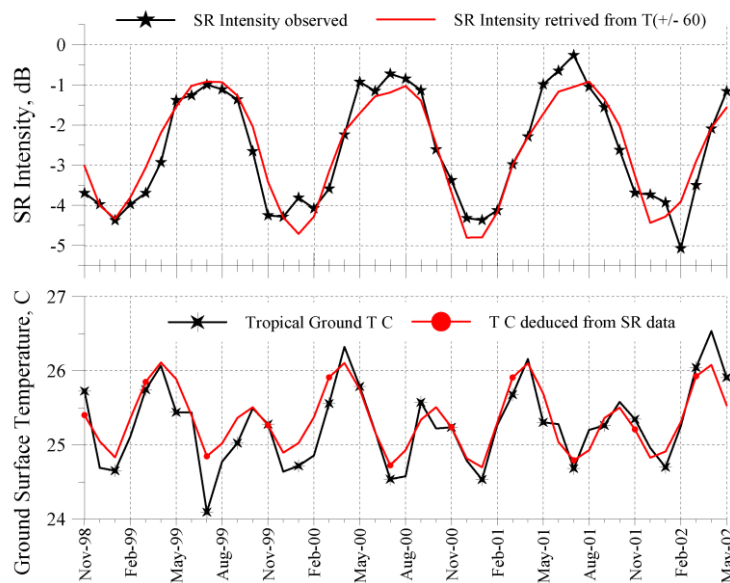


Figure 10: Seasonal variations of SR intensity and the ground temperature data

The lower plot of Figure 10 presents the situation with “inverse” modeling. Here, the ground surface temperature was computed by using SR records (red line with dots) for the symmetric latitudinal interval $\pm 20^\circ$. Processing of ground surface temperature and ELF data collected at Moshiri allowed obtaining the following relations [Sekiguchi, et al., 2006]:

$$\Delta P_{AN}[\text{dB}] = -2\cos(M\pi/6), \quad (33)$$

where ΔP_{AN} is the annual component in variations of the resonance intensity at Moshiri, and M is the month number ($M=1$ corresponds to January). The temperature anomaly ΔT_{20} in the tropical belt $20^\circ\text{S}–20^\circ\text{N}$ is described by the heuristic equation:

$$\Delta T_{20}[\text{°C}] = 0.55\cos(M\pi/3) - 0.3\cos(M\pi/6) = 0.55[1 - 0.5(\Delta P_{AN})^2] - 0.3\{[1 - 0.25(\Delta P_{AN})^2]^{1/2}\} \quad (34)$$

The red curve was reconstructed from the recorded annual variations of SR intensity by using Eq. (34). The black curve with stars in the lower panel of Figure. 10, depicts the space-borne observations of the ground surface temperature within the tropical belt. Again, outstanding correspondence is present between the observed ground surface temperature anomaly and the estimate deduced from the SR intensity. Unfortunately, the data available in [Sekiguchi et al., 2006],

covered only 42 months of continuous observations. The comparison of longer records would be desirable.

4.2 “Terminator effect” in SR records

The term “terminator effect” appeared when the long-term records of signal amplitude (intensity) were arranged over the month–local time plane [Melnikov et al., 2004]. We show this plot in Figure.11d, and the data were collected at Mitspe Ramon observatory (31° N and 35° E) in Israel. The frame (d) depicts the seasonal–daily variations of the amplitude of the first SR mode recorded in the vertical electric field component averaged over four years of observations (1999 – 2002). The months are shown along the abscissa ranging from Jan. 01 to Dec. 31, and the local time is plotted on the ordinate in hr. The color indicates the relative field amplitude, with higher levels being red.

The characteristic lens-like form of diurnal–seasonal variations was present in the records of three SR modes recorded at many observatories, e.g. Nagycenk (47.6°N and 16.7°E). The observational data showed the simultaneous increase in the electric and magnetic fields reaching 30%. The lens-like patterns were attributed to the influence of the day–night non-uniformity of the Earth–ionosphere cavity because the abrupt increase/decrease in amplitude was found in the vicinity of local sunrise and sunset. The day–night interface is called solar terminator; therefore the phenomenon got the name of “terminator effect”. The above work did not support the conclusion by computational data, while the published model data showed that the effect of ionospheric day–night non-uniformity is about 5–10% at SR. The point is that since the SR is a global phenomenon, its amplitude depends predominantly on the level of thunderstorm activity, and therefore the daily patterns at different observatories must have the universal character. The day–night non-uniformity provides a secondary effect.

The picture of lens–like variations made a great impression, and similar variations were found in the records of many sites. However, none of experimental works discussed a possible formal interpretation, and these ignore the model results [Rabinowicz, 1988; Pechony, 2007; Pechony et al., 2007; Nickolaenko et al.; 2006a, Nickolaenko et al., 2006b]. The model data [Pechony, 2007; Pechony et al., 2007] are shown in panels a – c of Figure. 11, relevant to the same Mitspe Ramon observatory. Computations shown in this figure were made for the uniform Earth–ionosphere cavity with the help of 2DTE.

Before discussing the data of Figure 11, we mention the major features relevant to the genuine terminator effect.

1. The impact of ionospheric non-uniformity might be observed in the two distinct propagation geometries: when the propagation path is positioned in the ambient day or in the ambient night conditions. According to the wave diffraction concept, a propagation path is the source–observer great circle arc surrounded by the first Fresnel zone of the field. One can speak about propagation in the day (night) conditions when the first Fresnel zone is found within the day (night) hemisphere. This condition is not held at the first SR frequency when the SOD is a few Mm because the first Fresnel zone covers the whole globe. Hence, the ELF radio wave ‘does not resolve’ the day and night hemispheres, and it propagates in an average uniform cavity (we can call it the “dusk” or the “dawn” resonator). The formal day or night propagation conditions are realized at the fourth SR mode and above, which occurs at frequencies above those addressed here. We will briefly discuss in what follows the impact of day–night non-uniformity on the artificial ELF radio signals.

2. The second feature is the frequency dependence of wave diffraction pattern: variations become faster and sharper with an increase in the signal frequency. When turning to SR modes 1, 2, and 3, we note that the relevant wavelength becomes shorter by the factor of 2.5. This means that variations caused by the wave diffraction at the third mode must be faster and have the period 1.6 times shorter than those at the first mode. In case when the patterns observed at different modes have the remarkable similarity, the driving mechanism was not the wave diffractions, and most probably it was the effect of variable source intensity.

3. The ionospheric height varies from ~60 to ~90 km from day to night, which means that median height is 75 km and the day–night asymmetry is ± 15 km or 20%. This modest deviation in the cavity height will cause a redistribution of the electric and magnetic field amplitude: the electric field will be concentrated on the dayside and the magnetic field on the night side of the globe. However, the following conservation law must be satisfied: the complete electromagnetic power remains a constant in the unit volume of the cavity $|\epsilon_0 E|^2 + |\mu_0 H|^2 = const$. The physical idea is simple, if this condition is not held, the power will flow from the places of high concentration to those of its lower value until the equilibrium is established. This feature means that an increase observed in the electric field at a point is combined by the equivalent decrease of the magnetic field at this point, provided that alterations were caused by the non-uniform cavity height. In other words, since the electric field concentrates on the dayside of the lower height, the magnetic field is reduced here. At the same time, the magnetic field relocates to the higher side where the electric field is smaller. Therefore, the lens-

like structure driven by the cavity height must have the opposite sign (an increase versus a decrease) when observed in the electric and in the magnetic fields. Again, a simultaneous modulation of the both field amplitudes must be attributed to the variable intensity of the source.

Analyses of observations and modeling indicate that the “terminator” effect is reflection of the everyday development/cease in the global thunderstorm activity observed at the sites occupying specific longitudes. The daily onset of the global lightning activity in the South-East Asia is coincident with the sunrise at the European observatories, while its ending in America West coast is close to the passage of evening terminator over the Europe.

Three source models were used in the computations shown in Figure 11. The upper left frame (a) shows the results for the point source of constant amplitude. The source is positioned at the latitude retarded from the noon point by 3 hr (at the local time of 15 hr). Its latitude varies with the season by $\pm 22.5^\circ$: the source is an equatorial one during the equinoxes, and it drifts to the North and to the South in accordance with the boreal summer and winter seasons. The lens-like pattern is clearly seen in the model data of Figure 11a, and the amplitude maximum is observed when the source approaches the observer (15 hr local time). The point source model has a serious drawback: the first mode amplitude also increases when the source of constant intensity is positioned near the observer antipode (the local time of 3 hr). Figure 11b presents a more realistic source model when global thunderstorms are concentrated at the same point, but they become active only over the land. The antipodal peak vanishes in this case because the observer antipode is found in the Pacific Ocean where thunderstorms are rare.

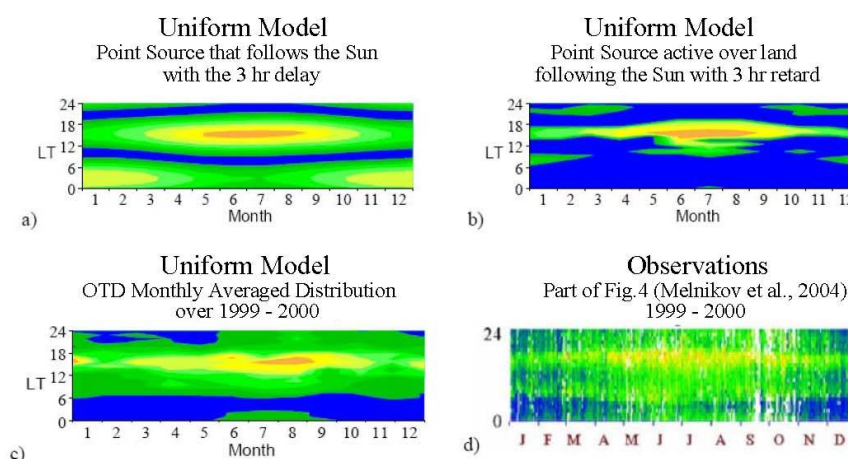


Figure 11 Comparison of the model and experimental data “terminator effect” at the Mitspe Ramon observatory

The map of Figure 11c was obtained in the framework of the source model based on the OTD (Optical Transient Detector) data averaged over the period of 1999 – 2002. As one may observe, patterns similar to observations are obtained in the model based on the realistic source models in the uniform cavity.

Similar model data were obtained by using ZHSR for the fields in the uniform cavity with the sources distributed in accordance to the OTD data for a given month of observations (see [Nickolaenko et al., ; 2006a, Nickolaenko et al. , 2006b] for details). The upper map in Figure 12 shows the yearly dynamics of the field source intensity derived from the OTD data. SR intensity is shown of the vertical electric field component in three maps were constructed for the European observatories Mitspe Ramon (31°N and 35°E), Nagycenk (48°N and 17°E), and Lehta (64°N and 34°E). The observatory name and the coordinates are printed at every map. The month is shown on the abscissa, and the UT in hr is shown on the ordinate. The range of UT variations was specially extended to 27 hr to clearly show the upper edge of the lens-like outline (the evening time). The color scale used for inking of all the maps is shown on the right. It is obvious that SR intensity reflects diurnal/annual changes in the global thunderstorm activity in the uniform Earth–ionosphere cavity. All maps have the similar shape: transition from low to higher intensity occurs in the European “morning hours” regardless latitude and longitude of the site. The transition from dark to bright in all maps is governed by the source activity, and it is present in dynamics of SR records.

Similarly to observations, data computed in the uniform mode also leave an impression that variation of the SR amplitude is linked to the motion of the day-night interface over the observatories. However, since the cavity was spherically uniform the pattern arises purely from the behavior of the field source. Moreover, if we compute the maps for other globally distributed sites, they will contain an abrupt variation in the SR intensity that occurs when the solar terminator passes over Europe [Pechony et al., 2007 Nickolaenko et al., 2006b].

A noticeable increase of the duration of thunderstorm activity in Figure 12 during the boreal summer is explained by the outline of continents in the Northern hemisphere. Indeed, with the increase of northern latitude the western shore of the North America moves westward by approximately 60° against the western edge of the South America. The Asian continent similarly expands to the east, though to the minor extent. This is why the world thunderstorms start earlier and end later in the summer months, so that the intense SR signal is recorded for a longer period at all observatories. Thus, seasonal changes of high lightning activity are similar to the day duration in

Europe: the increase of Asian thunderstorm activity starts in-phase with the sunrise in Europe while the decrease of the American activity occurs around the sunset in Europe.

An impact of the day-night interface on the SR oscillations was addressed in [Madden. and Thompson, 1965] and [Bliokh, 1980]. The results of analysis were summarized in the monographs [Nickolaenko and Hayakawa, 2002 ; Bliokh, 1980 ; Nickolaenko and Hayakawa, 2014] and in Ph. D works [Rabinowicz, 1988 ; Pechony, 2007]. The terminator effect in the SR band cannot be prominent because the pulsed wave front launched by a lightning stroke a few times passes through the day and the night hemispheres prior to its complete attenuation. The kind of “averaging” takes place as if the signal propagates in some effective uniform cavity. Depending on the smooth or the sharp terminator model, the day–night non-uniformity is able to cause amplitude modulations from $\pm 5\%$ (the smooth terminator) to 10% (the sharp step-like interface) (see [Nickolaenko and Hayakawa, 2002; Nickolaenko and Hayakawa, 2014; Rabinowicz, 1988 ; Pechony, 2007; Pechony et al ., 2007 ; Nickolaenko et al., 2006a; Nickolaenko et al., 2006b]). Some special experimental techniques should be elaborated for detecting the tiny variations caused by terminator in the natural radio noise having the 2-fold daily variations caused by the source motion and intensity.

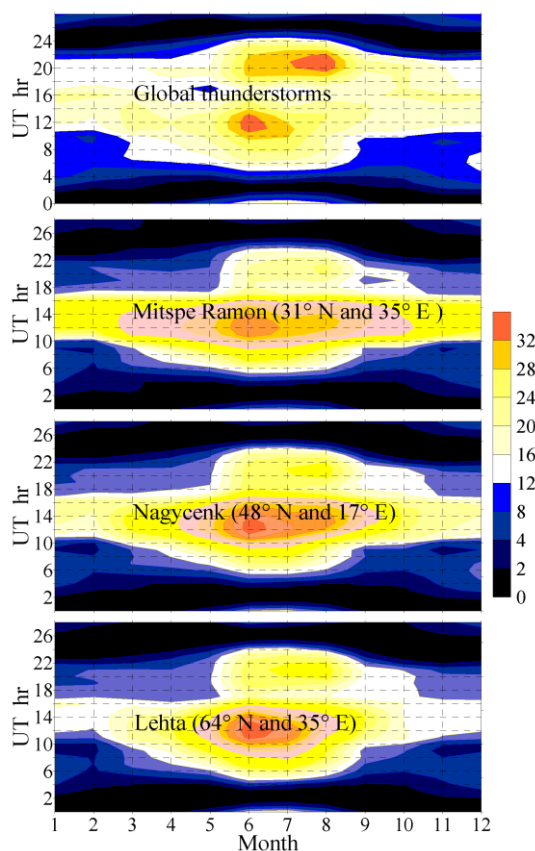


Figure 12: Model lens-like seasonal–diurnal patterns computed for a set of observatories in the uniform Earth–ionosphere cavity with the OTD data

4.2 Antarctic 10 years record

SR enables us to obtain characteristics of the lower ionosphere and dynamics of global thunderstorms by using the data recorded at a single or a few observatories. Here, we apply here the long-term SR record from the “Akademik Vernadsky” Ukrainian Antarctic station (65.25°S and 64.25°W) for demonstrating how the north-south seasonal drift of global thunderstorms might be evaluated. A complete description and all results deduced from these records might be found in [Sátori, 2003].

Two horizontal orthogonal components of magnetic fields are monitored by induction-coil magnetometers in the frequency band 0.1–300 Hz. Antennas are oriented along the geographic meridian (*SN* channel) and the parallel (*WE* channel). GPS synchronization was used. The experimental data are processed as follows. Daily records from *SN* and *WE* channels are subdivided onto 10-min intervals. The mean power and the cross spectra are obtained in these intervals with the frequency resolution 0.1 Hz. The daily records contain 144 spectra.

The spectra undistorted by interference are selected and monthly averaged diurnal data sets are derived each containing 144 spectra. These spectra are used to compute the monthly averaged intensities, peak frequencies (for the *SN* and *WE* channels separately), and polarization characteristics: the polarized intensity, ellipticity, position angle, degree of polarization. The modal intensity and frequency are defined by using the above-mentioned Rice definition. Figure 13 surveys the data corresponding to the first SR mode.

The upper frame in this figure depicts the long-term variation of the normalized intensity of the first SR mode observed in the horizontal magnetic field $I_1 = I_1^{WE} + I_1^{SN}$. The thick line in this panel is the running average in the time window of ± 3 points (months) width. The middle frame in Figure 13 presents variations of the first peak frequencies f_1^{WE} and f_1^{SN} observed in two orthogonal magnetic field components. The line with crosses corresponds to the H_{SN} field and the line with dots shows the H_{WE} component. To reduce rapid oscillations of peak frequencies, we also applied moving average of the same width. Dashed lines depict the peak frequencies averaged over the year. The lower frame illustrates the concurrent variations in the solar activity. The blue lines depict the intensity of solar radiation at the 10.7 cm wavelength (the left ordinate), and the red lines show the Wolf's number (the right ordinate). The dashed lines in the middle and lower frames present the annual average. One may observe that solar activity reached the minimum in 2009 and the SR parameters change in accordance with the solar cycle

We use the recorded peak frequencies f_1^{WE} and f_1^{SN} for evaluating the long-term variations of the effective SOD. The point source model was used for the world's thunderstorm activity. On the first stage, the power spectra of magnetic field were computed at the Antarctic station by the source positioned at a variable distance D . The model of the Earth-ionosphere cavity was used uniform along the angular coordinates, and the ionosphere was isotropic. The knee model [Mushtak and Williams, 2002] was applied for computing the ELF propagation constant, which was already described in the previous section.

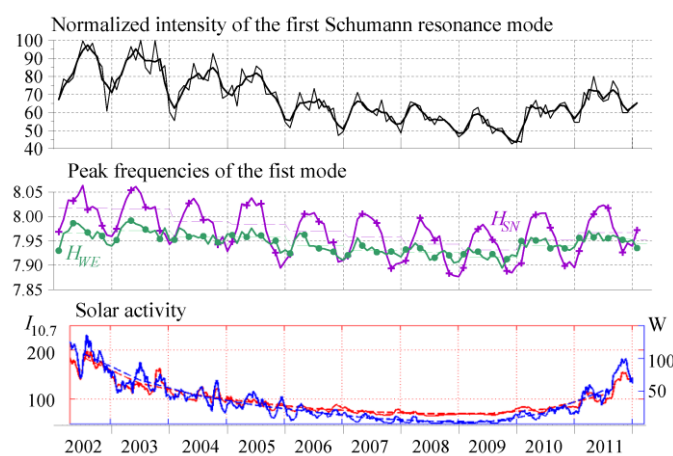


Figure 13 :Averaged intensities (top panel) and peak frequencies (middle panel) of first SR recorded at the Ukrainian Antarctic Station “Akademik Vernadsky” (65.25° S and 64.25° W) from March 2002 to February 2012 with respect to solar activity indices (bottom panel) - intensity of solar radiation at the 10.7 cm wavelength and the Wolf number

Results of computations are shown in Figure 14. The left frame shows the 2D intensity profile of vertical electric and horizontal magnetic field components over the frequency–distance plane. The abscissa shows the frequency in the vicinity of the first SR mode, and the ordinate depicts the SOD in Mm. The dark inking shows the intensity of oscillations. These maps are in fact the fragments of Figure 2 extended in the vicinity of the first SR mode. One may observe that the peak frequency of electric field is discontinuous around the 10 Mm distance and that of magnetic field monotonously increases with SOD. This allows us to evaluate the effective SOD from the observed value of resonant frequency.

We show the distance variations of the magnetic field peak frequency and intensity in Figure 14b. The horizontal axis depicts the SOD D in Mm. The first mode frequency is shown along the left ordinate by the black line with dots. The line 1 with stars fits the distance dependence $f_1(D)$ by a cubic polynomial. The normalized magnetic field intensity (the broken red line) is plotted along the right ordinate in percents. Magenta line 3 shows variations of the first associated Legendre polynomial $I_1(D) = [P_n^1(\cos\theta)]^2 \cdot 100\% = \sin(\pi D/20) \cdot 100\%$. The smooth curve 2 with diamonds refers to the distance variations of the magnetic field intensity $I_1(D)$ by the polynomial of the fourth order. The fitting polynomials were obtained by the least square technique and are expressed in the following way:

$$f_1(D) = a_0 + a_1 \cdot D + a_2 \cdot D^2 + a_3 \cdot D^3 \quad (35)$$

$$I_1(D) = b_0 + b_1 \cdot D + b_2 \cdot D^2 + b_3 \cdot D^3 + b_4 \cdot D^4 \quad (36)$$

Here D is the SOD in Mm, $a_0 = 6.71336$, $a_1 = 0.181732$, $a_2 = -0.008612582$, $a_3 = 0.0001477123$, and $b_0 = 115.548$, $b_1 = -30.40512$, $b_2 = 7.1121217$, $b_3 = -0.56481212$, $b_4 = 0.0133658$. By using Eq. (7), one can correlate the first peak frequencies of 7.7, 7.8, 7.9, and 8.0 Hz with the source distances of 8.3, 9.8, 12.2, and 16 Mm respectively.

When deducing variations of the effective source distance from the records of SR frequency, one must use the inverse dependence $D=D(f_1)$:

$$D(f_1) = d_0 + d_1 \cdot f_1 + d_2 \cdot f_1^2 + d_3 \cdot f_1^3 \quad (37)$$

where $d_0 = -15003.1$, $d_1 = 6033.82$, $d_2 = -809.608$, and $d_3 = 3.2566$. Annual and interannual variations of the effective distance from the source are shown in Figure 15. Here, abscissa depicts the months from January 2002 to June 2012, and the evaluated effective source distance of shown along the ordinate. The violet line with crosses was obtained from the f_1^{SN} frequency and the green line with dots corresponds to f_1^{WE} frequency. The dashed lines depict the annually averaged distances found from two orthogonal field components. These data are also listed in Table 2.

Variations of effective source distance were derived for the idealized point source model, and the observed frequency variations are attributed exclusively to the seasonal and inter-annual drift of global thunderstorms. In spite of such strong assumptions, we obtain a reasonable result. For instance, seasonal northward drift is clearly visible in Figure 15 during the boreal summer: the global thunderstorm centers move northward in the middle of a year, and we observe that the source

distance D from the Antarctic observer increases in both the field components. The range of annual drift is estimated as ~ 4 Mm from the SN field component (sensitive to African thunderstorms). Such a displacement reaching ± 2 Mm or even higher corresponds to $\pm 18^\circ$, which is quite reasonable. Variations derived from the WE component (American and Asian thunderstorms) are less pronounced: about 1.5 Mm or 13° .

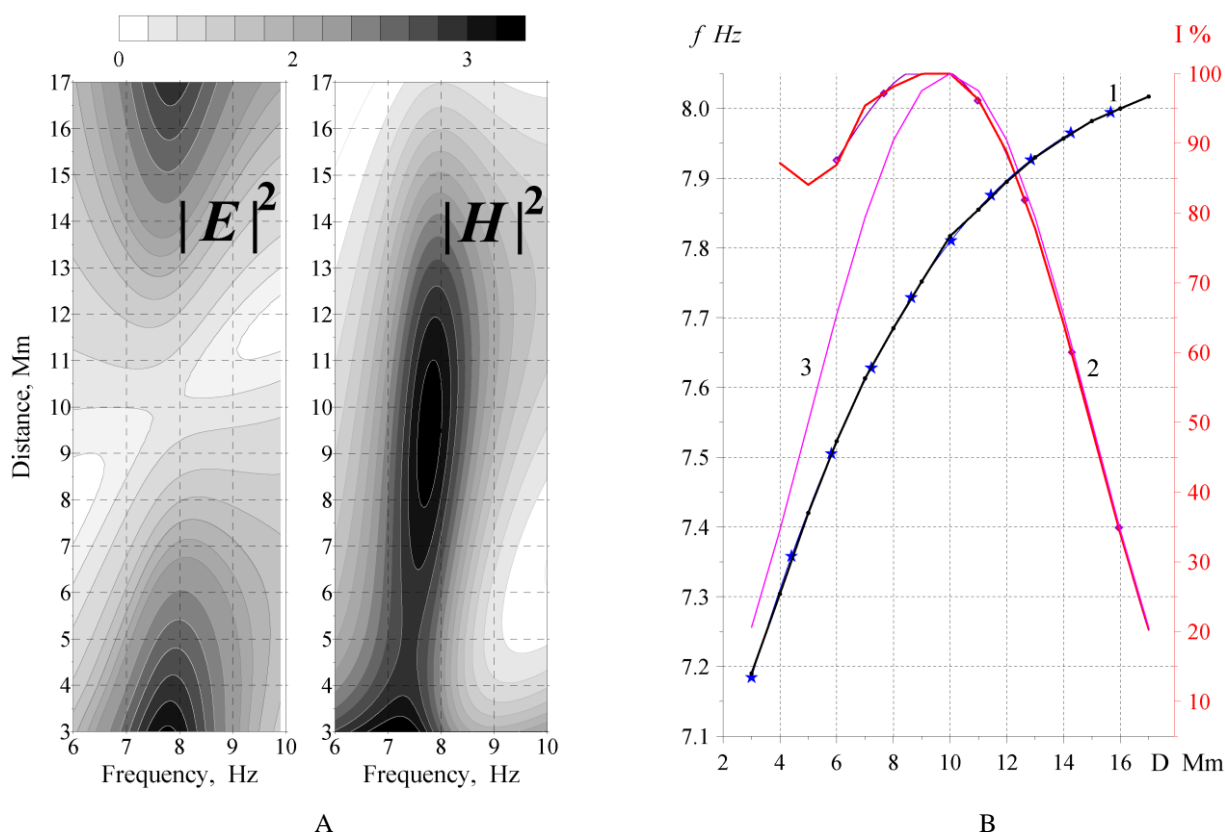


Figure 14 (a) Resonance intensity over the frequency–distance plane in the vicinity of the first SR mode; (b) distance dependence of the first mode frequency and intensity: curve 1 – the $I(D) = \sin(\pi D/20)$ dependence; curve 2 – peak frequency; curve 3 – intensity.

Plots in Figure 15 show the reasonable range annual variations and the inter-annual, which might be explained by alterations in the solar activity, but both estimates exceed the value of 10 Mm. The large median source distances deviate from the expected values. There might be the following causes of this discrepancy:

- (i) Different ways of evaluating the peak frequency. The values might deviate from those obtained by fitting the resonance peak in the observed spectra.
- (ii) Deviations might arise from an irrelevant ionospheric model that underestimates the peak frequency. Validity of such an assumption seems doubtful, since the knee model was specially developed for the most exact description of the experimental spectra, although recorded in the Northern hemisphere.
- (iii) Application of the point source model, which ignores the spatial distribution of global thunderstorms. The success of such a simple model is explained by closeness of the observed peak frequencies to the interval where the $f_1(D)$ function is a linear one. In case of distributed thunderstorms, the distance estimated corresponds to the centroid of zone covered by lightning strokes.

The qualitative and quantitative agreement exists among the data on the seasonal drift of global thunderstorms obtained with other ELF experiments (see e.g. [Sátori, 2003; Sátori et al., 2003 ; Sátori et al., 2005; Sátori et al., 2006 Sátori et al., 2009; Shvets et al., 2010; Shvets and Hayakawa, 2011; Hayakawa et al., 2011]). Still, further modeling and relevant calibrations are necessary to improve the accuracy of the source parameters evaluated by using SR records at different sites. Direct comparison with the concurrent compatible records in the Northern and Southern hemispheres is strongly desirable.

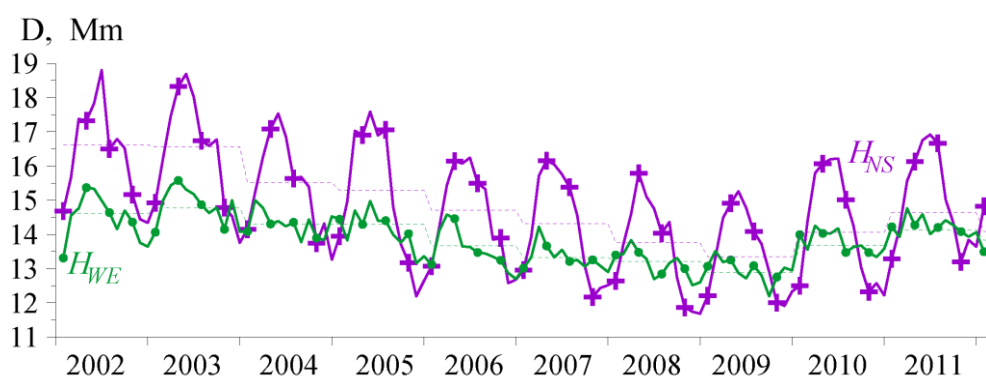


Figure 15 Annual and inter-annual variations of SOD deduced from the records at the Antarctic station

Table 2
 Annually averaged peak frequencies of the first SR mode and relevant source distances

Year	$\langle f_1 \rangle$ [Hz] in different field components		SOD, Mm	
	H_{WE}	H_{SN}	H_{WE}	H_{SN}
2002	8.016	7.966	16.62	14.6
2003	8.015	7.971	16.56	14.77
2004	7.999	7.958	15.52	14.3
2005	7.984	7.958	15.29	13.66
2006	7.969	7.940	14.7	57.43
2007	7.958	7.930	14.3	13.32
2008	7.943	7.927	13.76	13.2
2009	7.931	7.916	13.35	12.87
2010	7.951	7.941	14.05	13.67
2011	7.967	7.953	14.63	14.13

Antarctic long-term records were exploited in [Sátori, 2003] for evaluating feasible inter-annual temperature changes by using the following connection between the temperature anomaly of tropical land and the intensity of SR [Sekiguchi et al., 2006]:

$$\Delta T [^{\circ}\text{C}] = 0.0177 + 0.4845 \cdot \Delta I [\text{dB}] \quad (38)$$

SR intensity in Antarctica has decreased by ~ 3.2 dB at the first resonance mode during the time interval of 2003-2009 of reduced solar activity (see Figure. 13). Such a reduction results in the 1.6°C decrease of the tropical land temperature. This trend has no link to the global warming or cooling. This is a regular change in the soil temperature of the tropics related to the 11-year cycle of the solar activity, which was not yet mentioned in the literature. The alteration evaluated is related to the ground temperature, while 80% of tropics are covered by the ocean having the stable temperature, so that the globally averaged estimate is reduced to $\sim 0.3^{\circ}\text{C}$. This value is quite detectable, and it is desirable to compare the available temperature and the SR data.

4.3 Disturbances associated with space weather

Solar proton events (SPEs)

Monitoring of SR provides interesting results connected with the abrupt changes in the Earth environment, in the space weather. The effects are observed as quick abrupt changes in the records superimposed on the regular diurnal pattern. These transient variations are usually caused by modifications of the global ionosphere. In this sense, monitoring of peak frequencies has the obvious advantage: an abrupt alteration in the peak frequency might be caused either by changes in the

ionosphere or by the sudden displacement of global thunderstorms. The second modification is doubtful.

Ionospheric disturbances at different altitudes may provide the opposite reaction of SR frequency, which was noted in the pioneering study [Madden and Thompson, 1965] and multiply confirmed afterwards (see e.g. [Yang and Pasko, 2005 ; Zhou, et al ., 2016] and references therein). Two types of disturbances exist in the Earth–Ionosphere cavity, and both of them have the cylindrical symmetry. One of them is the Sudden Ionospheric Disturbance (SID) and the other is the Polar Cap absorption (PCA). An SID event is the abrupt enhancements in the dayside lower ionosphere caused by the solar X - flares. The plasma modifications belong to the day–night type and therefore they produce only minor changes in the peak frequencies hardly visible in the records.

Disturbances of the PCA type are caused by the charged particles arriving at the Earth from the Sun. These are deflected to the poles by the geomagnetic field and precipitate in the polar and sub-polar regions. The polar ionospheric D region goes down at both the poles, and a PCA is observed as a radio black-out on the sub-polar propagation paths. The PCA provides a global ionospheric modification that is symmetric in respect to the geomagnetic equator. This feature enhances its impact on the SR frequencies.

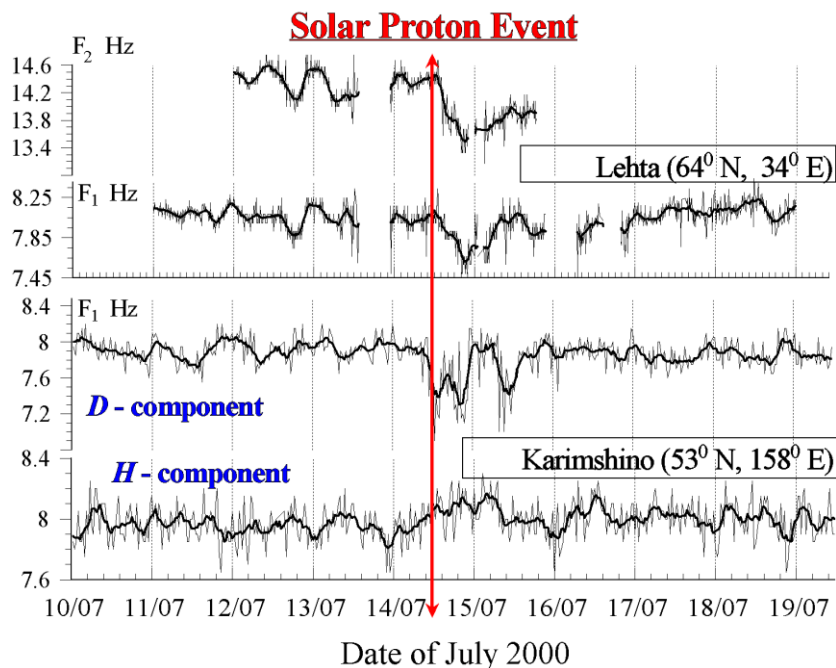


Figure 16: Abrupt changes in the peak frequencies caused by the Bastille Day SPE

A solar flare starts with radiation of X-rays and gamma quanta, which overcome the 150 million km distance in ~500 s or 8 minutes. The electromagnetic radiation is followed by the relativistic

solar protons (SPE) or electrons (SEE (solar electron event)) which arrive with the delay of a second. The proton energy may exceed the 10–100 MeV level, and that of the electrons exceeds a few MeV. Abrupt initial changes are followed by modifications in the solar wind flux causing the geomagnetic storms starting in a couple of days after solar flare initiation. Depending on the ionosphere modification height, the particular PCA and SID events may appear in the SR records in different ways, though both of them are caused by an increase in the lower ionosphere conductivity driven by the solar activity. We describe the impact of SPE on SR record first and afterwards describe the special processing technique that reveals the reaction of SR frequencies to the solar X-ray flares.

Figure 16 illustrates the effect of a powerful SPE that occurred around the UT noon on July 14, 2000. The event is regarded in the literature as Bastille Day SPE. The abscissa shows the time in days of July, and the observed SR peak frequencies are shown on the ordinates.

Two upper panels in Figure 15 show an abrupt decrease of the first and the second SR mode frequencies recorded at Lehta observatory (64°N and 34°E). The vertical red arrow denotes the SPE onset. One may note the rapid decrease of the peak frequencies of 0.4 Hz at the first, and 0.8 Hz at the second modes. Two lower frames of Figure 16 show the records from the Karimshino observatory (53°N and 158°E). Changes are depicted of the peak frequencies of the horizontal magnetic field components H and D . The H -component lies in the plane of magnetic meridian, so that it is close to the geographic H_{SN} , and D -component is perpendicular to this plane, it is close to the H_{EW} component. Each plot is shown by thin and thick lines. Thin lines show the original data, which indicate the power spectra accumulated every 10 min. Thick lines are the moving average (1 hr window) of quickly varying raw data.

Development of a classical PCA is clearly seen in Figure 16. The simultaneous global decrease of SR frequencies is apparent, and changes start at arrival of solar protons to the Earth. The simultaneous abrupt decrease in different field components recorded at widely separated field sites indicates the global modification of lower ionosphere [Roldugin et al., 1999; Roldugin et al., 2001; Roldugin et al., 2003; Nickolaenko et al., 2008].

A close examination of Figure 16 reveals a short increase of peak frequency at the onset of the SPE [Roldugin et al., 1999; Roldugin et al., 2001; Roldugin et al., 2003; Nickolaenko et al., 2008]. It lasts for 5–10 min followed by a reduction during 1 hr or longer. Such a development indicates that initially the ionospheric conductivity grew around the 100 km altitude causing an increase in the peak frequency [Bliokh, 1980]. Additional ionization penetrates to lower altitudes with time, and the conductivity finally increases around the electric characteristic height causing the reduction in the

peak frequency. Plasma modification covers the distance from 100 to 60 km in about 10 minutes, hence, its vertical velocity is 4 km/min or ~70 m/s. Such a slow expansion indicates the diffusion mechanism rather than the particle precipitation.

A comparison of record and the model data [Bliokh, 1980; Nickolaenko and Hayakawa, 2014; Nickolaenko et al., 2008] allowed us to conclude that the Bastille Day SPE has caused approximately 50% modification of the ionosphere above the poles. Since the observed peak frequency depends on the ratio Z/kh , where Z is the effective surface impedance of the lower ionosphere, h is its effective height, and k is the free space wavenumber, the observed modifications could be attributed either to the 50% increase of effective surface impedance of the polar ionosphere or to the 50% reduction of ionospheric effective height over the poles, or to the both of them simultaneously being 25% each.

4.4 Solar X-ray flares. Novel technique

The effect of SPEs on SR records is noticeable; therefore it is commonly addressed in many publications. Impact of the X-ray flares is less pronounced, and a problem exists of its identification at the background of stochastic variations relevant to the random nature of ELF field sources [Shvets et al., 2016a ; Shvets et al., 2016b]. No convincing data were presented in the literature demonstrating the influence of a solar X-ray flare on the SR frequencies (e.g. [Sátori et al., 2016]). We introduce below a special technique that reveals a simultaneous sharp variation in all resonance mode frequencies, which are usually hidden in the customary records. The technique implies the weighted average frequency of SR, which is formally based on the mutual relation $f_n = 5.7 [n(n+1)]^{1/2}$ of the modal frequencies mentioned when discussing Figure 2.

Impact of a X-flare on the SR pattern is readily explained physically. The hard solar electromagnetic radiation sharply increases the plasma density on the dayside of the globe, so that the boundary of the lower ionosphere goes down here. The night ionosphere is hidden in the shade, and it remains undisturbed. Reaction of ELF waves to X-ray flare is caused by the reduction of the globally averaged (effective) ionospheric height. Modeling shows (see the next-subsection) that such a reduction causes a simultaneous drop of all eigen-values, and the effect is observed as a modification of the whole SR pattern.

We present the SR records at the Karymshino observatory (52.9°N and 158.25°E) where three orthogonal components of the magnetic field H , D , Z are recorded with the sampling frequency of 100 Hz. The elementary power spectra of these fields were computed by the Fourier-transform of the fragments 3,000 points long. The 9-point moving average was used, and the results were averaged

over the 5-minute intervals. The resonance parameters were obtained by fitting these spectra by a sum of four Lorentzian curves (the first four SR modes).

Figure 17 shows data recorded during the X2.1 solar flare on March 11, 2015. The abscissa depicts the universal time in hours. The thin fractured curves show the modal frequencies with the 5 min time step. Here, the regular daily variations of modal frequencies were found by averaging records over 5 successive days (± 2 days relative the date of the event) and these were subtracted from the observed daily pattern. To facilitate comparison, we separated individual modal plots vertically by 0.5 Hz. The dotted line depicts the flux density of X-rays (I) shown on the logarithmic scale on the right ordinate. The X-ray data were obtained by the GOES-15 satellite.

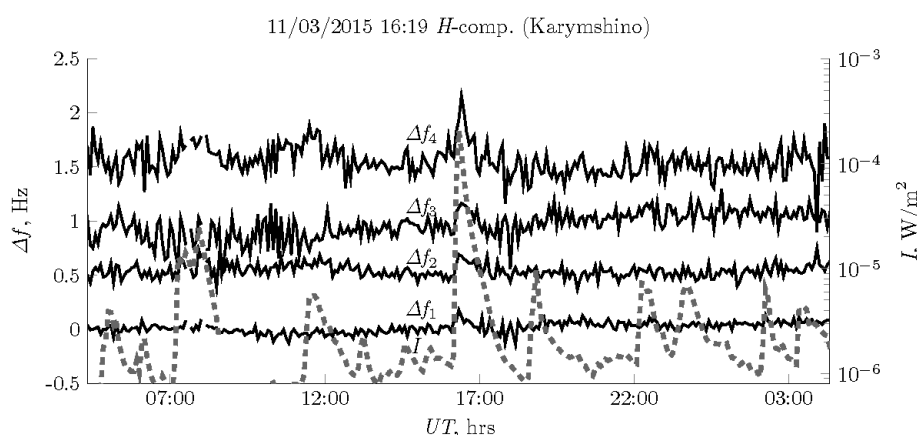


Figure17:Temporal variations of four modal frequencies during the solar X-ray flare on March 11, 2015 with the mean daily runs subtracted. Variations of the X-ray flux power are shown by a dashed curve.

An optimist would note an abrupt increase in all peak frequencies at the onset of the flare. However, the reciprocity to the solar flare is hardly convincing owing to many false abrupt variations that mask the only one excursion relevant to the flare. Thus, one cannot register credible reaction of SR frequencies to the X-flare.

Simultaneously, Figure 17 demonstrates that random variations in individual peak frequencies deviate from each other. In contrast, the reaction of peak frequencies to the abrupt change of global ionosphere must be similar and simultaneous at all resonance modes. We will reduce the random fluctuations and reveal the coherent reaction by special averaging of peak frequencies. For this purpose, we introduce the weighted resonance frequencies $f^{(n)}=f_{PEAK} \cdot [n(n+1)/2]^{-1/2}$, which are approximately equal to 5.7 Hz (see Figure 2). Averaging of the weighted frequencies over a few

modes must reduce the fluctuations. Simultaneously, the weighted averaged frequencies remain sensitive to the global properties of the lower ionosphere.

Figure 18 shows excursions of weighted average frequency during the same X2.1 event of March 11, 2015. Plots in this figure demonstrate now a close coincidence of the main increase in the X-ray flux and the reaction in weighted average frequencies. The similarity becomes apparent owing to a substantial decrease in frequency fluctuations. One can even observe a detailed agreement of two records: the reaction became visible on some secondary increases in the X-ray event.

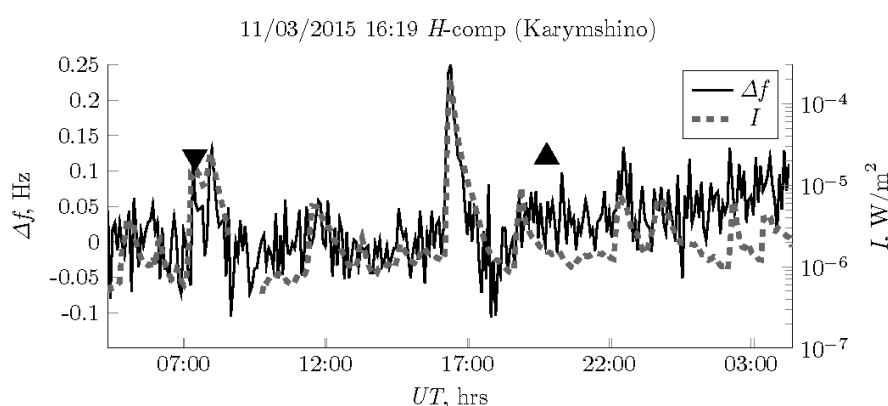


Figure 18: Temporal variation of weighted average frequency during the solar flare of March 11, 2015

To demonstrate the reaction of SR modes to the global modification of lower ionosphere, we place the black wedge and the triangle in the plot. The first one indicates the moment of sunset at the observatory, and the second one corresponds to the local sunrise. Clearly, reaction of SR frequencies was recorded in the ambient night conditions while the X-rays modified the dayside ionosphere. Such a reaction would be impossible at VLF. Thus, we conclude that an application of weighted average frequencies of SR reveals the reaction to the SID events.

4.4 *Powerful gamma-ray flare and SR background spectrum*

We briefly discuss the impact of the powerful gamma ray flare from *SGR 1806-20* on SR. The flare occurred around 21 hr 30 min and 26.5 s UT on December 27, 2004. The hard X- and gamma-rays arrived at the dayside of the Earth covering almost the whole hemisphere. Radiation came from a soft gamma repeater (SGR) neutron star *SGR 1900+14* positioned 30–40 thousand light years away. The peak flux exceeded the most intense solar flares by approximately 5 orders of magnitude, and it was 100 times greater than the *SGR 1900 + 14* gamma flare of 1998. The ionospheric disturbance was centered above the Pacific Ocean, at the geographic coordinates, 146.2°W and 20.4°S, which

was only 450 km away from the center of the dayside hemisphere, and it covered the whole hemisphere. The gamma flare lowered the dayside ionosphere by ~20 km, and this abrupt reduction lasted less than 0.02 s. The temporal change of the height was fitted by the function: $dH = -19 (9.6441 t)^{-0.1501}$ (see [Tanaka et al., 2011; Nickolaenko, et al., 2012]) where t is the time since the gamma ray arrival. The ionospheric height was varying with a step of 10 s in the model computations. Information in more detail and complete reference might be found in [Nickolaenko and Hayakawa, 2014].

We describe in what follows the successful detection of changes in the SR spectra during the gamma flare on December 27, 2004. The record was performed at the Moshiri observatory. Experimental material is compared with the model computations, and it was crucial to have the model results prior to inspecting the data: modeling has shown what we should look for in the record.

The heuristic knee ionosphere model was used [Mushtak and Williams, 2002]. To incorporate the ionosphere day–night non-uniformity into modeling, the partially uniform knee (PUK) model was used [Pechony and Price, 2004]. The computations suggested that the knee altitude was reduced by gamma rays in accordance with the above formula. Thus, the electric height of the ionosphere goes down, while the magnetic height remains undisturbed. Such a modification of the sole electric height is discussed in [Inan et al., 2007] based on the VLF monitoring at Antarctica “Palmer” station. The 20 km ionosphere reduction over the dayside of the globe results in the average height decrease of 10 km.

By using 2DTE modeling, the results were compared of the 10 km reduction in the uniform cavity and the 20 km reduction in the cavity with the day–night non-uniformity [Pechony and Price, 2004]. These two ionosphere models incorporated the globally uniform thunderstorm distribution and the lightning distribution following from the OTD data. A comparison of the model results showed that the day–night non-uniformity provides a secondary effect in the general modification by the galactic gamma rays in comparison with the reduction of globally averaged ionosphere.

Figure 19 shows the impact of gamma rays computed in the models the non-uniform Earth–ionosphere cavity (upper plot) and of the uniform cavity (lower plot). Individual spectra were computed for the vertical electric field by using the 2DTE with the PUK day–night model [Pechony and Price, 2004 25]. The OTD source distribution was used in both cases. Plots of Figure 19 have the same feature: in all models, the dynamic spectra contain the characteristic abrupt drop in the resonance pattern, which is coincident with the arrival of gamma rays.

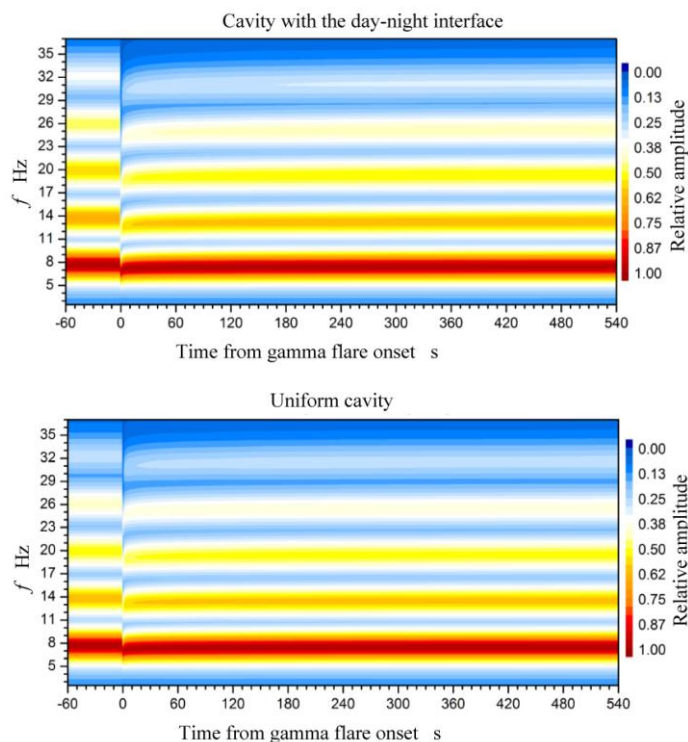


Figure 19: Changes in the SR sonograms at the moment of gamma flare computed for the Earth–ionosphere cavity with the day–night interface (upper frame) and the uniform resonator (lower frame)

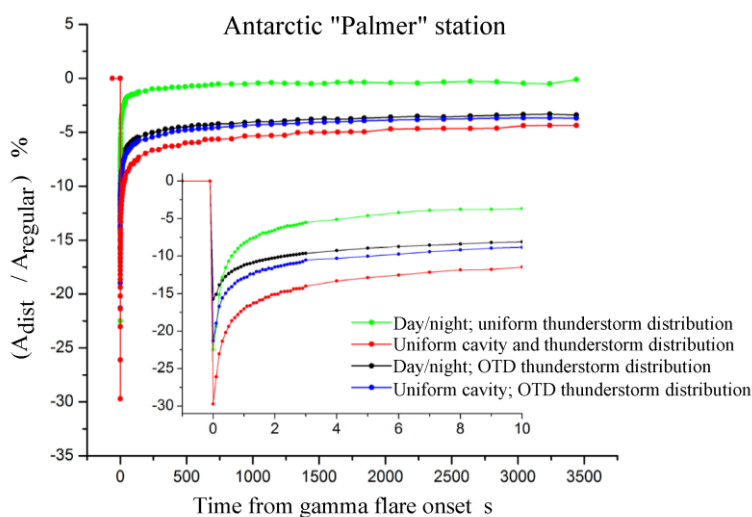


Figure 20: Sharp amplitude variations during gamma flare computed for the uniform and non-uniform cavity models with the uniform and OTD spatial distributions of global thunderstorms

Abrupt amplitude variations are given in Figure 20 obtained with the 2DTE for the amplitude of the first SR mode. We plot here modulations for the uniform and the non-uniform Earth–ionosphere cavities. The observer is placed at the “Palmer” Antarctic station, where the impact of gamma flare

on the lower ionosphere was detected in VLF transmissions [Inan et al., 2007]. Again, both uniform and the OTD spatial distributions of lightning strokes were used combined with the uniform and day-night models of the Earth–ionosphere cavity.

The inset in Figure 20 shows the amplitude reduction with the higher temporal resolution, $t \in [0, 10 \text{ s}]$ where $t = 0$ is the gamma flare onset. One may conclude by comparing the black line (OTD lightning distribution in the non-uniform cavity) with the blue one (OTD distribution in the uniform cavity) that impact of the ionosphere day-night asymmetry plays the secondary role. The general behavior remains the same: an abrupt reduction reaching 30%, which is followed by gradual recovery. The highest deviation is pertinent to the uniform distribution of lightning strokes. Thus, computations predict essentially the same modification for all models: gamma rays abruptly and simultaneously reduce all resonance parameters at all resonance modes. Hence, the effect must look as a discontinuity in the observed SR sonograms around the arrival time of gamma flare.

We use the ELF monitoring at Moshiri. Waveforms of vertical electric, the west-east (WE), and the south-north (SN) horizontal magnetic field components are recorded here with the sampling frequency of 4 kHz [Tanaka et al., 2011]. A fragment was chosen of the ELF record in the vicinity of the gamma flare and the dynamic spectra of H_{SN} and H_{WE} components were found as seen in Figure 21. Time is shown on the abscissa in seconds, and the zero time corresponds to the moment of gamma ray arrival. The ordinate depicts the frequency with the step of 2 Hz. We present two survey sonograms in this figure.

Apparently, the data processing must satisfy two contradicting conditions. The model computations predict the abrupt shift of resonance pattern by about -1 Hz , which lasts less than 10 seconds. To detect such a shift, the frequency resolution must be 0.1 Hz at least, so that segments of 10 s duration should be used in the FFT procedure. This is rather a long duration, because the ionospheric disturbance exists for less than 10 s. To obtain the necessary time and frequency resolution, we had used the time segments 10 s long, but the individual spectrograms were obtained with the 1 s step. In particular for the moment $t = 0$, we process the segment ranging from -5 to $+5 \text{ s}$; for the time $t = 1$, we use the segment from -4 to $+6 \text{ s}$, etc. These “central” times are shown on the abscissa of Figure 21.

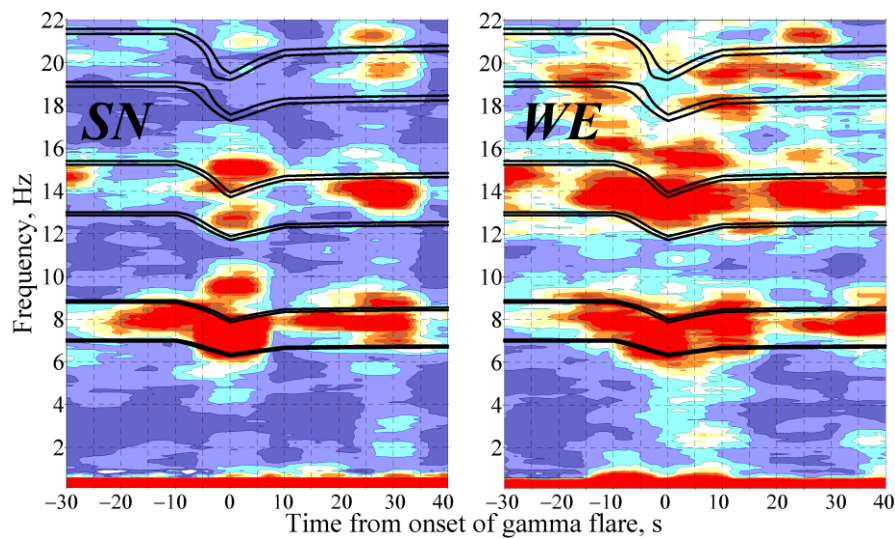


Figure 21: Comparison of observed data with the model dynamic spectra in the vicinity of gamma flare

The sonogram in Figure 21 visibly demonstrates the above-mentioned instability of experimental SR spectra associated with the stochastic nature of lightning strokes. The commonly known smooth resonance lines appear after averaging of elementary spectra acquired in the 5–10 min interval (from 30 to 60 elementary spectra). Therefore, one hardly can expect a regular resonance pattern in Figure 21: individual spectra are spontaneous in both the field components and this is the major obstacle in revealing the impact of gamma rays.

To disclose the global ionosphere modification, we combine in Figure 21, the experimental sonograms with the expected (model) modification shown by the thick black lines corresponding to the constant levels in the model sonogram of Figure 19. The sonogram covers the time interval ± 30 s around the gamma flare, and one may observe the similarity of expected and observed modulations in both the panels of Figure 21. Time of sudden reduction in the SR record fits the gamma ray arrival. Even the tendency toward the recovery might be perceived in Figure 21.

In contrast to the SID from solar X-ray flares, the ionosphere modification by the galactic gamma rays was much more intense, but of short duration. This swiftness is a serious obstacle in the experiment. Only direct comparison of computational and experimental sonograms revealed the fast simultaneous modification in the SR pattern caused by the powerful gamma ray flare of December 27, 2004. We can argue that conventional signal processing will miss the modulation. A special FFT procedure was necessary combining the 1 s time step with the 10 s segments.

Storms in the geospace result in different types of global ionosphere modifications. When a disturbance is driven by the hard electromagnetic radiation, its effect enhances the day-night non-

uniformity of the ionosphere (SID). Modification concentrates at the poles in both hemispheres when ionization is produced by the corpuscular radiation deflected by the geomagnetic field (PCA). Of course, this is a simplified picture, e.g., we do not mention the Earth's magnetosphere etc.. The symmetric polar disturbances are more efficient for the SR parameters than the asymmetric day-night modifications [Galejs, 1972; Bliokh et al., 1980; Nickolaenko and Hayakawa, 2014]. This is why the SPEs are easily seen in the SR records, while the solar X-flares demand a special processing. An event of the giant gamma flare on December 27, 2004 has caused the strong, but very short modification that was barely detected in the spectra of global electromagnetic resonance.

Inverse problem: the rigorous approach

SR data are usually collected for their further application in environmental studies, i.e., in solving the inverse electromagnetic problems. One can mention two kinds of these problems: those devoted to the global thunderstorms and those directed to studies of lower ionosphere. We briefly illustrate the first class of application.

The exhausting search is applied in the solutions aiming at the properties of lower ionosphere. For example, we found the simultaneous modification of resonance frequencies by the solar X-flare. The relevant ionosphere modification might be found in the following way. One picks a conductivity profile and computes the set of SR spectra for realistic global distributions of thunderstorms during the event. In these computations, a single model parameter is modified, and its selection depends on some additional information or consideration. The set of SR spectra computed for the same source distribution and the varying profile is compared with observations, so that a particular parameter might be found by fitting the experimental data in the best way (e.g. [Nickolaenko and Hayakawa, 2014]).

The exhausting search is relatively safe, but it is a time consuming approach. We briefly describe here the rigorous formulation and solution of inverse SR problem aiming at the global distribution of thunderstorms. We must remark that only an "effective" distribution might be found from the SR data. Indeed, the basic resonance frequency is equal to 8 Hz while the pulse rate of the global lightning is 50–100 events/s. One cannot resolve these pulses in a record and cannot formulate the problem of electromagnetic location of ordinary lightning strokes.

The formal solution of the problem implies the Tikhonov regularization procedure to a linear system of algebraic equations. One can present the links of the power spectra of the field components in the form matrix relation:

$$\mathbf{b} = \mathbf{A} \cdot \mathbf{L} \tag{39}$$

Here \mathbf{b} denotes the vector of measured power spectra, and \mathbf{L} is the sought vector of the stroke rate at different distances from the observer. The elements of \mathbf{A} matrix contain the model spectra in the particular Earth–ionosphere cavity that were computed for the set of distances from the vertical electric dipole source as seen in Figure 22.

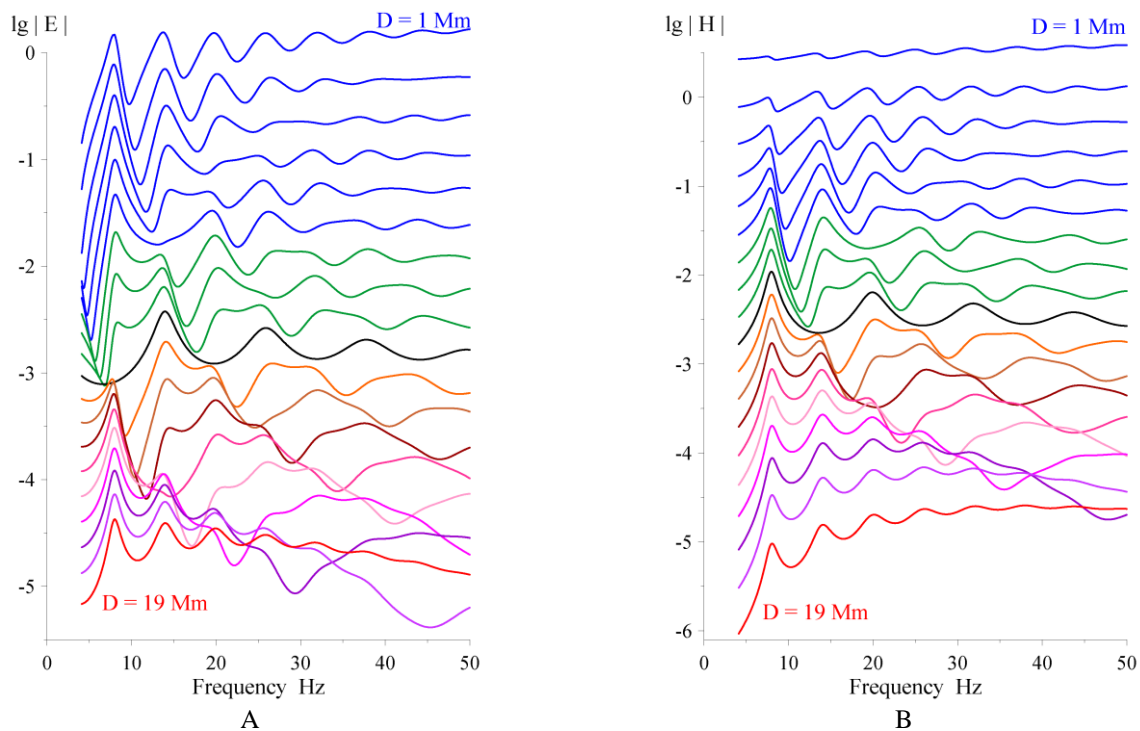


Figure 22: Amplitude spectra of vertical electric and horizontal magnetic field components for the SOD D ranging from 1 to 19 Mm. To separate plots, we shifted them vertically by $-0.25 D$, so that the top curves correspond to $D = 1$ Mm, and the bottom ones, to $D = 19$ Mm.

The SOD D ranges in Figure 25 from 1 Mm to 19 Mm varying with a 1 Mm step. Horizontal axes show the frequency in Hz, and the vertical axes depict the spectral amplitude on logarithmic scale. To separate different plots, we move them vertically by $-0.25 \cdot D$. The stroke current moment was $|M_C(\omega)| = 10^8 \text{ A m (Hz)}^{1/2}$ and the electric and magnetic spectral densities were measured in mV/m and $\mu\text{A/m}$ correspondingly. The standard frequency dependence $\nu(f)$ was used specified by Eqs. (13–16). One may observe that the regular succession of SR peaks is modulated by interference of the direct and antipodal waves. This interference was responsible for the deep extended canyons in the 2D maps of Figure 3. This feature is used to find the distance to the stroke that caused the Q-burst: every distance has a unique spectral outline.

The system (39) is resolved by the minimization of the squared deviations of the following functional:

$$F(\mathbf{x}, \rho_R) = \|\mathbf{A}\mathbf{L} - \mathbf{b}\|^2 + \rho_R \|\mathbf{L}\|^2, \quad \mathbf{L} \geq 0, \quad (40)$$

where α_R is the regularization parameter [Shvets et al., 2010; Shvets et al., 2011; Hayakawa et al., 2014].

After finding vectors \mathbf{L} (the stroke distribution along the distance from the observatory) by using the data at a few observatories, one can compile a map of the global distribution of field sources corresponding to the SR record. We illustrate the major stages of solution in Figure 23.

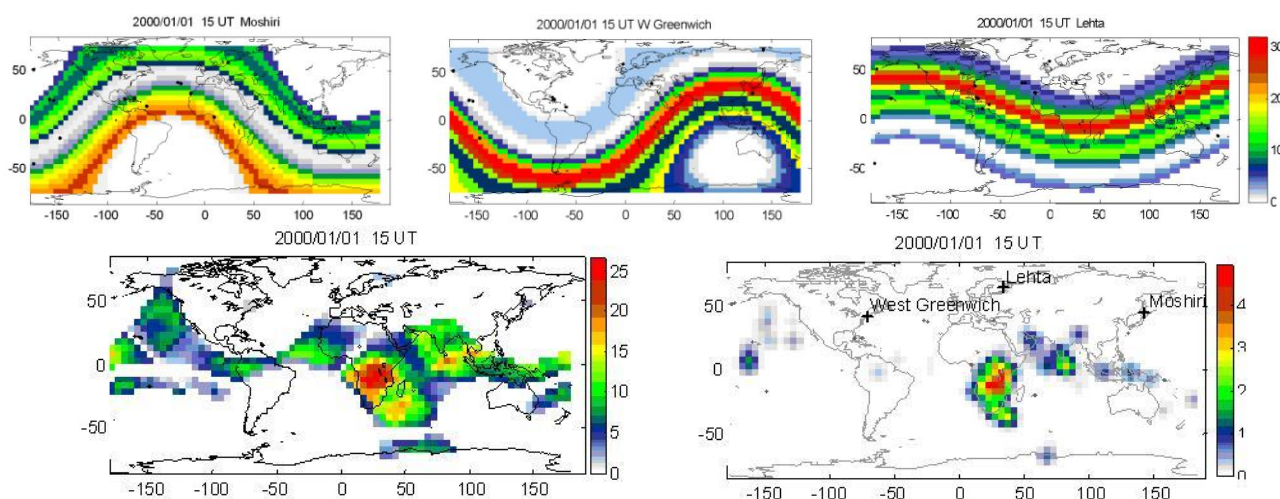


Figure 23: Major stages of solution of inverse problem based on simultaneous records at Moshiri, West Greenwich, and Lehta that at UT=15 hr on January 1, 2000

Three global maps in the upper part of Figure 23 depict the lightning rate (events per second) derived from the SR background spectra recorded simultaneously at Moshiri, West Greenwich, and Lehta at 15 hr UT on Jan. 1, 2000. The rates are shown as the strips of equal distances from the observatories. In the rectangular projection of the globe, the line of equal distance is a sinusoid, so that distance distributions are seen as concentric curved color bands. The color scale relevant to the maps is shown on the right. The distance profiles for every observatory allow constructing the equivalent spatial distribution of lightning strokes over the globe. The simplest way to do this task is to compute the geometric average, which is shown in the left lower frame of Figure 23. The map indicates that global thunderstorms are concentrated at Africa, which is quite natural for the 15 hr UT time moment. The higher activity is also apparent around the Ceylon Island and to the south of

Madagascar.

A more rigorous approach implies the tomographic reconstruction based on the set of spatial distributions [Shvets et al ., 2010; Shvets et al ., 2011; Hayakawa et al ., 2014]. Results of tomographic reconstruction are shown in the right lower panel of Fig. 23. Here, the crosses mark the observatories, and the color inking corresponds to the lightning rate. As a whole, the geometric averaging and the tomographic reconstruction provide similar geophysical results. However, the rigorous procedure performs a substantial “cleaning” of the global thunderstorm distribution: it removes insignificant and probably false objects while the most pronounced and compact areas are preserved.

Apparently, the average annual distribution of lightning is most interesting, and we show it in Figure 24 [Shvets et al., 2010; Shvets and Hayakawa, 2011; Hayakawa et al., 2011]. This map was constructed similarly from the SR monitoring at the same three stations shown in the figure by crosses. SR data cover the interval of August 1999 through May 2000. Here, the spatial distribution of lightning rate was obtained by the tomographic reconstruction with an account of the azimuthal data of the wave arrival (records of the orthogonal magnetic field components were used). The map of the global distribution of the lightning flashes is shown for comparison in the lower part of Fig. 24, which was observed by the OTD spacecraft [Christian et al., 2003]. One may observe the unmistakable similarity of optical orbital observations and the ground-based tomographic reconstruction of global lightning activity. Actually, there are definite departures in the maps, which indicate the necessity of further experiments and improvements.

The rigorously posed inverse problem of the SR is resolved in two stages. First, the power spectra of magnetic and electric fields (Figure 22) are inversed giving the distance distributions of thunderstorms relative to each observatory (Figure 23). Then, the distance profiles are applied as tomographic projections in the recovery of the spatial distribution of sources (Figure 24). Accuracy of solution increases when the wave arrival information is accounted for. Reconstruction based on the records from Lehta (Russia), Moshiri (Japan), and West Greenwich (USA) showed the diurnal/seasonal dynamics of the global distribution of lightning strokes, which fairly agree with the data of meteorology and optical observations from space [Shvets and Hayakawa, 2011; Hayakawa et al., 2011; Roldugin et al., 1999].

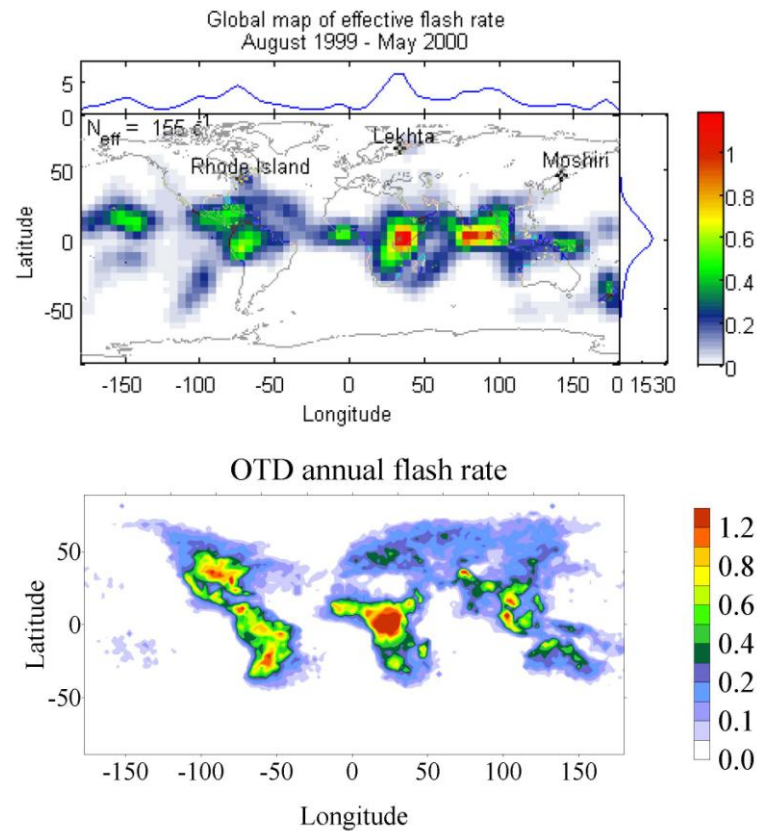


Figure 24: The yearly averaged (August 1999 – May 2000) global lightning distributions obtained from the SR records and observed by OTD

The rigorously posed inverse problem of the SR is resolved in two stages. First, the power spectra of magnetic and electric fields (Figure 22) are inverted giving the distance distributions of thunderstorms relative to each observatory (Figure 23). Then, the distance profiles are applied as tomographic projections in the recovery of the spatial distribution of sources (Figure 24). Accuracy of solution increases when the wave arrival information is accounted for. Reconstruction based on the records from Lehta (Russia), Moshiri (Japan), and West Greenwich (USA) showed the diurnal/seasonal dynamics of the global distribution of lightning strokes, which fairly agree with the data of meteorology and optical observations from space [Shvets and Hayakawa, 2011; Hayakawa et al., 2011; Roldugin et al., 1999].

3.2. Non-stationary ELF waves (Q-bursts)

The term of Q-bursts was introduced by Ogawa’s group in 1966 [Ogawa et al., 1966], which refers to discrete natural radio pulses that have the duration of 0.3 – 1 s and are detected all over the globe.

The Q-bursts or ELF transients arrive from exclusively powerful lightning discharges and their amplitude may exceed that of regular SR background by a factor of ten. These signals present a rare possibility of study on the wave arriving from individual source, i.e., to derive the source position and the radiation spectrum. The technique of locating the causative source was suggested in [Jones, 1970b; Burke and Jones, 1995; Burke and Jones, 1996 78–80], and it was developed and applied in different studies, especially in investigations of transient luminous events (TLEs) including red sprites.

We already demonstrated equations, the model spectra and the model pulsed waveforms computed for different SODs. Here, we compare the model waveform computed directly in the time domain by using Eq. (11) with the most advanced observations recorded in the extraordinary wide frequency band. The experimental data were published in [Ogawa and Komatsu, 2007]. These records practically do not contain the 50 Hz power supply interference, so that notch filtering was unnecessary. The waveforms were recorded by the receiver of unusual bandwidth of 1 Hz–11 kHz, and the sampling frequency was 22 kHz. The vertical electric field component was recorded at Kochi, Japan (33.3° N, 133.4° E) during the years of 2003–2005. Individual pulses were selected visually from the records performed in the fine weather conditions with the help of classical ball antenna.

A comparison of model and observational data is made in Figure 25. The source distance was evaluated as $D = 16.5$ Mm (see [Nickolaenko et al., 2008] for details). The waveform is shown by a red curve with dots computed by using Eq. (11) for the linear frequency dependence of propagation constant. The black line depicts the experimental waveform. One can note the remnants of the power supply 50 Hz interference in the record. The fine structure is apparent in the record formed by the spikes of individual lightning strokes, some of these having high amplitude. All these interesting and convincing features are much smaller in comparison with the major excursion of the Q-burst.

The similarity of experimental and model is apparent in Figure 25. One can conclude that the SOD was evaluated correctly, because the direct and the antipodal waves are well resolved and coincident in the initial part of the record. The secondary round-the-world pulses are also clear and coincident. The initial outline gave the name for the transient: the Q-burst of W-type. Owing to the wave dispersion and attenuation of high frequencies, two pulses merge in the round-the-world wave. It is remarkable that positions are coincident of the model and observed sub-pulses in the “head”, and the same is valid for the observed and model round-the-world pulses.

Similarity of the model and observational waveforms validates the application of:

- (i) The uniform model of the Earth–ionosphere cavity bounded by an isotropic ionosphere;
- (ii) The propagation constant linearly varying with frequency;
- (iii) The formal time domain solution for the ELF transient.

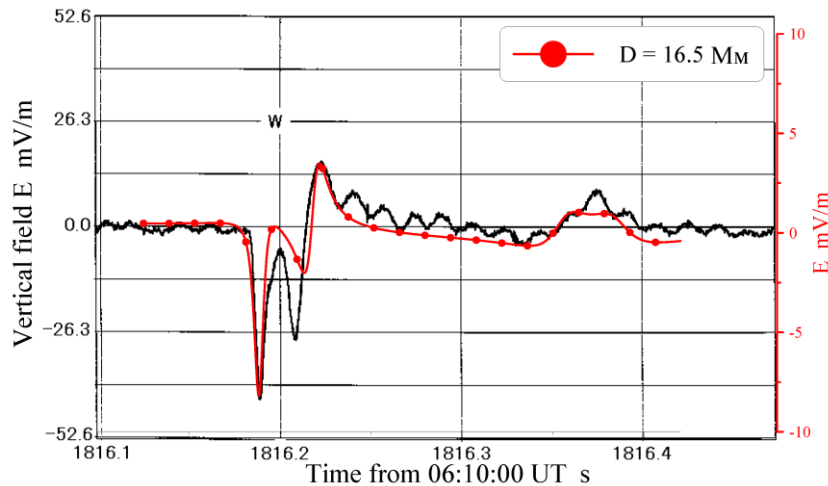


Figure 25: Observed (black) and the model (red) waveforms of the Q-burst

Usually the SOD is evaluated from the spectral patterns of natural ELF pulses. It was shown in [Jones, 1970b] that the amplitude spectra of E- and H- field components have the unique outline corresponding to the SOD as seen in Figure 22 where amplitude spectra of electric and magnetic fields are shown.

Parametric ELF burst caused by the gamma flare on December 27, 2004

We already mentioned the impact of cosmic gamma flares on the background spectrum of the SR. The huge abrupt modification of the dayside atmosphere by gamma rays has altered the leakage current in the global Earth–ionosphere electric circuit. As a result, a parametric ELF radio pulse was radiated, which was successfully detected by the SR observatories where we continuously monitor the natural signal with the GPS time stamps [Nickolaenko and Hayakawa 2014 ; Tanaka et al., 2011 ; Schekotov et al., 2013 ; Nickolaenko et al., 2014].

We present in Figure 25 the simultaneous experimental records of this pulse at the set observatories. The field sites were: Moshiri, Japan (44.37°N; 142.24°E); Onagawa, Japan (38.43°N;

141.48°E); Erange, Sweden (67.83°N; 21.1°E); Karimshino, Russia (52.83°N; 158.13°E); Nagycenk, Hungary (47.6°N; 16.7°E); and Hornsund, Spitzbergen (77.0°N; 15.5°E).

At the observatories of Erange, Onagawa and Karimshino they recorded two orthogonal horizontal magnetic field components, and at the sites at Moshiri, Nagycenk, and Hornsund they registered two magnetic components and the vertical electric field. All records were supplied with the GPS time stamps, so that time axis of individual records might deviate by a few milliseconds utmost. Magnetic antennas at all observatories were oriented parallel to the geographic cardinal directions, except the Karimshino observatory where they are positioned along the geomagnetic coordinates. Owing to a rather small (-6.5°) magnetic declination at this site, the component D at Karimshino practically coincides with the field H_{WE} or H_X component and the projection H is the H_{SN} or H_Y field. The vertical electric field is exceptionally important for establishing the source polarity and finding the unambiguous source azimuth. Luckily, at many field sites we acquired the concurrent ELF records in many channels, but none of them presented the reliable simultaneous records in all three field components.

We show the collection of records made at six above-mentioned observatories in Figure 26. The time (UT) is shown along the abscissa in the ± 1.5 s vicinity of 21:30:26.5 UT, which is the arrival time of galactic gamma rays. The ordinates show the field amplitudes plotted in arbitrary units.

The upper plot depicts temporal variations of the vertical electric field at the Nagycenk observatory. Two distinct pulses are clearly seen here, and since their onsets are negative, we can state that both of them arrive from the source of positive polarity (the source current was directed downward). Horizontal magnetic field records are assembled in pairs of all other sites. Before plotting the data in Fig. 26, we had to remove the industrial noise with the help of the low-pass filters and the Singular Spectral Analysis (SSA), or the Caterpillar procedure. Relevant details might be found in [Nickolaenko and Hayakawa 2014]. This procedure removed both the 50 Hz interference and the high frequency noise.

Figure 26 demonstrates outstanding similarity of data collected worldwide, although some departures are obvious. Deviations originate from different propagation conditions and from the local noise. Also, there are differences arising from deviations in particular frequency characteristics of receiving equipment, however, we show the records as they were. Three thick black horizontal bars at the time axis denote sections containing the distinctive pulse fragments: 26.3–26.4; 26.5–26.6; and 26.7–26.95 s. After applying the wavelet analysis to the waveforms of horizontal magnetic fields, we

found relevant wave arrival angles (source azimuth A_Z) and conducted the source triangulation from the field sites for all these sections of the records. The azimuth A_Z is the angle between the local

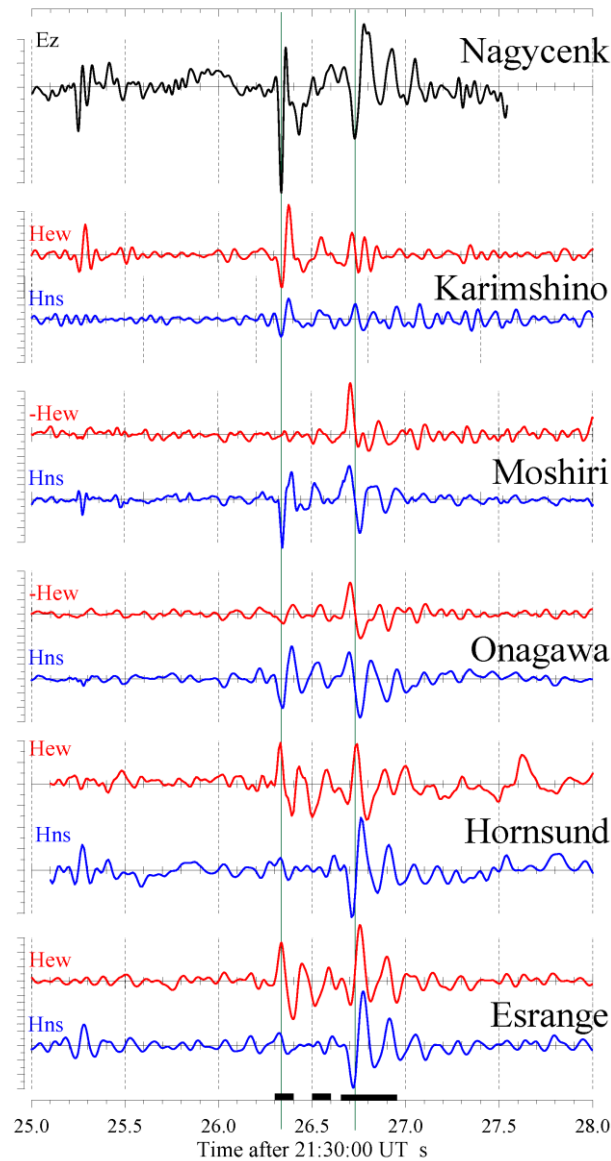


Figure 26: ELF records at different SR observatories. The (UT) is shown on the abscissa in the vicinity of the onset of gamma flare.

south–north direction (Y -axis) and the major axis of the wave polarization ellipse. The azimuth is counted clockwise, as a compass. Polarization characteristics were also computed through the elements $P_{YY} = \langle H_Y H_Y^* \rangle$, $P_{XX} = \langle H_X H_X^* \rangle$ and $P_{XY} = \langle H_X H_Y^* \rangle$ of the coherence matrix, which were derived from the spectra of the field components H_X and H_Y .

Preliminary model computations indicated the expected features of parametric pulse and thus facilitated the investigation. These were as follows:

1. The parametric pulse is formed around the arrival time of gamma rays.
2. Owing to the great size of parametric source, radio signal contains only the lowest SR modes.
3. The source polarity must be positive, i.e., the pulse onset must be negative in the vertical electric field.
4. Polarization of the pulsed magnetic field is linear, provided that modification of the global circuit was symmetric.
5. The wave arrival azimuth must point to the center of modification (20.4°S and 146.2°W).
6. Amplitude of the pulse must noticeably exceed the SR background.

All these features are present in the records shown in Figure 26. The problem is that these are pertinent to the couple of pulses: one occurred prior to the detection of gamma ray arrival, and the second one took place at the right time. Analysis indicated that the first, precursory pulse satisfied all demands except the early arrival time. The second pulse fitted all necessary characteristics, but the source triangulation was highly unstable (scattered). It was concluded having in mind this feature that the most probably both of these pulses were associated with the gamma flare.

A few words might be added concerning parametric excitation of SR transient signals in connection with recent successful detection of gravitational waves at 09:50:45 UT on September 14, 2015 [Abbot, 2016]. Possible modulation of the Earth–ionosphere cavity by a gravitational wave was modeled in [Minakov, et al., 1992]. It was shown that modification of SR by gravitational wave will be most pronounced at the second or the third resonance modes, which is conditioned by the geometry of modification and the finite propagation velocity. We will not go deeper in this issue and mention only the general outline of the phenomenon. Let the plane gravitational wave be incident on the Earth. The changes in the space-time metric will occur along the direction of propagation, so that modification of the Earth–ionosphere cavity will be similar to the polar non-uniformity. It will match the spatial field distribution of the second SR mode, so that the effect will reach its maximum at the frequency of gravitational wave ~ 14 Hz. If one takes into account the delay due to the propagation time of gravitational waves through the diameter of the Earth, it appears that the effect is enhanced at the 20 Hz or at the third mode. A parametric pulse (if any) originating in the Earth–ionosphere cavity from the gravitational modulation should occupy the band of 14 – 20 Hz. The gravitational wave [Abbot, 2016] was detected above the 60 Hz with a sharp maximum around 130 Hz, which excludes its possible detection by using SR. Thus, the Earth–ionosphere cavity was too large for an optimal detection of transient gravitational wave of year 2015. The smaller planetary cavities might be suitable for this task.

Distortion of signal waveform by a typical receiver

Computations of the pulse waveform at the output of a typical SR receiver showed that the signal shape is significantly disturbed: the pulse onset is delayed, substantial changes are possible in the amplitudes of positive and negative half-waves in the onset of pulsed signal, and the round-the-world and antipodal pulses become poorly distinguishable. We demonstrate below that the initial pulsed waveform might be partially restored when the phase modifications are compensated, which were caused by the receiver [Yatsevich et al., 2014].

A typical SR receiver has the finite bandwidth (usually, 4–40 Hz) and a rejection filter of the power supply frequency. Therefore, the pulsed waveforms might be modified beyond the recognition. Substantial delay might appear reaching tens of milliseconds, which might lead to wrong attribution when compared with other events. Changes in the positive and the negative excursions in the pulse onset might cause the problems in establishing the source polarity, especially in the presence of natural background resonance signal. An error in the arrival time of initial pulse and the smoothed antipodal and round-the-world waves might increase an error in determining the SOD. These features are important when analyzing the Q-burst records performed concurrently with the optical observations of TLEs in the mesosphere above the powerful lightning strokes, the so-called "red sprites".

It is clear that some correction is desirable of the experimental pulsed waveforms at the output of a typical SR receiver.

Changes in the waveform are mainly related to the phase characteristic of the receiver, and these might be compensated during the consecutive processing or during direct recording of the pulse in PC. The easiest way of compensating these distortions is the multiplication of the complex spectrum of the signal at the output of the receiver by the complex conjugate of the receiver gain. Model computations show that the inverse Fourier transform in this case will almost restore the correct pulsed waveform (apart from modifications due to finite bandwidth). Such operation is equivalent to the analog procedure of the "reverse playback", in which one takes the signal recorded at the receiver output, reverses it in the time, and sends it to the input of the same receiver. This procedure might be done by the "backward" playback of the tape recorder. In both of these cases, the phase shifts introduced by the receiver are completely compensated. Though the distortions remain that were caused by the finite bandwidth, and these are observed as smoothing and widening of the time domain signal. Moreover, the modification due to the receiver finite bandwidth will be enhanced owing to the squaring of the amplitude gain of the receiver in such operations.

The compensation procedure eliminates delays within the pulse and restores the original amplitudes of the positive and negative half-waves in the pulse onset. As a result, more accurate and fair assessment of the source parameters is obtained: the arrival time, the polarity, and the SOD. An example of such a processing is shown in Figure 27. Here, we show the actual record of the vertical electric field component of a Q-burst performed on January 21, 2001 at 22:54:12 UT at the Lehta observatory. The sampling rate was 204 Hz. Time in milliseconds is plotted on the abscissa, and the strength of vertical electric field is shown along the ordinates in arbitrary units. The red line in the upper panel shows the $E_z(t)$ signal recorded at the output of SR receiver. The blue line in the lower frame depicts the same pulse after compensation of the receiver phase characteristic. We computed the complex Fourier spectrum of the recorded pulse, multiplied it by the complex conjugate of the known receiver gain, and performed afterwards the inverse Fourier transform, which returned the records into the time domain. The through calibration of the complex gain of the receiver electric channel was regularly made at the observatory with the help of a special radiating rod antenna.

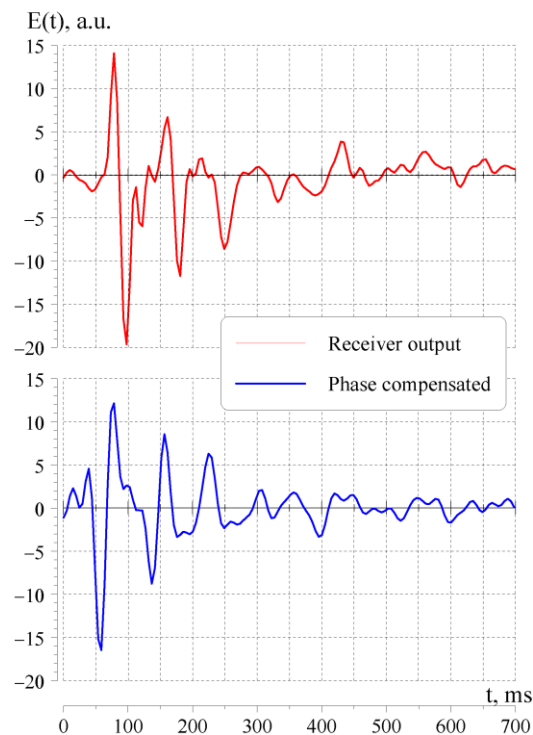


Figure 27: Waveforms of a Q-burst with and without compensation of the receiver phase characteristic

As might be seen from Figure 27, the phase characteristic of the real receiver has caused a significant (~ 40 ms) delay of the recorded pulse onset (red curve in upper plot) relative to its actual initiation (blue curve in the lower plot). It is important that after compensation of the phase

distortions one perceives that the observed Q-burst signal starts with the negative excursion. This suggests that it is originated from the positive cloud-to-ground stroke. It is remarkable that the red curve in Figure 27 started with the positive half-wave. Thus, the particular signal shape might be altered by the equipment, which definitely would impede its application in geophysical studies. Compensation of the receiver gain is strongly desirable.

4. Detection of artificial ELF signals

The ELF radio propagation in the Earth-ionosphere cavity can also be studied by using ELF transmissions. There are only two ELF transmitters in the world. The first one is the United States WTF/MTF (Wisconsin Transmitter Facility/Michigan Transmitter Facility) having two crossed transmitting antenna, and it operates at the center frequency of 46 and 76 Hz [Bannister, 1999 ; Fraser-Smith and Bannister, 1998]. The second one is the Russian Kola Peninsula Transmitter (KPT, working at 82 Hz [Bannister, 1999; Fraser-Smith and Bannister, 1998; Nickolaenko, 2008]. We present data on the Russian KPT transmissions detected in Japan, Antarctica and in the Atlantic Ocean.

The center of KPT antenna is approximately located at the geographic coordinates (68.8°N and 34.5°E). As described in [Velikhov et al., 1996], the transmitter consists of two swept-frequency generators of sinusoidal voltage and two parallel horizontal grounded wire antennas, each about 60 km long. The generator provides currents from 200 to 300 A in the antennas in the frequency range from 20 to 250 Hz.

Observation on the Russian KPT transmissions detected in:

(i) Japan

Our data present the particular frequency of 82 Hz, and the ELF equipment was placed at Moshiri in Japan. The detailed information might be found in [Yano et al., 2010]. We only note here that the long-term data covering a whole year of 2007 indicated that the measured signal amplitude is consistent with earlier results [Fraser-Smith. and Bannister, 1998]; the wave polarization was linear, and the source bearing found by the goniometer technique agrees with the geometry of experiment.

Two horizontal magnetic fields H_{SN} and H_{WE} were detected by induction coil magnetometers and the vertical electric field E_Z was received by the ‘ball’ antenna. The whole system was calibrated before installation, so that the absolute amplitudes were obtained of the ELF fields. The sampling

frequency was 4 kHz and the ELF waveforms were continuously recorded on the hard disk of the PC. The relative position of observatory and of KPT corresponds to the wave arrival angle of 24.8° from North to West, which was in fact the source bearing found in the measurements. The recorded signals were processed by using FFT procedure with the segments of data 65.536 s long, so that relevant frequency resolution was 0.01526 Hz. The amplitude spectra of each field component were computed every 60 seconds, and thus we obtained dynamic spectra with temporal resolution of 1 minute [Yano et al., 2010].

After deriving the amplitude spectra $|H_{SN}(f)|$ and $|H_{WE}(f)|$, the amplitude spectrum was found of the total horizontal magnetic field $H_\phi = [H_{SN}^2 + H_{WE}^2]^{1/2}$. Concurrently, the phase difference was deduced of the two horizontal magnetic fields $\Delta(f) = \theta_{SN}(f) - \theta_{WE}(f)$ where $\theta_{SN}(f) = \arg[H_{SN}(f)]$ and $\theta_{WE}(f) = \arg[H_{WE}(f)]$ are the arguments of the complex spectra $H_{SN}(f)$ and $H_{WE}(f)$ correspondingly. The phase difference Δ determines the ELF wave polarization.

Figure 28 depicts the signal characteristics detected on the particular day of January 08, 2007. The lowest panel here shows diurnal variations of the signal amplitude that reach $0.2 \mu\text{A/m}$. Intervals of the man-made signal reception are marked by the boxes in the figure. One may note from the amplitude data that the maximal signal-to-noise ratio was about 5.

Dots in the top panel of Figure 28 present the orientation of the complete magnetic field vector ϕ_H . The angle $\phi_H \approx 65^\circ$ was found from the orthogonal components H_{SN} and H_{WE} , and it is connected with the wave arrival angle ϕ_k by the relation $\phi_k = \phi_H \pm 90^\circ$, and the wave arrival angle was found from the formula: $\phi_k = \tan^{-1} [H_{SN}(f)/H_{WE}(f)]|_{f=82 \text{ Hz}}$. Thus, the direction to the source was $\phi_k \approx -25^\circ$ (rotation from North to West), which is very close to the geometrical estimate. One may observe that the arrival angle usually fluctuates due to the presence of natural ELF noise originating from the global thunderstorms. When the man-made signal appears, the wave arrival azimuth becomes stable, as seen in the boxes in the figure.

Points in the middle panel of Figure 28 depict the dynamic spectrum of the phase difference $\Delta = (\theta_{WE} - \theta_{SN})$. When the artificial signal is absent and only atmospheric noise is detected, the phase difference covers the interval from -180 to $+180$ degrees. When the KPT signal appears, all points of the plot concentrate around zero, thus indicating on the linear polarization of the arriving radio wave. Thus, one can use the goniometer technique for establishing the source bearing.

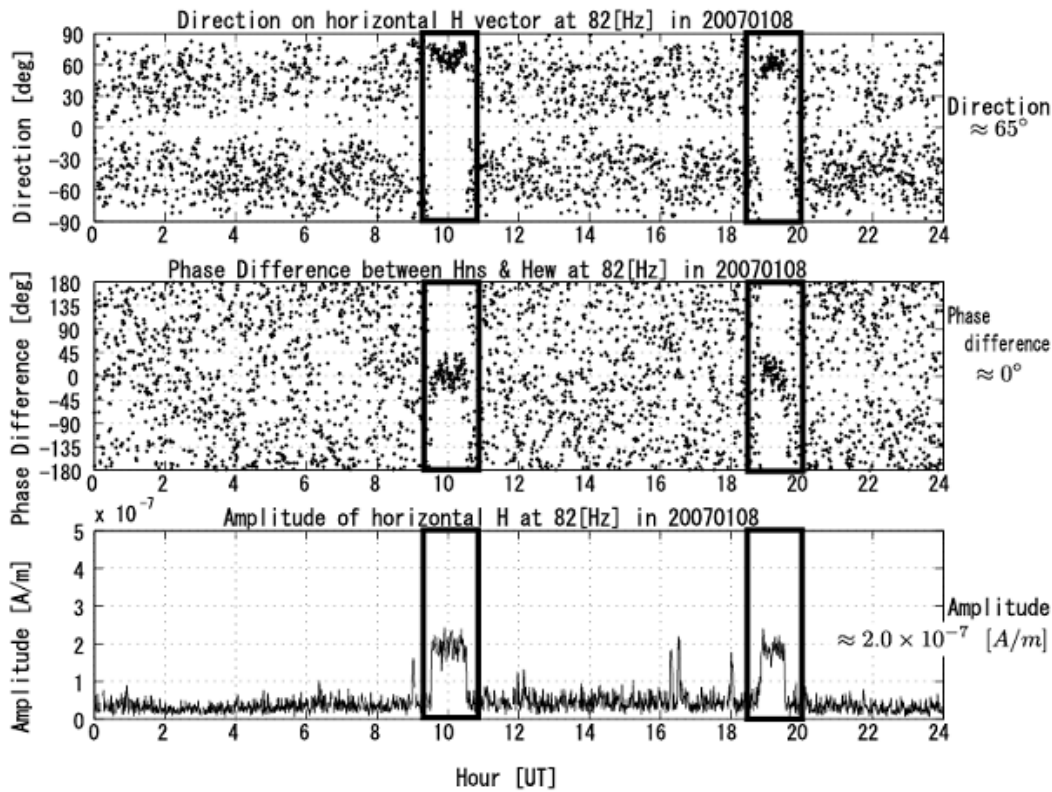


Figure 28: Records of man-made ELF radio signal on 8 January, 2007

Detected amplitude of transmitted radio signal had the average value of 2.0×10^{-7} A/m or -134 dB. The complex propagation constant $\nu(f)$ was estimated by using the characteristic heights h_E and h_M of the two-scale exponential profile [Bannister, 1999] for the ambient day and night conditions: $h_E^D = 55.1$ km and $h_M^D = 75.6$ km; $h_E^N = 75.6$ km and $h_M^N = 91.5$ km. The propagation constant was found from the standard equations pertinent to exponential profile. The wave attenuations rate was $\alpha_D = 1.33$ dB/Mm for the day and $\alpha_N = 0.82$ dB/Mm for the night conditions. The phase velocity (V) was characterized by $(c/V)_D = 1.245$ and $(c/V)_N = 1.12$ values. The model computations for the experiment geometry and the cosine angular pattern of transmitting antenna has predicted the signal amplitude of -137 dB at Moshiri (the distance of 6.2 Mm) [Yano et al., 2010], and its deviation from the measured -134 dB was attributed to the underestimated current moment of the source $M_L = 1.42 \times 10^{11}$ A/m². This estimate is higher than that found in [Fraser-Smith, and Bannister, 1998]: $M_L \approx 200(A) \cdot 55(km) \cdot 10(km) = 1.1 \cdot 10^5 (A \cdot km)^2$.

An additional point is the particular SOD of 6 Mm, which corresponds to the critical distance where the distance dependence intersects of the field amplitude in the ambient day and night

conditions [Nickolaenko, 2008]. This is why no significant day–night variations were observed. The physical explanation of the critical distance is rather simple. The wave attenuation is higher in the day propagation, and relevant amplitude decreases with distance faster than in the ambient night conditions. Simultaneously, the excitation factor of a source is greater in ambient day conditions. Thus, the rapidly decreasing ‘day’ curve starts from the higher initial amplitude, so it meets the nighttime curve at the critical distance of about 6 Mm. The absence of regular daily variations might play a positive role when the man-made signal is used to detect the seismogenic ionosphere disturbances.

(ii) Antarctica

The so-called KPT is one of the sources of artificial ELF radiation whose signals were clearly detected throughout the world [Fraser-Smith and Bannister, 1998]. A high amplitude signal was noted reaching –142 dB at the 16.5 Mm distance detected at Dunedin, New Zealand. The level was –151.9 dB at 18.3 Mm distance recorded at Arrival Heights, Antarctica.

We present the amplitude records performed at the “Bellinshausen” Soviet Antarctic station (62.2°S and 59°W) in February 1989. It is well known that the radiating horizontal grounded wire antenna acts as a vertical loop with the return current flowing through the Earth’s crust. Such an antenna is a horizontal magnetic dipole source. The maximum of its radiation pattern is found along the direction of horizontal wire ground (the east–west direction in our case). With the satisfactory accuracy one may apply the model of a vertical source current loop collinear to the geographic parallel centered at 68.8°N and 34.5°E.

The “Bellinshausen” station is situated at the Waterloo (King George) Island in the Drake Strait (62.2°S and 59°W). The SOD is equal to 16.25 Mm. Measurements were performed with one of two antennas: vertical electric or the horizontal magnetic antenna, and we present the electric field data here. The vertical electric antenna was a typical antenna with the 50 pF self-capacitance of active electrode mounted on the top the metallic mast 3 m high. The input resistance of electric antenna pre-amplifier was 10^9 Ohm.

The receiver of man-made signal was a narrow band RC filter designed as a combination of active low-pass and the high-pass filters. It provided the bandwidth of 0.8 – 1.0 Hz centered at the working frequency. The signal from this pre-selector was fed to the synchronous detector that performed additional filtering. The two stage synchronous detector had the integration time of 50 s, and it was locked-in with the high precision signal generator of 82.01 Hz frequency. Such a shift causes 0.01 Hz amplitude modulation (sinusoidal beating) at the detector output, provided that the

man-made radio signal arrives at the antenna. The amplitude of beating is directly proportional to that of the input radio signal. The slow fluctuations are observed in the absence of artificial radiation. The sensitivity of receiver was regularly checked and the effective height of the vertical electric antenna was about 1 m in the Antarctic measurements [Nickolaenko, 2008].

The output of synchronous detector was sent to the multi-channel pen recorder, and the 'beating' was clearly observed in the presence of man-made signal. Later, the paper chart was processed manually, and the beating amplitude was measured, averaged over 10-min intervals and fixed in the logbook.

Additional filtering and signal accumulation was performed simultaneously by the analog-digital spectrum analyzer. For this purpose, the output of synchronous detector was sampled in the spectrum analyzer with the sampling frequency of 0.25 Hz, and the instantaneous spectrum was obtained of the relevant beating wave. The frequency channel of the man-made transmissions was also logged by the chart record. Application of a spectrum analyzer allowed for extending the coherent accumulation time to 40 minutes, so that the signal-to-noise ratio was increased up to 10 – 12.

Experimental data are presented in Figure 29. The UT is plotted on the abscissa here, and the averaged amplitude variations are shown along the ordinate in the form of a histogram. The plot presents the averaged data recorded from Feb. 07 to Feb 14, 1999. The amplitude of vertical electric field is measured in dB relative to 5 $\mu\text{V/m}$. One may observe that signal amplitude increases by about 4 dB during the sunrise. It starts just before the local sunset, and the effect was noted in both electric and magnetic fields. An increase in the electric and magnetic fields indicates that the effect was conditioned by the decrease of wave attenuation on the propagation path. The relatively high amplitude was recorded all through the local night, and it noticeably reduced just before the local sunrise. Around the sunrise, the electric field amplitude showed a short, but distinct maximum, while the field remained small during the local day gradually increasing toward the night. The magnetic field amplitude behaves in a slightly different way: the narrow local peak in the amplitude was absent after the sunrise.

We also show in Figure 29 the results of simplistic modelling. The line with dots was obtained in the following way. According to the model [Nickolaenko, 2008] alteration in the wave attenuation factor from day to night was equal to 0.51 dB/Mm. For the path length of 16.25 Mm, the alteration increases the night amplitude by 8.3 dB in comparison with the day level. On the other hand, the daytime ionosphere is lower than the night ionosphere, and changes in the field excitation factor will work in the opposite direction: they will raise the daytime field by 2.3 dB. As a result, a transition

from the ambient day to the ambient night propagation conditions will be associated with the 6 dB field increase. By choosing the daytime amplitude of 1 dB, we obtain the night level of 7 dB. These two levels are shown by horizontal lines with dots in Fig. 29 linearly interpolated during the day-night transition period. One may observe that modelling agrees with observations.

The solid blue line in Figure 29 depicts the results of alternative interpretation. Now, the deviations in the field excitation factor are ignored, but the temporal changes at the day and night segments on the propagation path are more accurately accounted. The coordinates of the point $T(\theta_k, \varphi_k)$ are found on the propagation path where the sunrise (sunset) is observed at the given moment of universal time. This point divides the path into the “day” and the “night” portions, and the relevant field amplitude y_k in dB is calculate by using the following formula:

$$y_k = -1.33 \cdot d_D - 0.82 \cdot d_N \tag{41}$$

where d_D and d_N are the day and night portions of propagation path. The relevant amplitude variation is shown by the solid blue line in Figure 29 deviating from the linear interpolation. The range of amplitude variations increases owing to a disregard of modulations in the excitation factors.

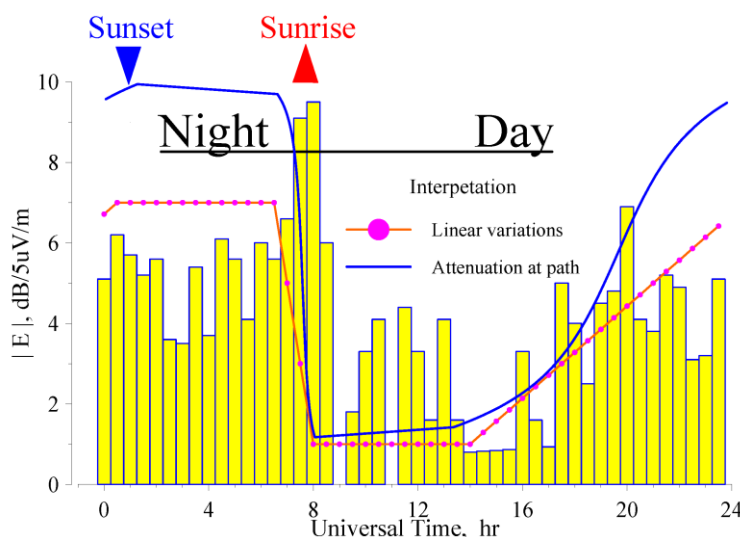


Figure 29 : Diurnal variations of man-made signal in Antarctica

The above explanations of experimental data account for the position of the day – night interface (solar terminator) that plays the key role. The localized peak around the sunrise time is definitely linked to the “gliding propagation” of the ELF radio wave when the day–night interface and the arc connecting the source and observer are almost coincident. Maps in Figure 30 indicate that the source

and observer are positioned nearby the solar terminator line when the field increases at the observatory. Such behavior suggests that the day–night interface is rather sharp. The transmitted radio wave is incident on the day – night interface with a gliding angle at UT= 7 – 8 hr, so that one can expect relatively high reflection at this time and a summation of the direct and reflected waves. The absence of the peak in the magnetic field component might be explained by the orientation of direct and mirror interfering vectors.

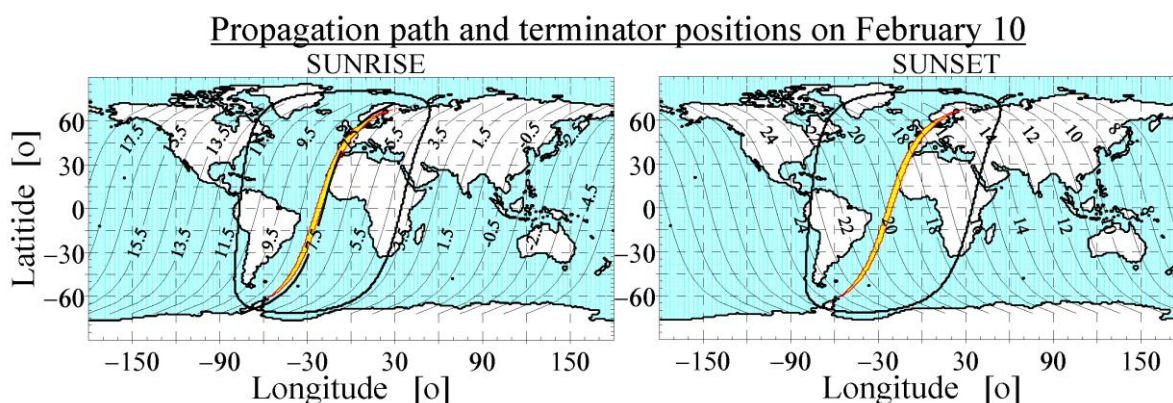


Figure 30: Global map with propagation path and the first Fresnel zone. Positions of morning (left frame) and evening (right frame) terminators are shown for different moments of UT. Time is printed on terminator lines.

The habitual terms “propagation path” and “wave reflection from the day–night interface” must be used at ELF with caution. One has to draw the “the radio beam” first, i.e. the first Fresnel zone as seen in Figure 30. Distant source and the receiver are positioned in the Northern and Southern hemispheres, and the first Fresnel zone is superimposed on the global map in the rectangular coordinates. It replaces the customary propagation path at ELF, and we show such a path (the first Fresnel zone) for the signal frequency of 4.1 kHz by the narrow yellow contour embracing the geodetic source – observer arc. This high frequency radio beam still has a considerable width of $\sim 4^\circ$, so that the terminator line crossed it in 15 minutes. Owing to a great path length and to the extremely low frequency, the first Fresnel zone covers the 110° longitude interval at 82 Hz, so that Africa and South America are found within this zone.

The morning terminator lines are shown on the ground surface in the left frame of Figure 30 for a set of sunrise time (UT) printed for February 10, 1989. Obviously, these lines are practically “parallel” to the source–observer arc. The right frame depicts geodetic lines of the evening terminator. When UT = 7.5 hr, the sun has already risen at the transmitter, and the point of the sunrise is found close to the Greenwich meridian at the propagation path. The morning terminator

line moves across the source–observer arc rather fast, about one hour. In contrast, the evening terminator (the right frame of figure) is almost perpendicular to this arc, and it crosses the source–observer arc during 11 hr. Thus, the February sunrise occurs almost simultaneously at the points of source–observer geodetic line, in spite the longitudinal separation of transmitter and observer exceeds 90°.

Sunrise and sunset are shown in Figure 29 by blue wedge and red triangle. The sunrise occurred at the transmitter around 6.7 hr UT, and the sunset takes place on 13.5 hr. Despite the wide Fresnel zone, the amplitude records of artificial ELF radio wave demonstrate the effect of terminator in an interval of UT from 6 to 9 hr. It looks like that the effect emerged from the great SOD combined with practically parallel positioning of the day–night interface and the source–observer geodetic line. Approximately the observed amplitude increase reached 100% (6–8 dB) at the 82 Hz signal frequency. If one assumes that the magnitude of terminator effect linearly varies with frequency, it must decrease to 10% at the first SR mode. This estimate agrees rather well with the rigorous model computations. Thus, observations of the man-made ELF radio signal correspond to those collected in the SR observations.

(iii) Atlantic Ocean

The vertical ELF field component from the KPT was recorded on board the “Professor Zubov” research vessel in the Atlantic Ocean from April to May 1989 during the return of 34th Soviet Antarctic expedition to the city of Leningrad [Nickolaenko, 2008]. The receiving vertical electric antenna was installed at the port side of navigation deck of the ship. The same antenna received the signals of the “Omega” VLF radio navigation system at 10.2 kHz, which allowed them to calibrate its effective height and obtain $h_{\text{eff}} = 1.1 \pm 0.1$ m. Thus the absolute values of the ELF field could be

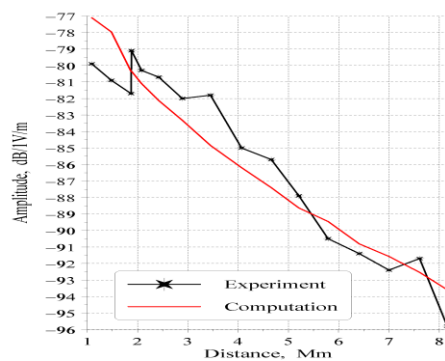


Figure 31: Field amplitude versus the SOD

obtained.

Measurements in the sea were made in the same way and with the same equipment as at the “Bellinshausen” Antarctic station [Nickolaenko, 2008]. The recorded field amplitude was averaged over the whole day, and this value was used as the function of the daily averaged SOD. The distance was calculated for the vessel coordinates for the the ship’s noon. Figure 31 depicts the distance dependence of the observed field amplitude. The abscissa shows the distance from the vessel to the center of radiating antenna in Mm. The ordinate depicts the field amplitude in dB relative to 1 V/m. The dotted curve shows the experimental data, and the smooth red line depicts the computed amplitude.

The ship coordinates during the measurements varied in the way that provided practical invariability of the “launching angle” at the transmitting antenna: variations of azimuth of observer seen at the transmitter were practically absent in the data set. Distance variations of the field amplitude indicated that the wave attenuation rate was $\text{Im}[\nu]_{f=82\text{ Hz}} = -0.9225$ Napier/radian. The estimate for the attenuation rate was obtained in the distance interval 1–8 Mm. The red line in Figure 31 shows the model computation of the field amplitude for the above attenuation rate with an account of slight alterations of the receiver azimuth relative the middle of radiating antenna. Obviously the model data are in excellent agreement with observations.

5. Tweek atmospherics (sferics)

Internal contradiction of experimental studies of transverse resonance: the resonance cannot be observed at a short distance from the source – no propagating waves. Observations at some distance suppose longitudinal propagation in the Earth-ionosphere duct at frequencies just above the modal cutoff. When the SOD substantially exceeds the waveguide effective height, the pulsed signal transforms into a tweek atmospheric (sferic). The following formula contains actually two independent branches of eigen-values.

$$k_{np} \approx \sqrt{\frac{n(n+1)}{a^2} + \left(\frac{p\pi}{b-a}\right)^2} \quad (42)$$

The first one is the SR condition pertinent to TM-waves that corresponds to $p=0$. The second branch of the solution corresponds to $p=1, 2, 3, \dots$. It describes the transverse resonance with characteristic frequencies corresponding to the condition $k(b-a) \approx p$. The second term under the square root in Eq. (42) becomes principal in this case, and we have the following expression for the transverse resonance frequency,

$$f_{np} \approx \frac{cp}{2(b-a)} \left[1 + \frac{1}{2} \frac{n(n+1)}{(p\pi)^2} \left(\frac{b-a}{a} \right)^2 \right] \quad (43)$$

which practically gives the relation $k_{pn}(b-a) = p\pi$ for an arbitrary n .

The basic transverse resonance ($p=1$) is found around 1.5-2.5 kHz frequency and is observed predominantly at night [Rafalsky , 1991 ; Shvets, 1994; Hayakawa et al., 1994]. Indeed for the ionospheric height of 100 km, we have $f_{10} = 1.5$ kHz with the corrections proportional to $n(n+1)$ term of approximately 1 Hz value [Hynninen, 1974]. This transverse resonance is a local phenomenon because of relatively high attenuation factor of about 20 dB/Mm at its frequencies. Such waves do not propagate over long distances from the sources. The frequencies (43) are regarded in the literature as the cut-off frequencies of the Earth-ionosphere waveguide [Wait, 1970; Galejs, 1972; Sukhorukov et al., 1992] because the p -th mode does not propagate at frequencies below f_{pn} . Still, special investigations had demonstrated that electromagnetic waves are indeed trapped in the transverse cross-section of the Earth-ionosphere guiding system [Rafalsky , 1991 ; Shvets, 1994].

5.1. *Tweaks as a diagnostic tool for the lower ionosphere*

Tweak atmospherics (tweaks) are electromagnetic pulses propagating in the natural Earth–ionosphere waveguide, and they represent a response of the natural cavity to the excitation by lightning discharges. Tweaks are formed due to small losses during night time in the ionosphere at altitudes from about 85 to 95 km, which effectively reflects ELF-VLF electromagnetic waves. A study of this altitude range in the ionosphere meets essential difficulties due to relatively small electron densities ($10\text{--}1,000 \text{ cm}^{-3}$).

The sources of probing radiation are both the transmitters of VLF navigation and communication systems, and the strokes of lightning. The amplitude and phase of narrow band signals from a VLF transmitter vary with changes of the waveguide height, the slope of electron density profile, with the irregularities appearing in the lower ionosphere close to the propagation path. Owing to the small VLF attenuation rate in the ambient night conditions and at the distances smaller than 3,000 km, significant contribution to the observed field concurrently with the basic normal wave (mode) is made by the modes of higher orders. This detail hampers substantially the solution of the inverse problem when deducing the waveguide parameters from the results of measurements of the narrow band radiation of VLF radio stations, so that tweaks are considered to be a useful natural means for radio sounding the lower ionosphere in a wide frequency band.

Tweaks were distinguished from the so-called “musical atmospheric disturbances” [Eckersley, 1925] as a separate phenomenon by Burton and Boardman [Burton and Boardman, 1933] who extensively studied interferences on submarine cables. Having a duration less than 1/8 second these distinct musical atmospherics were given their onomatopoeic name [Burton and Boardman, 1933]. “Tweaks practically always start above the 2000 Hz and reduce very rapidly toward a lower limiting frequency”. An example of tweak records is presented in Figure 32.



Figure 32: Early records of tweaks (oscillogram of tweaks) and the timing impulse frequency, 1000 Hz. Adapted from [Burton and Boardman, 1933].

Those authors explained the frequency change of tweaks based on the theory of multiple reflections of the pulse emitted by a lightning stroke from the Earth and from the ionosphere. The approach (as seen in Figure 33) was originally proposed by Barkhausen [Barkhausen, 1930] in an attempt to explain the formation of whistling atmospherics: “whistlers”. Observations [Burton and Boardman, 1933] showed that whistlers do not have a lower cutoff frequency, while the analysis of tweak atmospherics revealed such a limit.

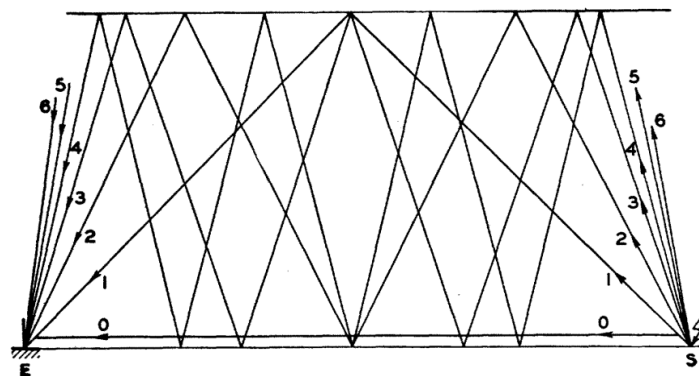


Figure 33: Multiple reflections of a lightning stroke pulse from the Earth and ionosphere. Adapted from [Barkhausen, 1930].

The analysis of tape recordings of tweaks was made by Burton and Boardman [Burton and Boardman, 1933] with the help of a sound spectrograph, and it revealed the presence of three distinct harmonics [Potter, 1951]. Lynn and Crouchley [Lynn and Crouchley, 1967] have demonstrated that the tweaks containing a few harmonics arrive from the sources at distances up to 3,000 km.

Owing to the reduced attenuation in the ionosphere, the spectrum of such signals increases nearby the cutoff frequencies of the Earth–ionosphere waveguide, and this allows us to estimate the reflection height and some other parameters of the lower ionosphere [Burton and Boardman, 1933; Reeve and Rycroft, 1972; Mikhailova and Kapustina, 1988; Yedemsky et al., 1992; Ryabov, 1994; Shvets and Hayakawa, 1998].

It was shown originally in [Singh and Singh, 1996] that the cutoff frequency of the Earth–ionosphere waveguide evaluated directly from the higher harmonics of a tweek deviate from the multiples of the cutoff frequency of the first (fundamental) harmonic. In particular, the proportionality coefficients of the cutoff frequencies for the second and third modes were a few percent higher than the corresponding integers. So the lower ionosphere edge cannot be described by a sharp boundary when one treats the propagation of wideband ELF–VLF radio signals.

In turn, measurements of the cutoff frequencies of several modes in a tweek provide an opportunity for evaluating parameters of the conductivity profile of the lower ionosphere [Shvets et al., 2014].

5.2. Basic equations

To calculate field components from a vertical electric dipole it is necessary to sum up contributions from all waveguide modes propagating at a given frequency. The following equations give the vertical electric and horizontal magnetic field components on the Earth’s surface from the dipole source with the source current moment $M_C(\omega)$ at a distance D [Wait, 1970]:

$$E_r(\omega) = -i\eta \frac{M_C(\omega) \exp(-i\pi/4)}{h\sqrt{\lambda a \sin D/a}} \sum_{p=0}^{\infty} \delta_p S_p^{3/2} \exp(-ikS_p D) \quad (44)$$

$$H_\varphi(\omega) = i \frac{M_C(\omega) \exp(-i\pi/4)}{h\sqrt{\lambda a \sin D/a}} \sum_{p=0}^{\infty} \delta_p S_p^{1/2} \exp(-ikS_p D) \quad (45)$$

$$H_\rho(\omega) = i \frac{M_C(\omega) \exp(-i\pi/4)}{h\sqrt{\lambda a \sin D/a}} \sum_{p=0}^{\infty} C_p P_p \delta_p S_p^{1/2} \exp(-ikS_p D) \quad (46)$$

where η is the free space impedance. To calculate values of $S_p = (1 - C_p^2)^{1/2}$ for the perfectly conducting Earth and anisotropic ionosphere it is necessary to obtain the solution of the following dispersion equation [Wait, 1970; Budden, 1952],

$$W = 0, \quad W \equiv \left(e^{i2khC} {}_{-||} R_{||} \right) \left(e^{i2khC} {}_{+\perp} R_{\perp} \right) {}_{+||} R_{\perp} {}_{\perp} R_{||}, \quad (47)$$

where the excitation factor is determined by $\delta_p = i2khC_p \left(e^{i2khC_p} {}_{+\perp} R_{\perp} \right) e^{i2khC_p} / \left(\frac{dW}{dC} \right)_{C=C_p}$, and the reflection coefficient matrix \mathbf{R} was calculated for homogeneous and inhomogeneous models of

anisotropic ionosphere with quasi-longitudinal or arbitrary [3, 111] direction of the Earth's magnetic field. The polarization factor of a particular mode $P_p = \frac{R_{\parallel}}{R_{\perp} + e^{i2khC_p}}$ is the ratio of the complex amplitudes of the horizontal components of the magnetic field in and perpendicular to the plane of incidence [Budden, 1952].

Approximate solutions for tweek fields near cutoff frequencies were obtained in [Sukhorukov et al., 1992; Ryabov, 1994; Sukhorukov, 1992; Sukhorukov, 1996] that allowed us to obtain analytical expressions connecting the parameters of the lower ionosphere with peculiarities in the spectra of tweeks.

5.3. Methods for tweek analysis

The first analysis was aimed at the distance from the lightning stroke and the effective height of the reflecting layer in the ionosphere, and the time–frequency variation was used of the individual tweek [Burton and Boardman, 1933]. The instantaneous frequency of the signal was determined as the reciprocal of the time delay between two successive peaks in the signal waveform fixed by an oscillograph. The results of frequency determination (curves A and B) are presented in Figure 34, where also the curve C calculated based on the multiple reflection theory [Barkhausen, 1930] is shown for the distance of 1770 km and ionosphere height of 83.5 km.

To determine the parameters of the waveguide by using the tweek signal, it is necessary to know the coordinates of the source, and these might be obtained from the independent networks of lightning location [Cummer and Bell, 1998; Rodger et al., 2005]. However, this information is provided on a commercial basis, and the realization of the lightning location network is technically difficult and expensive. Therefore, the single-position techniques are used that allow for locating the parent lightning strokes from the analysis of tweeks.

A method based on measurements of two orthogonal magnetic and vertical electric component of the tweek field was proposed by Rafalsky et al. [Rafalsky et al ., 1995a ; Rafalsky et al ., 1995b] and termed later as “Kharkov method” [Rafalsky et al ., 1995b]. The phase spectrum of a single mode related to the time of the signal reception is determined by $kD(S_n - 1)$, where k is again the wave number in free space, D is the SOD, and S_n is again the complex sine of the modal incidence angle. While the waves propagating under grazing incidence angles are of little utility to estimate the waveguide height, the frequency band near a cutoff frequency should be chosen. The single TE_1 mode can be isolated in the frequency band between the first and the second order mode cutoffs in the

spectrum of the longitudinal magnetic component. The source azimuth is determined by finding direction of the Poynting vector averaged over a wide frequency range and the longitudinal magnetic component is extracted by the rotary coordinate system transformation. In the model of the perfectly conducting plane waveguide the phase spectrum of the TE₁ mode is determined as follows: $F_1 = kD\{[1-(\pi/kh)^2]^{1/2} - 1\}$ and the inverse problem solution is reduced to fitting F_1 to an experimental phase spectrum by choosing the two parameters h and D . The method was validated in [Brundell et al., 2002] by a comparison with results of lightning location using a network of Lightning Positioning and Tracking System (LPATS) with sub kilometer location accuracy. The accuracy of the distance finding of the “Kharkov method” was estimated to be 74 km for distances at least greater than 1,000 km.

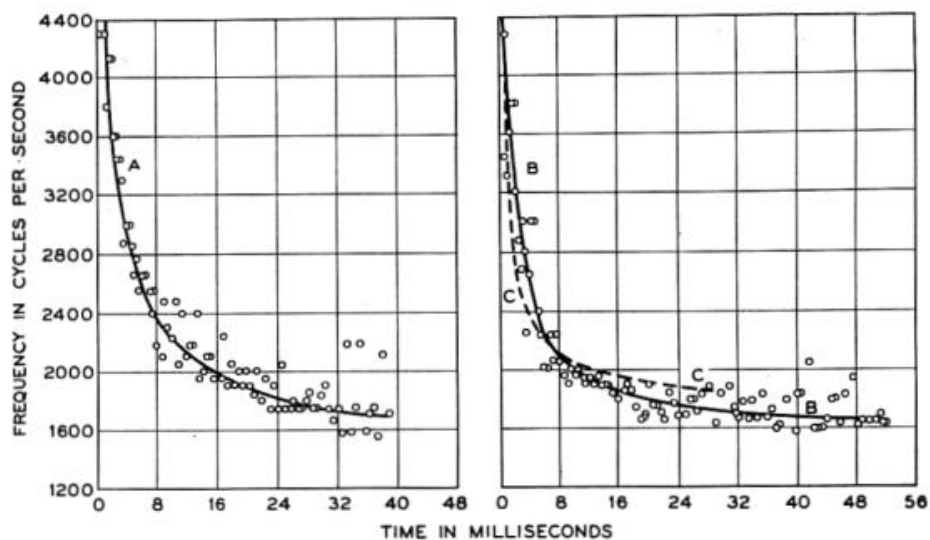


Figure 34: A and B, tweek frequency variation curves, and C, computed curve. Adapted from [Burton and Boardman, 1933].

Another traditional approach consists in measuring the time delay between the waves of different frequencies pertinent to the same tweek, and the retard arises from the frequency dispersion in the waveguide [Outsu, 1960; Ohya et al., 2008]. By using the delay measured at several frequencies, one can estimate both the distance from the source and the height of the waveguide.

Deducing the waveguide parameters for the higher-order modes presents a significant problem, since the phase and amplitude spectra as a whole are formed by interference of several waveguide modes. Resting on the Barkhausen’s multiple reflection theory we can simply obtain an analytical expression for the instant frequency in a tweek. It is obvious from Figure 33 that the propagation time for the path with n reflections from the ionosphere is equal to,

$$t_n = \frac{1}{c} \sqrt{D^2 + (2nh)^2}, n = 0, 1, 2, \dots \quad (48)$$

where $h = b - a$ is the effective height of the waveguide and D is the distance between the lightning and observer. The instant frequency is defined by derivative t_n by n from (48) [Yano et al., 1989]:

$$f = \frac{1}{dt_n/dn} = \frac{c}{2h} \left[1 - \left(\frac{D}{ct} \right)^2 \right]^{-1/2}, \quad (49)$$

where t is the time counted from the moment of lightning origin.

This expression is obtained also from the frequency dispersion relation for the group velocity of the first order waveguide mode [Hayakawa et al., 1995]. The waveguide mode theory yields that the value $f_c = c/(2h)$ in Eq. (49) is the cutoff frequency of the first order mode. The strong frequency dispersion of tweek harmonics is associated with a sharp reduction in the group velocity of radio waves propagating in the Earth–ionosphere waveguide when the signal frequency approaches the cut-off frequency of the waveguide. The cutoff frequency for higher order modes can be obtained by dividing the waveguide height by the mode number p :

$$f_{cp} = \frac{pc}{2h} \quad (50)$$

Let $\tau = t - D/c$ be the time from the moment of arrival of the direct ray to the observer, then the instant frequency of Eq. (49) for the p^{th} order mode transforms to the following expression:

$$f(\tau) = f_{cp} \left[1 - \left(\frac{D}{D + c\tau} \right)^2 \right]^{-1/2}, \quad (51)$$

In spite of simplicity of the model this formula proves to be useful in tweek analysis to find both the source range and effective waveguide height along the propagation path of a tweek by fitting the theoretical dependence (51) to experimental one till present time [Shvets, et al, 2014; Ohya et al., 2008]. In particular, when analyzing higher order harmonics in tweeks it becomes possible to estimate the frequency dependence of the effective reflection altitude and in such a way, parameters of the vertical conductivity profile of the lower ionosphere. An example of analyses of experimental tweek records [Budden, 1952] is demonstrated in Figure . 35.

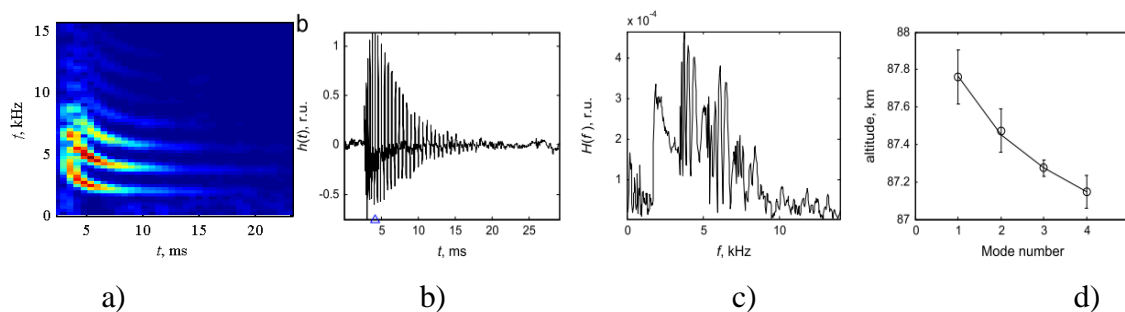


Figure 35 : Dynamic spectrum (a), waveform of the longitudinal magnetic component (b), its amplitude spectrum (c) and estimated effective heights (d) for different waveguide modes for the tweak recorded at 5.55° E, 16.7° S on January 21, 1991, at 20:29:22 UT. The estimated distance to the source and parameters of the exponential ionospheric conductivity profile are as follows: $D=1190$ km, $h_1=86.1$ km, $\zeta_0=0.44$ km. The circle points with the standard deviation bars in (d) denote effective heights experimentally found, and the solid line is the fitted theoretical dependence of h_1 from Eqs. (22, 23) which yields the estimated parameters h_1 and ζ_0 .

6. Other ELF related topics

This review has dealt with the main parts of subionospheric ELF radio wave propagation (fundamental theory, ELF natural noise (stationary and non-stationary), ELF transmitter signals, and their use to deduce different geophysical information such as space weather effects etc), but many other related topics are still existing, so we will list only a few below.

Other important directions are extensively pursued recently with the use of ELF waves treated in this review: studies of TLEs in the mesosphere originating from the powerful positive lightning discharges, because the whole view of TLEs is closely related to the most fundamental physics of lightning (charge generation, acceleration of particles by the electric field etc.). This topic is also addressed in the monographs [Nickolaenko and Hayakawa, 2014; Surkov, and Hayakawa, 2014]. Finally, we must also mention the attempts of detecting and applying the global electromagnetic resonance on other planets of the solar system (Venus, Mars, Titan etc) and implications of the use of SR data in detecting the environmental modifications by seismic and pre-seismic activity dedicated to earthquake prediction [Hayakawa, 2015; Molchanov and Hayakawa 2008]. These issues are exceptionally interesting, but they are beyond the scope of this brief review.

References

- Abbot, B.P. et al., Observations of gravitational waves from binary black hole merger, *Phys. Rev. Lett.*, 116, 061102, 16, 2016.
- Ayurov, D., and Bashkuev, Yu. B., Schumann resonances in high latitudes, *MSMW 2016 Symposium*, Kharkov, June 2016.
- Bannister, P. R., Further examples of seasonal variations of ELF radio propagation parameters, *Radio Sci.*, 34, No.1, 199–208, 1999.
- Barkhausen, H., Whistling tones from the Earth, *Proc. IRE*, 18, 1,155–1,159, 1930.
- Bliokh, P.V., Nickolaenko, A.P., and Filippov, Yu. F., Schumann Resonances in the Earth–ionosphere Cavity, *Peter Perigrinus*, London, 1980.
- Brundell, J.B., Rodger, C.J., and Dowden, R.L., Validation of single station lightning location technique, *Radio Sci.*, 37, No 4, 1059–1067, doi: 10.1029/2001RS002477, 2002.
- Budden, K. G. , The propagation of a radio atmospheric---II, *Phil. Mag.*, 43, 1179, 1952.
- Burke, C. P. and Jones, D. Ll., Global radiolocation in the lower ELF frequency band, *J. Geophys. Res.*, 100, 26,263 – 26, 271, 1995.
- Burke, C.P. and Jones, D. Ll., On the polarity and continuing currents in unusually large lightning flashes deduced from ELF events, *J. Atmos. Terr. Phys.*, 58, 531–540, 1996.
- Burrows, M.L., ELF Communications Antennas, *Peter Peregrinus*, London, 245, 1978.
- Burton, E.T. and Boardman, E.M., Audio-frequency atmospherics, *Proc. IRE*, 21, 1,476–1,494, 1933.
- Burton, E.T. and Boardman, E.M., Effects of solar eclipse on audio frequency atmospherics, *Nature*, 131, 81–82, 1933.
- Christian, H. J., Blakeslee, R. J., Boccippio, D. J., Boeck, W. L., Buechler, D. E., Driscoll, K. T., Goodman, S. J., Hall, J. M., Koshak, W. J., Mach, D. M. and Stewart, M. F., Global frequency and distribution of lightning as observed from space by the Optical Transient Detector, *J. Geophys. Res.*, 108(D1), 4005, doi:10.1029/2002JD002347, 2003.
- Cole, R.K. and Pierce, E.T., Electrification in the Earth's atmosphere from altitudes between 0 and 100 kilometers. *J. Geophys. Res.*, 70 (11), 2,735–2,749, 1965.
- Cummer, S.A., Inan, U.S., and Bell, T.F., Ionospheric D-region remote sensing using VLF radio atmospherics, *Radio Sci.*, 33, No. 6, 1,781–1,792, 1998.
- Eckersley, T. L., Note on musical atmospheric disturbances, *Phil. Mag.*, 49 (5), 1,250–1,259, 1925.

Fraser-Smith, A.C. and Bannister, P. R. , Reception of ELF signals at antipodal distances, *Radio Sci.*, 33, 83–88, 1998.

Füllekrug, M., Dispersion relation for spherical electromagnetic resonances in the atmosphere, *Phys. Lett. A*, 275, 80 – 89, 2000.

Galejs, J., Terrestrial Propagation of Long Electromagnetic Waves, *Pergamon Press, New York*, 362, 1972.

Galuk, Yu.P., Nickolaenko, A.P., and Hayakawa, M., Comparison of exact and approximate solutions of the Schumann resonance problem for the knee conductivity profile, *Telecommun. Radio Eng.*, 74 (15), 1,377-1,390, 2015.

Gradstein, C. and Ryzhik, I.M., Tables of Integrals, Sums, Series and Products, *Phys-Math Publ., Moscow (in Russian)*, 1963.

Greifinger, C. and Greifinger, P., Approximate method for determining ELF eigenvalues in the Earth–ionosphere waveguide, *Radio Sci.*, 13, 831–837, 1978.

Harth, W., Theory of low frequency wave propagation, in Handbook of Atmospherics, Ed. by H. Volland, Vol. 2, *CRC Press, Boca Raton, FL*, 133–202, 1982.

Hayakawa, M., Earthquake Prediction with Radio Techniques, *John Wiley & Sons, Singapore*, 289, 2015.

Hayakawa, M., Nickolaenko, A. P., Shvets, A. V. and Hobara, Y., Recent studies of Schumann resonance and ELF transients, in Lightning: Properties, Formation and Types, Ed by M.D. Wood, *Nova Sci Pub., Ch. 3*, pp.39 – 71, 2011.

Hayakawa, M., Ohta, K., and Baba, K., Wave characteristics of tweek atmospherics deduced from the direction finding measurement and theoretical interpretation, *J. Geophys. Res.*, 99, 10,733–10,743, 1994.

Hayakawa, M., Ohta, K., Shimakura, S. and Baba, K., Recent findings on VLF/ELF spherics, *J. Atmos. Terr. Phys.*, 57, 5, 467-477, 1995.

<http://www.interscience.wiley.com:83/eeee/57/1257/W.1257-toc.html>.

Huang, E., Williams, E., Boldi, R., Heckman, S., Lyons, W., Taylor, M., Nelson T., and Wong, C., Criteria for sprites and elves based on Schumann resonance observations, *J. Geophys. Res.*, 104, 16,943–16,964, 1999.

Hutchins, M. L., Holzworth, R. H., Brundell, J. B. and Rodger, C. J., Relative detection efficiency of the World Wide Lightning Location Network, *Radio Sci.*, 47, RS6005, doi:10.1029/2012RS005049, 2012.

Hynninen, E.M., On the high-frequency resonance oscillations of electromagnetic field in the Earth–ionosphere cavity, in Problems of Wave Diffraction and Propagation, 21, *Leningrad State University Press*, 150–154 (in Russian), 1974.

Hynninen, E.M. and Galuk, Yu.P. , Field of vertical dipole over the spherical Earth with non-uniform along height ionosphere, in Problems of Diffraction and Radio Wave Propagation, Vol. 11, *Leningrad State University Press, Leningrad*, 90–120 (in Russian) ,1972.

Inan, U. S., Lehtinen, N. G., Moore, R. C., Hurley, K., Boggs, S., Smith, D. M. and Fishman, G. J., Massive disturbance of the daytime lower ionosphere by the giant γ –ray flare from magnetar SGR 1806–20, *Geophys. Res. Lett.*, 34, L08103, doi:10.1029/2006GL029145, 2007.

Ishaq, M. and Jones, D. Ll., Method of obtaining radiowave propagation parameters for the Earth–ionosphere duct at ELF, *Electronic Letters*, 13(2), 254–255, 1977.

Jones, D. Ll., The apparent resonance frequencies of the Earth–ionosphere cavity when excited by a single dipole source, *J. Geomagn. Geoelectr.*, 21, 679–684, 1969.

Jones, D. Ll., Numerical computations of terrestrial ELF electromagnetic wave fields in the frequency domain, *Radio Sci.*, 5, 803 – 809, 1970.

Jones, D. Ll., Propagation of ELF pulses in the Earth-ionosphere cavity and application to slow tail spherics, *Radio Sci.*, 5, 1,153–1,163, 1970.

Jones, D. Ll. and Knott, M., Comparison of simplified and full-wave ELF propagation models, Abstracts of Reports at XXVI URSI General Assembly, Section E6-10, Toronto, 295, 1999.

Kudintseva, I.G., Nickolaenko, A.P., Rycroft, M.J., and Odzimek, A., AC and DC global electric circuit properties and the height profile of atmospheric conductivity, *Ann. Geophys.*, in press, 2016.

Lynn, K.J.W., and Crouchley, J., Night-time spheric propagation at frequencies below 10 kHz, *Aust. J. Phys.*, 20, 101–108, 1967.

Madden, T. and Thompson, W., Low frequency electromagnetic oscillations of the earth–ionosphere cavity, *Rev. Geophys.*, 3, 211–254, 1965.

Melnikov, A., Price, C., Satori, G., and Füllekrug, M., Influence of solar terminator passages on Schumann resonance parameters, *J. Atmos. Solar-Terr. Phys.*, 66, doi:10.1016/j.jastp.2004.05.014, 2004.

Mikhailova, G.A., and Kapustina, O.V., The frequency-time structure of “tweek”-type atmospheric and VLF diagnostics of parameters of the night-time lower ionosphere, *Geomagn. Aeron.*, 28, 879–882, 1988.

Minakov, A.A., Nickolaenko, A. P., and Rabinowicz, L. M. , Transformation of gravitational waves into electromagnetic by the electrostatic field in the Earth-ionosphere cavity, *Izvestija vuzov, Radiofizika*, 35, No. 6-7, 488-497, 1992, (in Russian). [Translated into English: Minakov, A.A., Nickolaenko, A.P., Rabinowicz, L.M., Gravitational-to-electromagnetic wave conversion in electrostatic field of earth-ionosphere resonator, *Radiophysics and Quantum Electronics*, Vol. 35, No. 6, 318-323, 1992.

Molchanov, O.A., and Hayakawa, M., Seismo Electromagnetics and Related Phenomena: Histroy and latest results, *TERRAPUB*, Tokyo, 189, 2008.

Mushtak, V.C., and Williams, E., Propagation parameters for uniform models of the Earth-ionosphere waveguide, *J. Atmos. Solar-Terr. Phys.*, 64(6), 1,989–2,001, 2002.

Nelson, P. H., Ionospheric perturbations and Schumann resonance data, *Ph.D. Thesis, MIT*, Cambridge Mass, 1967.

Nickolaenko, A. and Hayakawa, M., Schumann Resonance for Tyros (Essentials of Global Electromagnetic Resonance in the Earth–Ionosphere Cavity), *Springer, Springer Geophysics Series XI, Tokyo*, 348, 2014.

Nickolaenko, A. P., and Hayakawa, M., Resonances in the Earth-ionosphere Cavity, *Kluwer Academic Publ., Dordrecht*, 380, 2002.

Nickolaenko, A. P., Koloskov, A.V., Hayakawa, M., Yampolski, Yu.M., Budanov, O.V., and Korepanov, V.E. 11-year solar cycle in Schumann resonance data as observed in Antarctica, *Sun and Geosphere*, 10, No. 1, 39–49, 2015.

Nickolaenko, A. P., Pechony, O., and Price, C., Model variations of Schumann resonance based on Optical Transient Detector maps of global lightning activity, *J. Geophys. Res.*, 111, D23102, doi:10.1029/2005JD006844, 2006b.

Nickolaenko, A. P., Schekotov, A. Yu., Hayakawa, M., Hobara, Y., Satori, G., Bor, J., and Neska, M., Multi-point detection of the ELF transient caused by the gamma flare of December 27, 2004, *Radiophysics and Quantum Electronics*, 57, No. 2, 125–140, 2014.

Nickolaenko, A. P., Yatsevich, E. I., Shvets, A. V., Hayakawa, M. and Hobara, Y., Universal and local time variations deduced from simultaneous Schumann resonance records at three widely separated observatories, *Radio Sci.*, 46, RS5003, doi:10.1029/2011RS004663, 2011.

Nickolaenko, A.P., ELF attenuation factor derived from distance dependence of radio wave amplitude propagating from an artificial source, *Telecommun. Radio Eng.*, 67, No. 18, 1621 – 1629, 2008.

Nickolaenko, A.P., Impact of the Ionosphere day-night non-uniformity on amplitude of ELF radio signal, *Telecommun. Radio Eng.*, 67, No.5, 437-455, 2008.

Nickolaenko, A.P. and Rabinowicz, L.M., Possible global electromagnetic resonances on the planets of the solar system, Translated from *Kosmicheskie Issledovaniya*, Plenum Publishing Corporation , 20, No. 1, 82 – 88, 1982.

Nickolaenko, A.P., and Rabinowicz, L.M., Applicability of ultralow – frequency global resonances for investigating lightning activity on Venus, Translated from *Kosmicheskie Issledovaniya*, Plenum Publishing Corporation, 25, No. 2, 301 – 306, 1987.

Nickolaenko, A.P., Galuk, Yu.P., and Hayakawa, M. , Vertical profile of atmospheric conductivity that matches Schumann resonance observations, *Springer Plus*, 5, 108, DOI 10.1186/s40064-016-1742-3, 2016.

Nickolaenko, A.P., Hayakawa, M., and Sekiguchi, M., Variations in global thunderstorm activity inferred from the OTD records, *Geophys. Res. Lett.*, 33, L06823, doi:10.1029/ 2005GL024884, 2006a.

Nickolaenko, A.P., Hayakawa, M., Ogawa, T., and Komatsu, M., Q-bursts: A comparison of experimental and computed ELF waveforms, *Radio Sci.*, 43, RS4014, doi:10.1029/2008RS003838, 2008.

Nickolaenko, A.P., Kudintseva, I. G., Pechony, O., Hayakawa, M., Hobara, Y., and Tanaka, Y. T., The effect of a gamma ray flare on Schumann resonances, *Ann. Geophys.*, 30, 1321–1329, 2012 doi:10.5194/angeo-30-1321-2012, 2012.

Nickolaenko, A.P., Rabinowicz, L.M., and Shvets, A.V., Polar non-uniformity of ionosphere related to solar proton events, *Telecommun. Radio Eng.*, 67(5), 413–435, 2008.

Ogawa, T. and Komatsu, M., Analysis of Q burst waveforms, *Radio Sci.*, 42, RS2S18, doi:10.1039/2006RS003493, 2007.

Ogawa, T., Tanaka, Y. and Yasuhara, M. , Schumann resonances and worldwide thunderstorm activity, in Planetary Electrodynamics, Ed. by S. C. Coroniti and J. Hughes, Vol. 2, *Gordon and Breach*, New York, Chap. V-7, 1969.

Ogawa, T., Tanaka, Y., Miura, T., and Yasuhara, M., Observations of natural ELF and VLF electromagnetic noises by using ball antennas, *J. Geomagn. Geoelectr.*, 18, 443 – 454, 1966.

Ohya, H., Shiokawa, K., and Miyoshi, Y., Development of an automatic procedure to estimate the reflection height of tweek atmospherics, Earth, *Planets and Space*, 60, 837–843, 2008.

Outsu, J., Numerical study of tweeks based on wave-guide mode theory, *Proc. Res. Inst. Atmos. Nagoya Univ.*, 7, 58-71, 1960.

Pechony, O., Modeling and simulations of Schumann resonance parameters observed at the Mitzpe Ramon field station (Study of the day-night asymmetry influence on Schumann resonance amplitude records), *Ph.D. Thesis, Tel-Aviv University*, Israel, 92 , 2007.

Pechony, O. and Price, C. , Schumann resonance parameters calculated with a partially uniform knee model on Earth, Venus, Mars, and Titan, *Radio Sci.*, 39, RS5007, doi:10.1029/2004RS003056, 2004.

Pechony, O., and Price, C., Schumann resonances: Interpretation of local diurnal intensity modulations, *Radio Sci.*, 41, RS2S05, doi:10.1029/2006RS003455, 2006.

Pechony, O., Price, C. and Nickolaenko, A.P., Relative importance of the day-night asymmetry in Schumann resonance amplitude records, *Radio Sci.*, 42, RS2S06, doi:10.1029/2006RS003456, 2007.

Polk, C., Relation of ELF noise and Schumann resonances to thunderstorm activity, Planetary Electrodynamics, Ed. by S. C. Coronati and J. Hughes, Vol. 2, *Gordon and Breach, New York, Chap. V-6*, 55–83, 1969.

Porrat, D. and Fraser-Smith, A.C., Propagation at Extremely Low Frequencies, in Encyclopedia of Electrical and Electronics Engineering Online, Ed. J. Webster, John Wiley and Sons, New York, 2001.

Potter, R.K., Analysis of audio-frequency atmospheric, *Proc. IRE*, 39(9), 1067–1069, 1951.

Rabinowicz, L.M., Global electromagnetic resonances in non-uniform and anisotropic Earth–ionosphere cavity, *Ph.D. Thesis, Kharkov* (in Russian), 1988.

Rafalsky, V.A. , Resonance phenomena in cross section of the Earth–ionosphere duct and their influence on radio wave excitation and propagation, *Ph.D. Thesis, Kharkov* (in Russian), 1991.

Rafalsky, V.A., Nickolaenko, A.P., and Shvets, A.V., Location of lightning discharges from a single station, *J. Geophys. Res.*, 100, No. D10, 20, 829-20, 838, 1995a.

Rafalsky, V.A., Shvets, A.V. and Hayakawa, M., One-site distance-finding technique for locating lightning discharges, *J. Atmos. Terr. Phys.*, 57, No. 11, 1255-1261, 1995b.

Rakov, V.A. and Uman, M.A., Lightning: Physics and Effects, *Cambridge Univ. Press*, Cambridge, 687, 2013.

Reeve, C.D. and Rycroft, M.J., The eclipsed lower ionosphere as investigated by natural very low frequency radio signals, *J. Atmos. Terr. Phys.*, 34, 667–672, 1972.

Rodger, C. J., Brundell, J. B., and Dowden, R. L., Location accuracy of VLF World Wide Lightning Location (WWLL) network: Post-algorithm upgrade, *Ann. Geophys.*, 23, 277-290, 2005.

Roldugin, V.C., Maltsev, Y.P., Petrova, G.A., and Vasiljev A.N., Decrease of the first Schumann resonance frequency during solar proton events. *J. Geophys. Res.*, 106, 18,555–18, 562, 2001.

Roldugin, V.C., Maltsev, Y.P., Vasiljev, A.N., Shvets, A.V., and Nickolaenko, A.P., Changes of Schumann resonance parameters during the solar proton event of 14 July 2000, *J. Geophys. Res.*, 108(A3), 1103, doi:10.1029/2002JA009495, 2003.

- Roldugin, V.C., Maltsev, Yu.P., Vasiljev, A.N., and Vashenyuk, E.V., Changes of the first Schumann resonance frequency during relativistic solar proton precipitation in the 6 November 1997 event. *Ann Geophysicae*, 17, 1293–1297, 1999.
- Ryabov, B.S., Tweek formation peculiarities. *Geomagn. Aeron.*, English Translation. 34, no. 1, 60 – 66, 1994.
- Rycroft, M.J., Harrison, R.G., Nicoll, K.A., and Mareev, E.A., An overview of Earth's global electric circuit and atmospheric conductivity, in *Planetary Atmospheric Electricity*, Ed. by F. Leblanc et al., *Springer*, New York, 83-105, doi:10.1007/978-0-387-87664-1_6.2000a, 2008.
- Rycroft, M.J., Israelsson, S., and Price, C., The global atmospheric electric circuit, solar activity and climate change, *J. Atmos. Solar-Terr. Phys.*, 62, 1,563-1,576, 2000b.
- Sátori, G., On the dynamics of the north-south seasonal migration of global lightning, Proc. 12th ICAE, *Global Lightning and Climate, Versailles, France*,. 1 – 4, 2003.
- Sátori, G., Mushtak., V., and Williams, E., Schumann resonance signatures of global lightning activity. In: Betz H.D., Schumann U., Laroche P. (Eds) *Lightning: Principles, Instruments and Applications*, *Springer*, Dordrecht, ISBN: 978-1-4020-9078-3, 347–386, 2009.
- Sátori, G., Neska, M., Williams, E., and Szendrői, J., Signatures of the day-night asymmetry of the Earth-ionosphere cavity in high time resolution Schumann resonance records, *Radio Sci.*, 42, RS2S10, doi:10.1029/2006RS003483, 2006.
- Sátori, G., Szendrői, J., and Verö, J., Monitoring Schumann resonances – I. Methodology, *J. Atmos. Terr. Phys.*, 58, 1475–1482, 1996.
- Sátori, G., Williams, E. R., and Boccippio D. J. , Global lightning and climate, *AGU Fall Meeting*, San Francisco, December 8–12. 2003. P. AE32A-0166, 2003.
- Sátori, G., Williams, E., Price, C., Boldi, R., Koloskov, A., Yampolski, Yu., Guha, A., and Barta, V. , Effects of energetic solar emissions on the Earth -ionosphere cavity of Schumann resonances, *Surv. Geophys.*, DOI:10.1007/s10712-016-9369-z, 2016.
- Sátori, G., Williams, E.R., and Mushtak, V. , Response of the Earth ionosphere cavity resonator to the 11-year solar cycle in X-radiation, *J. Atmos. Solar-Terr. Phys.*, 67, 553-562. doi:10.1016/j.jastp.2004.12.006, 2005.
- Schekotov, A. Yu., Nickolaenko, A.P., Hayakawa, M., Hobara, Y., Satori, G., Bor, J., and Neska, M. , Worldwide detection of ELF transient associated with the gamma flare of December 27, 2004, *Telecommun. Radio Eng.*, 72 (18), 1,695-1,718, doi:10.1615/TelecomRadEng.v72.i18.60, 2013.
- Schumann, W.O. , On the free oscillations of a conducting sphere which is surrounded by an air layer and an ionosphere shell, *Z. Naturforschung*, 7a, 149-154 (in German), 1952.

Sekiguchi, M., Hayakawa, M., Nickolaenko, A. P., and Hobara, Y., Evidence of a link between the intensity of Schumann resonance and global surface temperature, *Ann. Geophysicae*, 24, 809 – 817, 2006.

Sentman, D.D., Electrical conductivity of Jupiter shallow interior and the formation of a resonant planetary-ionospheric cavity, *ICARUS*, 88, 73–86, 1990.

Sentman, D.D., Schumann Resonances, in Handbook of Atmospheric Electrodynamics, Ed. by H. Volland, Vol.1, *CRC Press, Boca Raton, FL*, 267–298, 1995.

Sentman, D.D. and Fraser, B.J., Simultaneous observation of Schumann resonances in California and Australia: evidence for intensity modulation by local height of D region, *J. Geophys. Res.*, 96(A9), 15,973-15,984, 1991.

Sheddy, C. H., A general analytic solution for reflection from a sharply bounded anisotropic ionosphere, *Radio Sci.*, 3, No. 8, 792-795, 1968.

Shvets, A., and Hayakawa, M., Global lightning activity on the basis of inversions of natural ELF electromagnetic data observed at multiple stations around the world, *Surv. Geophys.*, 32(6), 705–732, doi:10.1007/s10712-011-9135-1, 2011.

Shvets, A.V., Experimental study of propagation of ELF–VLF radio waves and dynamics of the global thunderstorm activity, *Ph.D. Thesis, Kharkov* (in Russian), 1994.

Shvets, A.V. and Hayakawa, M. , Polarization effects for tweek propagation, *J. Atmos. Solar-Terr. Phys.*, 60, 461–469, 1998.

Shvets, A.V., Hobara, Y., and Hayakawa, M. , Variations of the global lightning distribution revealed from three station Schumann resonance measurements, *J. Geophys. Res.*, 115, A12316. doi:10.1029/2010JA015851, 2010.

Shvets, A.V., Nickolaenko, A. P., and Chebrov, V., Effect of solar flares on Schumann resonance frequencies, report B-4, *Abstracts of MMSMW-2016, Kharkov, Ukraine*, 2016b.

Shvets, A.V., Nickolaenko, A. P., Chebrov, V. N., Influence of solar flares on the Schumann resonance frequencies, *Radiofizika, Izv. VUZo.*(in print), 2016a.

Shvets, A.V., Serdiuk, T.M., Gorishnyaya, Y.V., Hobara, Y., and Hayakawa, M., Estimating the lower ionosphere height and lightning location using multimode "tweek" atmospherics, *J. Atmos. Solar-Terr. Phys.*, 108, 1 – 9, 2014.

Singh, A. K. and Singh, R. P., Propagational features of higher harmonic tweeks at low latitudes, Earth, *Moon and Planets*, 73, 277–290, 1996.

Sukhorukov, A.I., ELF-VLF atmospheric waveforms under night-time ionospheric conditions, *Ann. Geophys.*, 14, 33-41, 1996.

Sukhorukov, A.I., Shimakura, S. and Hayakawa, M., On the additional dispersion of a whistler in the earth-ionosphere waveguide, *Planet. Space Sci.*, 40(9), 1185-1191, 1992.

- Sukhorukov, A.I., Shimakura, S. and Hayakawa, M., Approximate solution for the VLF eigen-values near cut-off frequencies in the nocturnal inhomogeneous Earth-ionosphere waveguide, *Planet. Space Sci.*, 40, 1,363–1,369, 1992.
- Surkov, V. and Hayakawa, M., Ultra and Extremely Low Frequency Electromagnetic Fields, *Springer*, Tokyo, 486, 2014.
- Tanaka, Y. T., Hayakawa, M., Hobara, Y., Nickolaenko, A. P., Yamashita, K., Sato, M., Takahashi, Y., Terasawa, T., and Takahashi, T., Detection of transient ELF emission caused by the extremely intense cosmic gamma-ray flare of 27 December 2004, *Geophys. Res. Lett.*, 38, L08805, doi:10.1029/2011GL047008, 2011.
- Toledo-Redondo, S., Salinas, A., Morente-Molinera, J.A., Mendez, A., Fornieles, J., Portí, J., and Morente, J.A., Parallel 3D-TLM algorithm for simulation of the Earth-ionosphere cavity, *J. Computational Phys.*, 236, 367–379, 2013.
- Velikhov, E. P., Zhamaletdinov, A. A., Sobvhakov, L. A., Veshev, A. V., Sarayev, A. K., Tokarev, A. D., Shevtsov, A. N., Vasilyev, A. V., Sinnikov, A. G. and Yakovlev, A. V., Extra-low frequency sounding of the Earth's crust with a high-power antenna, *Trans. Russian Acad. Sciences (Doklady)*, 341, 12-16, 1996.
- Volland, H., Longwave spheric propagation within the atmospheric waveguide, in *Handbook of Atmospheric*, Ed. by H. Volland, Vol. 2, *CRC Press, Boca Raton, FL*, Chap. 3, 65–93, 1995.
- Wait, J. R., *Electromagnetic Waves in Stratified Media*, *Pergamon Press*, New York, 608, 1970.
- Williams, E.R., The Schumann resonance: a global tropical thermometer, *Science*, 256, 1,184–1,188, 1992.
- Yang, H. and Pasko, V.P., Three-dimensional finite-difference time domain modeling of the Earth-ionosphere cavity resonances, *Geophys. Res. Lett.*, 32, L03114. doi:10.1029/2004GL021343, 2005.
- Yano, M., Ida, Y., Hayakawa, M. and Nickolaenko, A. P., Reception of ELF transmitter signals at Moshiri, Japan and their propagation characteristics, *Radio Sci.*, 45, RS1009, doi:10.2009RS004224, 2010.
- Yano, S., Ogawa, T., and Hagino, H., Wave-form analysis of tweek atmospherics, *Res. Lett. Atmos. Electr.*, 9, 31–42, 1989.
- Yatsevich E.I., Shvets, A. V., and Nickolaenko, A. P., Impact of ELF receiver on characteristics of ELF transients, *Radiophysics and Quantum Electronics*, 57, No.3, 176 – 186, 2014.
- Yedemsky, D.Ye., Ryabov, B.S., Shchokotov, A.Yu., and Yarotsky, V.S. , Experimental investigation of the tweek field structure, *Adv. Space Res.*, 12, 251–254, 1992.
- Zhou, H.J., Hayakawa, M., Galuk, Yu.P., and Nickolaenko, A.P. , Conductivity profiles corresponding to the knee model and relevant SR spectra, *Sun and Geosphere*, 11, No.1, 5–15, 2016.